

# Vector Sum Control of Pulsed Accelerating Fields in Lorentz Force Detuned Superconducting Cavities

Dissertation  
zur Erlangung des Doktorgrades  
des Fachbereichs Physik  
der Universität Hamburg

vorgelegt von  
Thomas Schilcher  
aus Steinhöring

Hamburg  
1998

Gutachter der Dissertation :

Prof. Dr. P. Schmüser  
Dr. A. Gamp

Gutachter der Disputation :

Prof. Dr. P. Schmüser  
Dr. J. Roßbach

Datum der Disputation :

27.04.1998

Dekan des Fachbereichs Physik und  
Vorsitzender des Promotionsausschusses :

Prof. Dr. F.W. Büßer

*For my parents*



## Abstract

The TESLA Test Facility (TTF) is designed to demonstrate the feasibility of a 500 GeV  $e^+e^-$ -linear collider. One of the major subsystems under study is the low level RF control system. For cost saving reasons one klystron supplies RF power to 32 superconducting cavities which are operated in pulsed mode at gradients of up to 25 MV/m. Significant Lorentz force detuning, microphonic noise, and power limitations are the main issues for the low level RF control. A fully digital control system has been developed and installed in the TESLA Test Facility to control the field vector sum of eight cavities initially. The digital feedback system provides flexibility in the control algorithm, precise calibration of the vector sum, extensive diagnostics, and exception handling. The main features are a sampling rate of 1 MHz for the individual cavity signals, digital detection of real and imaginary parts of the complex field vectors instead of amplitude and phase detection, and the concept of adaptive feed forward to suppress repetitive errors to minimize the control effort. During the commissioning phase of the first accelerating module in the TTF linac the RF control system has proven to be a reliable system exceeding the performance goals. The adaptive feed forward scheme has reduced the residual rms errors of amplitude and phase by a factor of 10. Measurements of the microphonic level in the module have shown that the fluctuations of the resonance frequencies are below 10 Hz (rms) under the condition that the helium pressure is kept constant within 0.25 mbar peak to peak. The pulsed operation has not lead to excessive excitation of mechanical resonances of the cavities. Investigations of the dynamics of Lorentz force detuning have shown that the description of the detuning by a first-order differential equation gives a qualitatively good agreement with the measured data. However, it remains the question if the description is still valid for the dynamics at high gradients above 20 MV/m.

## Zusammenfassung

Mit der TESLA Test Facility (TTF) befindet sich ein Test-Linearbeschleuniger im Aufbau, mit dem die technische Realisierbarkeit eines 500 GeV  $e^+e^-$ -Linearbeschleunigers demonstriert werden soll. Eine der wesentlichen Komponenten, die dabei untersucht wird, ist das Hochfrequenzkontrollsystem. Aus Kostengründen wird ein Klystron 32 supraleitende Beschleunigungsstrukturen mit Hochfrequenzleistung versorgen. Die Strukturen werden im Pulsbetrieb bei Beschleunigungsgradienten von bis zu 25 MV/m betrieben. Die Hauptaufgaben für das Hochfrequenzkontrollsystem sind, durch die bei diesen Gradienten bedeutsame Lorentzkraftverstimmung, mechanische Vibrationen (Mikrophonie) und Leistungsbeschränkung des Klystrons gegebenen Störungen und Limitationen zu kompensieren. Für die TESLA Test Facility ist ein volldigitales Hochfrequenzkontrollsystem entwickelt und installiert worden, welches in einer ersten Stufe die Vektorsumme von acht Hohlraumresonatoren regelt. Das digitale Rückkopplungssystem bietet große Flexibilität in der Anwendung von Kontrollalgorithmen, genaue Kalibration der Vektorsumme, umfangreiche Diagnostik und die Möglichkeit, automatisierte Prozeduren für den Ausnahmefall zu implementieren. Die wichtigsten Eigenschaften des Kontrollsystems sind eine Abtastrate von 1 MHz der einzelnen Kavitätensignale, deren digitale Detektion als Real- und Imaginärteile stattfindet anstatt der Detektion von Amplitude und Phase. Desweiteren wird das Konzept von adaptivem Feed Forward angewandt, welches zeitlich periodische Störgrößen unterdrückt und damit die Rückkopplungsschleife entlastet. Während der Inbetriebnahme des ersten Beschleunigungsmoduls der TESLA Test Facility hat das digitale Hochfrequenzkontrollsystem seine Zuverlässigkeit unter Beweis gestellt und die gesteckten Ziele übertroffen. Das Konzept des adaptiven Feed Forwards hat die verbleibenden rms-Fehler in Amplitude und Phase um einen Faktor 10 reduziert. Messungen der mechanischen Vibrationen im Beschleunigungsmodul haben gezeigt, daß die hiervon herrührenden Schwankungen der Resonanzfrequenzen der Kavitäten unter einem Wert von 10 Hz (rms) liegen. Dies galt unter der Voraussetzung, daß die Heliumdruckfluktuationen innerhalb von 0,25 mbar konstant gehalten werden können. Der Pulsbetrieb hat zu keinen übermäßig großen Anregungen von mechanischen Resonanzen der Kavitäten geführt. Untersuchungen zum dynamischen Verhalten der Lorentzkraftverstimmung haben gezeigt, daß die Beschreibung des zeitlichen Verlaufs der Verstimmung durch eine Differentialgleichung erster Ordnung eine qualitativ gute Übereinstimmung mit den gemessenen Daten aufweist. Es bleibt jedoch die Frage, ob diese Beschreibung die Dynamik der Lorentzkraftverstimmung auch noch bei Beschleunigungsgradienten von über 20 MV/m ihre Gültigkeit behält.

# Contents

<b>1</b>	<b>Introduction</b>	<b>1</b>
<b>2</b>	<b>RF Control Design</b>	<b>4</b>
2.1	General Sources for Cavity Field Errors . . . . .	4
2.1.1	Microphonics . . . . .	4
2.1.2	Lorentz Force Detuning . . . . .	6
2.1.3	Calibration Error of the Vector Sum . . . . .	6
2.1.4	Bunch-to-Bunch Charge Fluctuations . . . . .	9
2.1.5	Non-linearity of Field Detector . . . . .	10
2.1.6	Klystron Saturation . . . . .	10
2.1.7	Phase Noise from the Master Oscillator . . . . .	11
2.1.8	Influence of Bunch Length . . . . .	11
2.1.9	Higher Order Modes . . . . .	11
2.2	Requirements on the RF System . . . . .	12
2.2.1	Amplitude and Phase Stability . . . . .	12
2.2.2	Operational Requirements . . . . .	14
2.3	Design Choices for the Control System . . . . .	17
2.3.1	Options to Drive an RF Cavity . . . . .	17
2.3.2	RF Vector Control . . . . .	18
<b>3</b>	<b>Theory of RF Cavities</b>	<b>21</b>
3.1	Cavity with Beam Coupled to RF Generator . . . . .	21
3.2	General Cavity Equations and Definitions . . . . .	25
3.3	Dissipated and Reflected Power of a Cavity . . . . .	30
3.3.1	Cavity without Beam Loading . . . . .	30
3.3.2	Cavity with Beam Loading . . . . .	33
3.3.3	Transient Behavior of a Pulsed RF Cavity with Beam Loading . . .	40
3.4	Mechanical Model for Lorentz Force Detuning . . . . .	46
<b>4</b>	<b>The Digital RF Control System for the TESLA Test Facility</b>	<b>50</b>
4.1	Principle and Components of the Digital Control System . . . . .	50
4.2	Local Oscillator and Timing . . . . .	54
4.3	Digital Signal Processing . . . . .	55

4.3.1	Hardware . . . . .	55
4.3.2	Digital Signal Processor Code . . . . .	62
4.4	Diagnostic Tools . . . . .	64
4.4.1	Detuning Measurement . . . . .	64
4.4.2	Vector Sum Calibration . . . . .	65
4.5	Operational Experience . . . . .	68
4.5.1	Open Loop Operation . . . . .	69
4.5.2	Closed Loop Operation without Beam Acceleration . . . . .	70
4.5.3	Closed Loop Operation with Beam Acceleration . . . . .	70
<b>5</b>	<b>Stability Investigations of Feedback System</b>	<b>75</b>
5.1	Transfer Matrix Representation of Discrete System . . . . .	76
5.2	Transfer Matrices of the Subsystems . . . . .	79
5.3	Open Loop Transfer Matrix of the Digital RF Feedback System . . . . .	84
5.4	Stability Analysis with Bode and Nyquist Plots . . . . .	85
<b>6</b>	<b>Mechanical Properties of the TESLA 9-cell Cavity</b>	<b>93</b>
6.1	Microphonics in the Module . . . . .	94
6.2	Lorentz Force Detuning . . . . .	98
6.3	Mechanical Resonances of the Cavity . . . . .	103
<b>7</b>	<b>Conclusion and Outlook</b>	<b>108</b>
<b>A</b>	<b>Appendix</b>	<b>110</b>
A.1	Effective Accelerating Voltage of an RF Cavity . . . . .	110
A.2	Amplitude and Phase of an LCR circuit . . . . .	112
A.3	Lossless Transmission Line . . . . .	113
A.4	RF Component of a Bunched Beam Current . . . . .	115
A.5	Cavity Power Equation . . . . .	116
A.6	Cavity Differential Equation . . . . .	119
A.7	Open Loop Transfer Function of the Digital RF Feedback System . . . . .	121
A.8	Solution of the First-Order Differential Equation . . . . .	122

# Chapter 1

## Introduction

Particle accelerators have been playing a very important role in experimental particle physics. With these instruments, it has been possible to develop and verify a coherent model describing the fundamental constituents of matter and its interactions. This model is known as the Standard Model. Its predictions concerning the electro-weak forces, which were later confirmed by experiments, have demonstrated the power of this model. Despite its great success, the Standard Model leaves many important questions unanswered. For example, in order to find an explanation for the origin of the mass of the different quarks, leptons and bosons, the Higgs-mechanism has been introduced - but neither the Higgs mass nor the masses of the fundamental particles can be predicted. Particle physicists are therefore called upon to develop and study theories that go beyond the Standard Model. One very attractive extension of the model is the theory of supersymmetry (SUSY), which describes a symmetry between fermions and bosons. It predicts the existence of supersymmetric particles and provides for a unification of the electro-weak and strong interactions in the context of the Grand Unified Theory. However, these points, as yet unclarified, can only be investigated at energy levels that are higher than those available today. At the present time, a new proton-proton circular collider (LHC for Large Hadron Collider) is under construction at CERN (Geneve, Switzerland). It is designed to reach a center of mass energy of 12 - 14 TeV. Despite the fact that positron-electron colliders have a much lower center of mass energy than hadron colliders (like proton-anti-proton colliders), the  $e^+e^-$ -colliders can deliver results of much higher precision. There is widespread agreement within the high energy physics community that an  $e^+e^-$ -collider with an energy level well above the LEP2 center of mass energy ( $E_{cm,s} = 200$  GeV) will provide complementary results [CDR 500]. On account of the initial state of positrons and electrons being well defined, the signature of their collision can reveal precise information about their interaction. The desired energy range of positron-electron annihilation between 300 GeV and 1000 GeV cannot be reached with circular accelerators by reasonable means. The synchrotron radiation losses, which are drastically increasing with increasing energy, can only be avoided in a linear collider. Since the expected cross sections of the interactions in this energy range are in the range below picobarn ( $< 10^{-40}$  m<sup>2</sup>), the required luminosity has to be above  $10^{33}$ cm<sup>-2</sup>s<sup>-1</sup> in order to achieve a reasonable event rate. This demands large

bunch charges, high beam power and extremely small spot sizes at the interaction point.

The TESLA collider (TeV-Energy Superconducting Linear Accelerator) with a center of mass energy of 500 GeV is an approach to reach this goal. It is based on superconducting cavities operating at 1.3 GHz. The full list of design parameters is given in [CDR 500]. To demonstrate the feasibility of such a collider, the TESLA Test Facility (TTF) is presently under construction at DESY (Hamburg, Germany) [TTF CDR]. The first stage of this facility started operating in May 1997. The requirements of unprecedentedly small spot sizes at the interaction point and high luminosity demand a very low energy spread contribution from the RF system. The use of superconducting cavities for a high energy linear collider therefore raises the new challenge of achieving a low energy spread. These cavities have very narrow bandwidths and are consequently highly sensitive to mechanical disturbances. The resulting errors in amplitude and phase have to be corrected by means of feedback systems. The basic principle of an RF control system as used in superconducting electron accelerators is explained in [Grä 92]. In the past few years, several accelerators using superconducting cavities have come into operation (KEK, CERN/LEP, CERN/SPS, DESY/HERA, CEBAF, S-DALINAC, LISA, MACSE, HEPL). Most of them are operated in continuous-wave mode. A list detailing the RF system-related parameters of superconducting electron accelerators (linear and circular) is provided in [Sim 93]. Experience with superconducting cavities at the above-mentioned laboratories has shown that microphonics can cause severe problems in controlling the accelerating fields.

In order to reduce the installation costs of a high energy linac, it seemed advantageous to drive several cavities by one high power klystron instead of supplying RF power to the cavities by individual low power klystrons. This approach has already been used at some accelerator facilities but only in circular machines. One klystron, for example, supplies RF power to four cavities at KEK, 16 cavities at CERN/LEP and 16 cavities at DESY/HERA. In this, the amplitude and phase control of the vector sum of the accelerating field has been used at KEK and at DESY/HERA, while only the scalar sum of the 16 cavities is used for gradient control at CERN/LEP. The objective of the TESLA Test Facility is to control the field vector sum of 32 cavities, which are driven by one 10 MW klystron.

Operating the cavities at an average accelerating gradient of 25 MV/m introduces a new source of interference, which causes the mechanical deformation of the cavities on account of the accelerating field (Lorentz force detuning). Since TESLA will be operated in pulsed mode with RF pulses of 1.3 ms, the mechanical deformation is dynamic and occurs repeatedly. These major interferences, and the effects of microphonics and Lorentz force detuning require a powerful and versatile RF feedback system.

The subject-matter of this thesis is the development of a fully digital RF feedback system to be used in the first stage of the TESLA Test Facility, namely in the control of eight cavities by one common klystron.

In chapter 2, the possible error sources related to RF control are discussed and requirements for amplitude and phase stability are derived. Three different options for an RF feedback system are introduced and the one chosen for the TESLA Test Facility is

presented.

The theory underlying the RF cavities is summarized in chapter 3. In this chapter, steady-state equations are derived and then extended to the transient behavior of a cavity with beam loading. Special attention has been given to the forward and reflected waves at the cavities with mismatches.

The digital RF system, which at present has been installed for the accelerating field control of eight cavities, is described in chapter 4. Furthermore, this chapter provides information on the operational experience gained during commissioning.

In chapter 5, the tools of modern control theory are applied to investigate the stability of the digital RF control system with respect to the loop delay time and the next passband mode ( $\frac{8}{9}\pi$  - mode).

The mechanical properties of a TESLA 9-cell cavity are studied in chapter 6 - including microphonics, the transient behavior of Lorentz force detuning during an RF pulse and the mechanical resonances of the accelerating structure.

# Chapter 2

## RF Control Design

To meet the requirements for a next-generation linear collider, small spot sizes at the collision point and high beam power are necessary to achieve a high luminosity of several  $10^{33} \text{ cm}^{-2}\text{s}^{-1}$ . The TESLA approach of a linear collider design is based on superconducting accelerating structures with average accelerating gradients of 25 MV/m. The advantages of this technology are significant [CDR 500]; however, they are accompanied by some new challenges when compared with the conventional approach that uses normal conducting accelerating cavities. The requirements for the RF system demand a sufficiently low energy spread of the beam at the interaction point.

In this chapter, the general sources of errors of the accelerating field resulting in energy spread are investigated in the case of a superconducting linear accelerator before the requirements for an RF control system are specified. In the final section, different design options and the one chosen for the TESLA Test Facility are presented.

### 2.1 General Sources for Cavity Field Errors

Energy fluctuations of an accelerated beam along a linac are caused by various phenomena. The cavities in TTF/TESLA are operated in a pulsed mode where each klystron drives up to 32 cavities. The maximum pulse repetition rate is 10 Hz. The RF pulse length is 1330  $\mu\text{s}$  from which 530  $\mu\text{s}$  are required to build up the RF field in the cavities. The beam is accelerated for 800  $\mu\text{s}$  with a constant accelerating field. Three different types of energy fluctuations have to be distinguished: macro pulse-to-macro pulse, bunch-to-bunch and intra-bunch energy fluctuations. Some of them have been studied in detail in [Mos 95]. The following provides an overview of the different contributions to the energy spread.

#### 2.1.1 Microphonics

Mechanical vibrations caused by the accelerator environment are always present and may be transferred to the accelerating structures. A schematic diagram of the possible sources and the transfer medium is shown in Figure 2.1 [Grä 92]. Vibrations caused by vacuum pumps can be transferred to the cavities by the beam tube. Man-made noise (traffic,

machinery, etc.) and ground motions (seismic activities, ocean waves, elastic motion produced by the moon) are imposed on the linear accelerator through the ground and the supports. In addition to these, the vibrations of the pumps and compressors of the cryogenic plants can be passed onto the cavities by means of the helium transfer lines or directly by the liquid helium flow. Each transfer medium has a certain filter characteristics on the imposed noise resulting in a filtered microphonics frequency spectrum transferred to the cavities or to their supports. The vibrations modulate the resonance frequency of the cavity. In superconducting linacs, the cavities have a high quality factor which results in a narrow resonance bandwidth in the order of a few hundred Hertz. As far as TESLA with its loaded quality factor of  $Q_L = 3 \cdot 10^6$  is concerned, the bandwidth is 217 Hz at a resonance frequency of 1.3 GHz. Since mechanical vibrations are expected in the range well below 1000 Hz [Mos 94], the resulting change in the resonance frequency is very small during a 1300  $\mu$ s pulse. It mainly influences the resonance frequency from macro-pulse to macro-pulse and therefore the RF phase with respect to the beam if no feedback loops are closed. It has been shown [Ju et.al.93][Shi et.al.95][Br/Ro 94] that ground motions with frequencies above 0.1 Hz are wave-like with wave lengths of up to several hundred meters. The power density of these motions is decreasing very rapidly with increasing frequency. The resulting vibrational excitation of the cavities can be considered as correlated. Nevertheless, man-made noise usually predominates over natural noise. Therefore, the microphonic noise is not predictable and is expected to be uncorrelated along the linac.

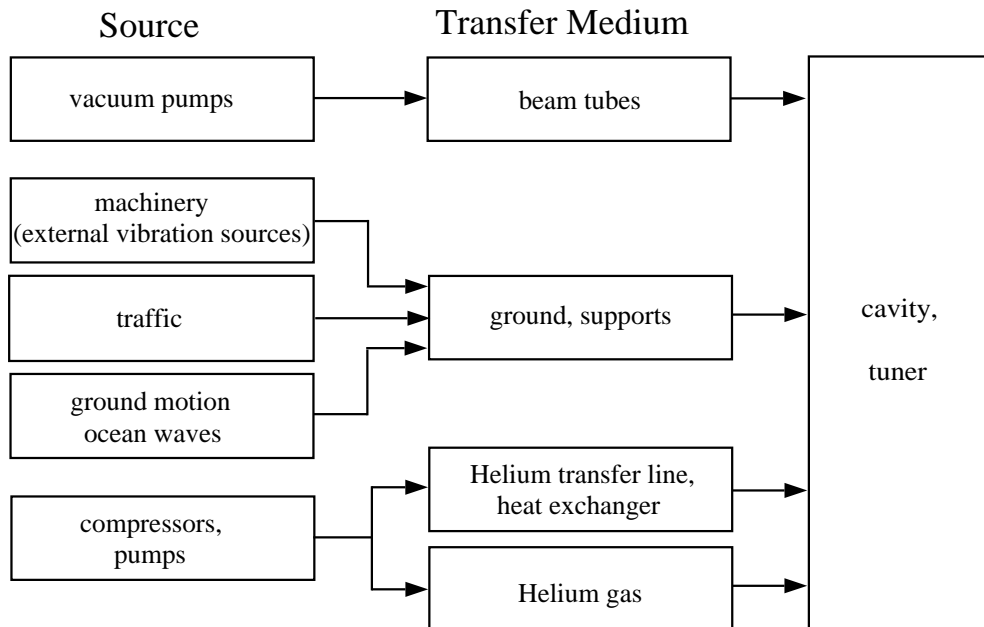


Figure 2.1: Microphonic sources and their transfer medium to an accelerating cavity.

### 2.1.2 Lorentz Force Detuning

The objective is to reach high electromagnetic fields in superconducting structures. However, high electromagnetic fields in a cavity cause strong Lorentz forces acting on the walls. This deforms the cavity, leading to a change in the resonance frequency. It is however possible to increase the wall thickness to enhance its rigidity. On the other hand, the wall thickness should be kept thin since this ensures more effective cooling by liquid helium and results in lower material costs. As a consequence of this, a compromise between the two aspects has to be found. The wall thickness of the TESLA cavities has been chosen to be 2.8 mm, and the individual cells are stiffened with stiffening rings to reduce Lorentz force detuning. This detuning is gradient-dependent and under steady-state condition proportional to the square of the electrical field. However, the TESLA cavities are operated in pulsed mode. Building up a field in a cavity results in a dynamic behavior of the resonance frequency from the initial to the final state. This is due to the inertial mass of the cavity walls. The transient behavior is discussed in detail in chapter 3.4. On account of repetitive excitation of the cavities, Lorentz force detuning is predictable from pulse-to-pulse. The variation of amplitude and phase of the RF field can be considered correlated from cavity to cavity. The calculated energy spread induced only by Lorentz force detuning without RF feedback is  $\sigma_E/E \approx 2.8 \cdot 10^{-3}$  for accelerating gradients of  $E_{acc} = 25$  MV/m at the end of the linac (TESLA 500) [Mos 95].

### 2.1.3 Calibration Error of the Vector Sum

RF sources like klystrons are expensive devices. The experience with existing klystrons has shown that many smaller units are more expensive than fewer high-power klystrons. A reduction of capital investment is to be expected if a large number of cavities are driven by one single klystron. In TTF / TESLA, it is planned to supply 32 cavities by a single 10 MW high-power klystron. For this reason, the RF control system has to control the vector sum of the accelerating fields of a control section of 32 cavities. Calibration errors in amplitude and phase of these individual fields result in an additional energy spread in the presence of microphonic noise. The measured vector sum and the actual vector sum seen by the beam differ on account of these errors. Even if a control system stabilizes the measured vector sum perfectly, the microphonic noise results in a different actual vector sum from macro-pulse to macro-pulse. This leads to different energy gains per control section. A control section is a string of cavities whose vector sum is controlled by one feedback system acting on the klystron which feeds the cavities. In Figure 2.2, the schematic of the measured and actual vector sum of eight cavities is displayed.

Simulations with different levels of microphonic noise have been carried out. The resonance frequencies of an ensemble of cavities have been assumed to be Gaussian distributed from pulse to pulse in the given microphonic range. This results in different amplitudes and phases according to the resonance curves of the cavities. Table 2.1 shows the required amplitude- and phase-calibration accuracy for two different acceptable relative energy gain errors for different strings of modules. The energy gain  $E_g$  is the energy

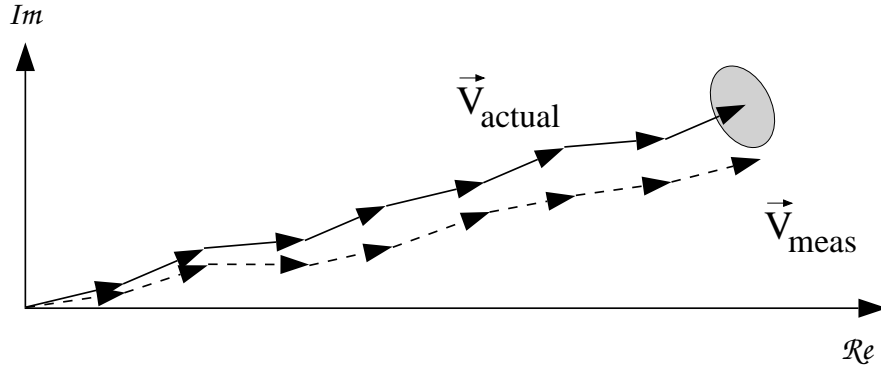


Figure 2.2: The measured vector sum of eight cavities with amplitude and phase calibration errors differs from the actual vector sum of the accelerating fields as seen by the beam. In the presence of microphonics, the actual vector sum fluctuates from macro-pulse to macro-pulse even with perfect amplitude and phase control.

which a particle gains by the given amount of cavities while  $(\Delta E_g)_{rms}$  is the according energy gain error caused by calibration errors of the vector sum. It has become evident that gradient calibration errors contribute much less to the energy gain error than phase errors. This is shown in Figure 2.3 where 16 cavities are fed by one klystron. In the left diagram, the resulting energy gain error is plotted versus the amplitude calibration error. Thereby it is assumed that the phases of the individual cavities are calibrated within  $\pm 1^\circ$ . The right diagram shows the reversed case where the energy gain error is plotted versus phase calibration error. The amplitude calibration error is in the range of  $\pm 10\%$ . The loaded  $Q_L$  is set to  $3 \cdot 10^6$  and the microphonic noise level to  $\pm 10$  Hz (rms). Each point (cross) in the plot represents the following: a set of amplitude and phase calibration errors within the given range has been chosen and kept constant. Then, microphonics causes an energy fluctuation due to these calibration errors. The resulting rms energy gain error is plotted as a cross.

To meet the energy spread requirements, an appropriate calibration method for the vector sum has to be applied. It is evident that the more cavities are fed by one klystron, the more relaxed the requirements for the calibration of amplitude and phase are. It should also be mentioned that the total energy spread caused by vector sum calibration errors decreases with the square root of the number of cryomodules in a control section. The energy gain errors are presumably uncorrelated (microphonics is the most relevant reason). For example: an energy gain error of  $4 \cdot 10^{-4}$  per controlled vector sum of a control section results in an energy spread contribution of  $2.3 \cdot 10^{-5}$  (TESLA 500 with  $N=308$  klystrons).

		gradient calibration error				
		1 %	5 %	10 %	15 %	
$\frac{(\Delta E_g)_{rms}}{E_g} < 2 \cdot 10^{-4}$	microphonics	tolerable phase calibration error (peak values)				
	$\sigma_f$					
	40 Hz	–	–	–	–	
	20 Hz	0.2°	–	–	–	
8 cavities	10 Hz	0.9°	0.8°	0.7°	0.5°	
	5 Hz	1.7°	1.7°	1.6°	1.6°	
	40 Hz	–	–	–	–	
	20 Hz	0.4°	–	–	–	
16 cavities	10 Hz	1.2°	1.1°	1.0°	0.8°	
	5 Hz	2.4°	2.4°	2.4°	2.4°	
	40 Hz	0.05°	–	–	–	
	20 Hz	0.5°	–	–	–	
24 cavities	10 Hz	1.4°	1.4°	1.3°	1.1°	
	5 Hz	2.8°	2.8°	2.8°	2.8°	
	40 Hz	0.1°	–	–	–	
	20 Hz	0.6°	–	–	–	
32 cavities	10 Hz	1.6°	1.6°	1.5°	1.4°	
	5 Hz	3.3°	3.3°	3.3°	3.2°	
	$\frac{(\Delta E_g)_{rms}}{E_g} < 4 \cdot 10^{-4}$		tolerable phase calibration error (peak values)			
	40 Hz	0.2°	–	–	–	
8 cavities	20 Hz	0.6°	0.2°	–	–	
	10 Hz	1.7°	1.7°	1.7°	1.5°	
	5 Hz	3.6°	3.5°	3.4°	3.4°	
	40 Hz	0.4°	–	–	–	
16 cavities	20 Hz	1.0°	0.6°	–	–	
	10 Hz	2.3°	2.3°	2.3°	2.2°	
	5 Hz	4.7°	4.7°	4.6°	4.6°	
	40 Hz	0.5°	–	–	–	
24 cavities	20 Hz	1.2°	0.9°	–	–	
	10 Hz	2.8°	2.8°	2.8°	2.6°	
	5 Hz	5.7°	5.7°	5.6°	5.6°	
	40 Hz	0.6°	–	–	–	
32 cavities	20 Hz	1.3°	1.2°	–	–	
	10 Hz	3.3°	3.3°	3.2°	3.2°	
	5 Hz	6.5°	6.4°	6.4°	6.4°	

Table 2.1: Vector sum calibration requirements for amplitude (gradient) and phase of a 9-cell cavity to meet the required rms energy gain error. Microphonics is assumed to be Gaussian distributed with width  $\sigma_f$ . Amplitude and phase calibration errors of the vector sum are uniformly distributed in the given range (peak value). A bar indicates that the required energy gain error cannot be reached with the according gradient calibration error.

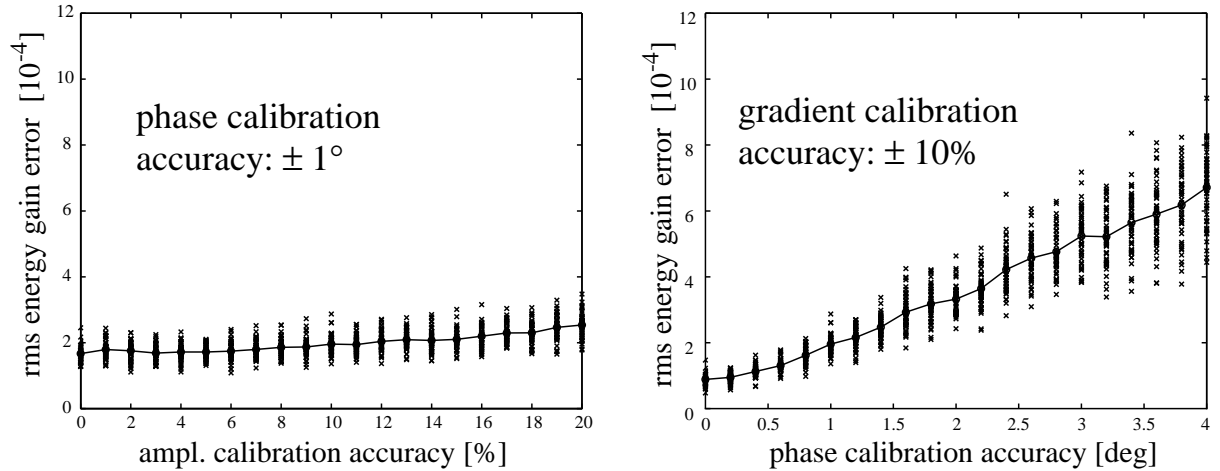


Figure 2.3: Left: Energy gain error versus gradient calibration accuracy for the vector sum control of 16 cavities. The phases are calibrated within  $\pm 1^\circ$  and the microphonic noise level is  $\pm 10$  Hz (rms). Right: Energy gain error versus phase calibration accuracy for the vector sum control of 16 cavities. The gradients are calibrated within  $\pm 10\%$  and the microphonic noise level is  $\pm 10$  Hz (rms).

### 2.1.4 Bunch-to-Bunch Charge Fluctuations

Superconducting cavities with high loaded quality factors  $Q_L$  possess large characteristic time constants  $\tau$ . As a consequence, the filling times of the cavities from zero to the nominal accelerating field are several hundred microseconds. A bunch passing through the cavity with a high bunch charge extracts energy, which results in a small, immediate drop of the accelerating gradient called a transient of the amplitude. This energy has to be supplied by an RF power source before accelerating the next bunch. The cavity voltage rises again with the time constant  $\tau$ . The result is that the beam imposes a profile on the gradient. The bunched structure of the TTF beam current produces a sawtooth-like profile where a klystron fills up the cavity again between the bunch spacing of one microsecond (injector II). The drop of the gradient is  $1.4 \cdot 10^{-3}$  at 25 MV/m with a bunch charge of 8 nC. As a consequence, the transient amplitude of a varying beam current changes from bunch-to-bunch on account of the extracted energy being different. Therefore, the bunch-to-bunch energy spread increases. In contrast to fast bunch-to-bunch charge fluctuations, slow charge variations resulting in a slow cavity field variation can be compensated for by a feedback system. Fast bunch-to-bunch charge fluctuations will increase the energy spread linearly since the transient amplitude is directly proportional to the bunch charge. Hence, the gradient in the cavity varies. The expected bunch-to-bunch energy spread contribution with feedback loops for  $\pm 10\%$  charge fluctuations is  $(\sigma_E/E) \approx 1.51 \cdot 10^{-4}$

for TTF and  $(\sigma_E/E) \approx 1.11 \cdot 10^{-4}$  for TESLA 500 [Mos 95].

### 2.1.5 Non-linearity of Field Detector

The common control loop of an ensemble of cavities with slightly different loaded  $Q_L$  and mechanical properties (Lorentz force constant  $K$ , mechanical time constant  $\tau_m$ ) results in a time varying gradient distribution. Microphonics modulates the initial resonance frequencies of the cavities. The consequence is different gradient distributions from macro pulse to macro pulse. RF field detectors like Schottky diodes or RF mixers are therefore operated at different working points on their characteristic input-output curve. Non-linearities of these devices result in a time varying measured vector sum error. Applying feedback control can control only the measured vector sum. Hence, the bunch-to-bunch energy spread varies within a macro pulse. The linearity requirements of the field detectors strongly depend on the feedback system. The more sophisticated the controller, the less stringent the linearity requirements are.

### 2.1.6 Klystron Saturation

Klystrons show input-output non-linearities known as saturation. A typical saturation curve is plotted in Figure 2.4 which is the type of klystron used for the first accelerating modules in the TESLA Test Facility. The electronic efficiency of this klystron is 41%.

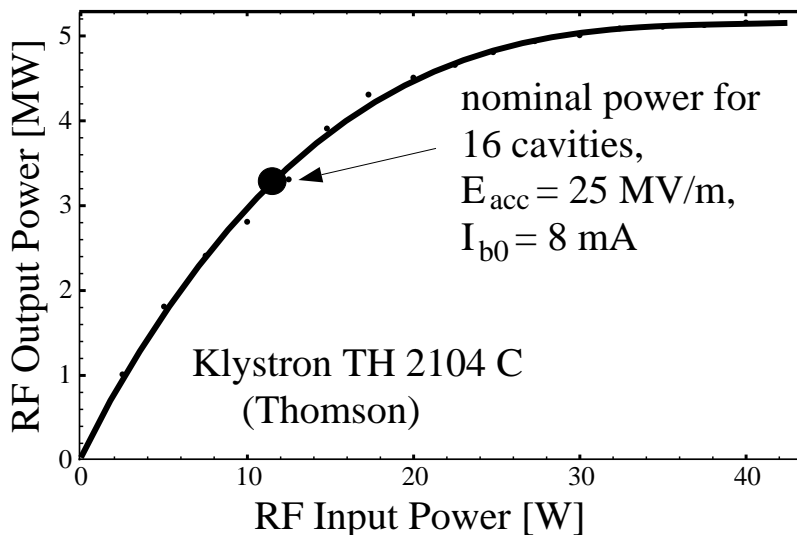


Figure 2.4: Klystron saturation curve of the 5 MW klystron TH 2104 C made by Thomson (TTF klystron). The power of the output RF signal is plotted versus the input RF signal. The cathode voltage is 126 kV and the current 95 A.

With a cathode voltage of 126 kV and a beam current of 95 A, the saturated RF output power is 5 MW. The required RF power for 16 cavities at gradients of 25 MV/m and 8 mA beam current is 3.32 MW (see Figure 2.4). To reduce the operating cost, it is desirable to reduce the cathode voltage as much as possible. For TTF, a 30% peak power reserve is needed for amplitude and phase control. Additionally, allowance is made for a 10% power margin to saturation [Ga]. The nominal operating point will be about 40% below the maximum output. The operation will be in the non-linear regime of the klystron causing a power-dependent gain. It is known from control theory that the residual error with a proportional feedback controller is inversely proportional to the gain factor. If the required power varies during a beam pulse (for example due to Lorentz force detuning), this will result in a varying gradient because of the proportional gain. RF control close to the saturation of a klystron is fairly complex and demands sophisticated controllers. Usually, neither analog feedback systems nor even digital ones with proportional gain take into account the non-linearity of the klystron input-output curve. As a consequence, this will result in an energy spread within the macro-pulse.

### 2.1.7 Phase Noise from the Master Oscillator

Two types of RF control systems are commonly used in accelerators: firstly, driven systems in which a signal from a reference oscillator (master oscillator) is manipulated to act as a source signal in order to drive a cavity; and secondly, systems using self-excited loops whose phase is locked to an external reference oscillator during beam acceleration. In both systems, the phase noise from the reference oscillator results in a measured phase noise of the cavity field probe signal. A control system tries to compensate for this, thereby imposing a real phase jitter on the beam which yields a bunch-to-bunch energy spread.

### 2.1.8 Influence of Bunch Length

Due to the finite bunch length, the RF accelerating voltage seen by a particle depends on its position in the bunch. This creates an intra-bunch energy spread. The effect increases when the bunch is accelerated off-crest, i.e. accelerating phase is different from  $0^\circ$ . The  $0^\circ$  are defined as the phase with respect to the maximum accelerating voltage. A more precise definition is given in chapter 3.3. The sign of the accelerating phase is shown in Figure 2.5. In storage rings, it is necessary to accelerate the beam off-crest to achieve stability with respect to synchrotron oscillations. The beam has a phase  $\phi_b$  with respect to the maximum accelerating voltage. Even in linear accelerators it might be desirable to accelerate off-crest by a few degrees to compensate for the induced wakefields which result in an intra-bunch energy spread (see next subsection).

### 2.1.9 Higher Order Modes

Standing wave RF accelerating structures are usually operated in the fundamental resonance mode  $TM_{010}$  (accelerating mode). The wakefields of short bunches passing the

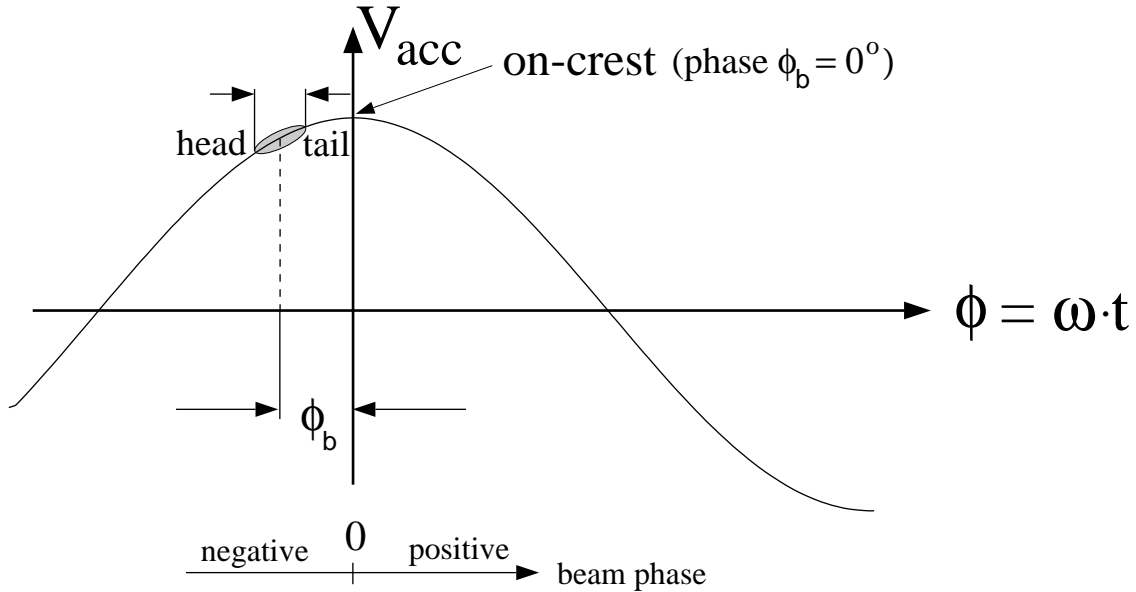


Figure 2.5: Effect of RF curvature on bunches of finite length. The beam phase is defined with respect to the on-crest operation (phase  $0^\circ$ ).

cavity can excite high order modes. These modes perturb the field distribution of the accelerating mode. Higher order modes ( $TM$ ,  $TE$ ) can cause an intra-bunch and intra-macro-pulse energy spread. The estimated bunch-to-bunch energy spread in TESLA due to wakefields and due to the effect of the finite bunch length is in the order of  $5 \cdot 10^{-4}$  [CDR 500].

## 2.2 Requirements on the RF System

The RF control system for the TESLA Test Facility is a prototype for the TESLA linear collider. For the sake of the desired high luminosity in the interaction point and for the sake of the restricted acceptance of the accelerator optics (particle losses have to be minimized), the energy fluctuations have to be kept small. The goal for TESLA 500 is an energy spread of  $2 \cdot 10^{-3}$  [CDR 500]. Besides that, the extra power needed to compensate for the effects of microphonics and Lorentz force detuning has to be minimized. Additionally, reliability, operability, robustness and maintainability in the design have to be taken into account.

### 2.2.1 Amplitude and Phase Stability

The energy spread at the interaction point is the result of different sources as discussed in the previous section. Gradient and phase fluctuations will result in bunch-to-bunch energy spread. It is desirable to keep it below the intra-bunch energy spread of  $5 \cdot 10^{-4}$ . The influence of small correlated amplitude and phase errors is given by the formula [Mos 94]

$$\left(\frac{\sigma_E}{E}\right) = \frac{1}{\cos \phi_b} \sqrt{\frac{1}{2}(1 + \cos 2\phi_b) \left(\frac{\sigma_A}{A}\right)^2 + \frac{1}{2}(1 - \cos 2\phi_b)\sigma_\varphi^2 + \frac{1}{4}(3 \cos 2\phi_b - 1)\sigma_\varphi^4}.$$

Here, Gaussian distributions for amplitude and phase errors are assumed. The quantity  $\left(\frac{\sigma_A}{A}\right)$  denotes the relative amplitude rms error while  $\sigma_\varphi$  describes the rms phase error.  $A$  is the amplitude (gradient) of the accelerating field in the cavity. With regard to the special case of on-crest acceleration ( $\phi_b = 0$ ), the previous formula simplifies to

$$\left(\frac{\sigma_E}{E}\right) = \sqrt{\left(\frac{\sigma_A}{A}\right)^2 + \frac{\sigma_\varphi^4}{2}}.$$

If the amplitude and phase errors of the cavities are uncorrelated, the proper statistical average is given by this expression divided by the square root of the number of control sections  $N$ .

$$\left(\frac{\sigma_E}{E}\right) = \frac{1}{\sqrt{N}} \sqrt{\left(\frac{\sigma_A}{A}\right)^2 + \frac{\sigma_\varphi^4}{2}} \quad (\text{uncorrelated errors})$$

For TTF with its 8 cryomodules (8 cavities each) one klystron supplies RF power for 32 cavities resulting in  $N = 2$ . For TESLA 500, a total number of  $N = 308$  klystrons for each linac (positron and electron linac) is planned (32 cavities per klystron). The total energy spread from correlated and uncorrelated errors is

$$\left(\frac{\sigma_E}{E}\right)^2 = \left(\frac{\sigma_E}{E}\right)_{corr.}^2 + \left(\frac{\sigma_E}{E}\right)_{uncorr.}^2$$

Assuming that correlated field fluctuations can be suppressed to a value better than  $3 \cdot 10^{-4}$ , the uncorrelated fluctuations are in the same order (also  $3 \cdot 10^{-4}$ ) to meet the relative bunch-to-bunch energy spread of  $5 \cdot 10^{-4}$ . In TESLA 500, the requirements for the uncorrelated errors are therefore  $\sqrt{N} \cdot 3 \cdot 10^{-4} \approx 5 \cdot 10^{-3}$ . In Figure 2.6, the energy spread is plotted versus the uncorrelated phase and amplitude errors. In the upper plot, the phase dependence of the energy spread is calculated for two different uncorrelated amplitude errors. The dash dotted line indicates acceleration on-crest, while the solid line stands for injecting the beam  $-3^\circ$  off-crest with respect to the maximum acceleration voltage. In [Mos 95] it has been shown that this is the optimum beam phase to compensate for wakefield effects. The lower plot shows the amplitude dependence of the energy spread for two different uncorrelated phase errors. The influence of amplitude errors on the energy spread is bigger than that of phase errors. Figure 2.7 displays the

same observation for correlated errors. From these two figures it can be concluded that suppressing uncorrelated amplitude and phase errors to a value better than  $5 \cdot 10^{-3}$  and  $0.5^\circ$ , respectively, and suppressing correlated amplitude and phase errors to a value better than  $3 \cdot 10^{-4}$  and  $0.1^\circ$ , respectively, is needed to meet the requirements to stay below the tolerable upper limit for the energy spread.

### **2.2.2 Operational Requirements**

The turn-on procedure of the RF control for a section of 32 cavities driven by one klystron is quite complex. Therefore, it is desirable to have automated procedures for the calibration of the vector sum, the adjustment of the phases at the individual cavities and for the control of the cavity frequency tuners. Moreover, the amplitude and phase of the accelerating field need to be changed frequently during operation. Further consideration needs to be given to the importance of integrating the RF control system into the framework of the overall linac control system, whilst preserving the possibility of stand-alone operation.

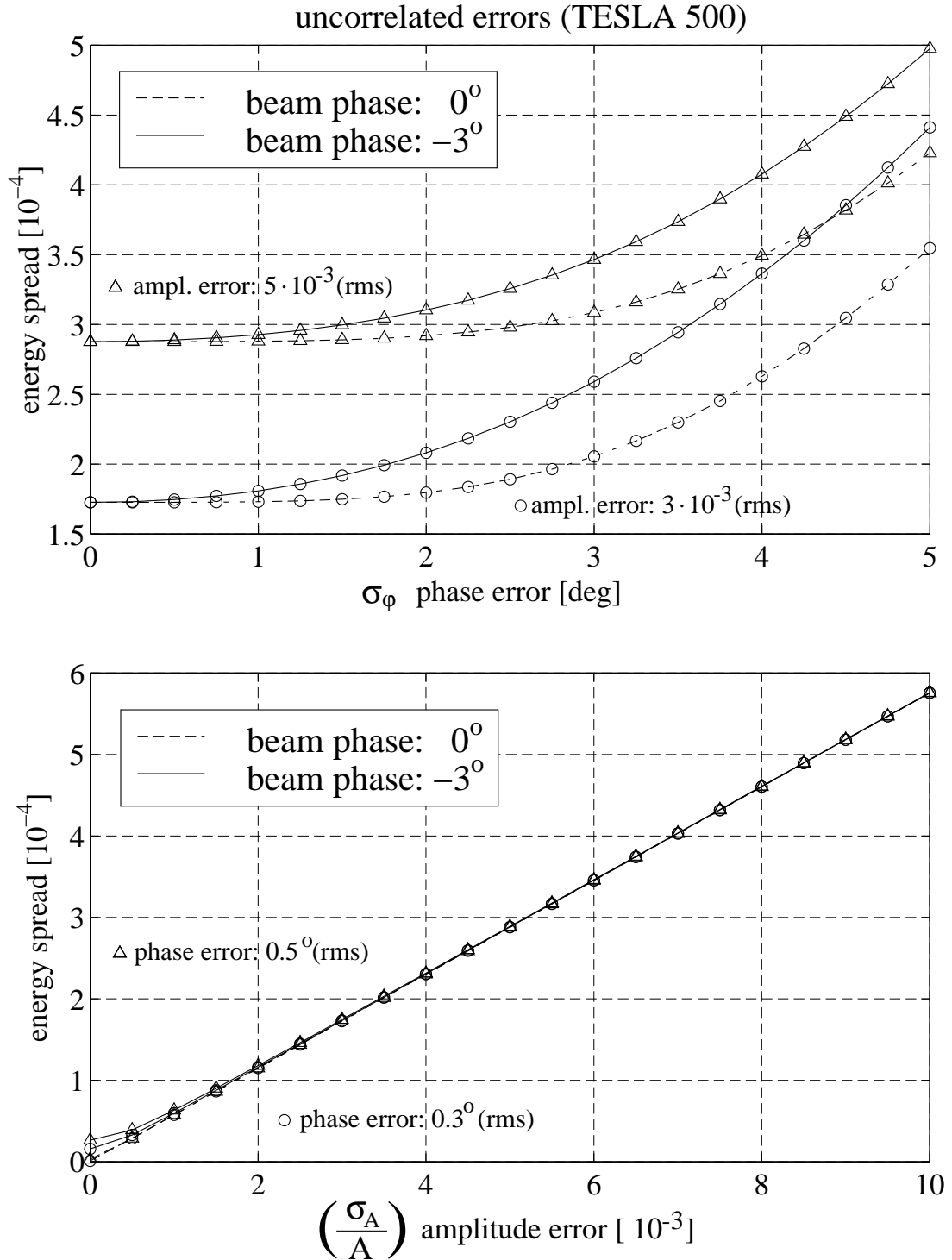


Figure 2.6: Energy spread due to uncorrelated amplitude and phase errors of the vector sum of 32 cavities. The dashed line is valid for beam phase  $0^\circ$ , while the solid line is calculated for optimum beam phase  $-3^\circ$  (TESLA 500).

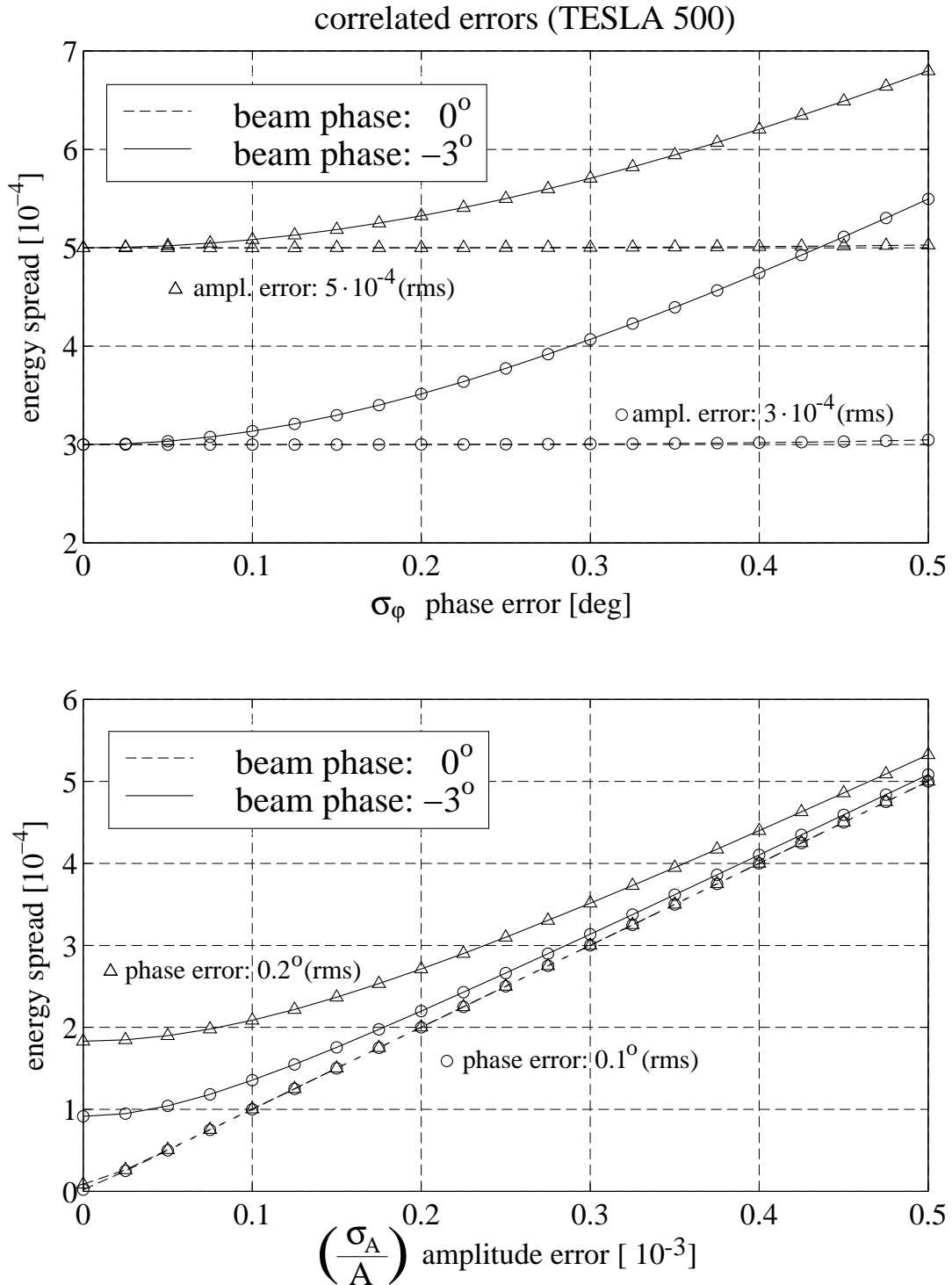


Figure 2.7: Energy spread due to correlated amplitude and phase errors of the vector sum of 32 cavities. The dashed line is valid for beam phase 0°, while the solid line is calculated for optimum beam phase -3° (TESLA 500).

## 2.3 Design Choices for the Control System

Control of the RF power normally takes place on the low-power level before the amplification of the signals. The main components are detectors for amplitude and phase of the individual cavity fields, the controller for the feedback itself, and actuators to control the incident wave to the klystron and thus to the cavities. There are different ways to drive an RF cavity: the driven feedback system, the self-excited loop and the direct RF feedback. In the first two cases, one can choose to control amplitude and phase or the real and imaginary parts of the incident RF vector. In subsection 2.3.2, the appropriate choice depending on the requirements will be discussed.

### 2.3.1 Options to Drive an RF Cavity

#### ”Driven” Feedback

The basic element of a driven feedback is an RF reference source, the so-called master oscillator (MO). The RF output signal of the master oscillator is controlled by actuators which act on amplitude and phase before the RF wave is amplified, for example by a klystron, and guided into the cavity. A pick-up antenna in the cavity detects the accelerating field, and detectors, which can be gradient and phase detectors, provide the input signal to the feedback controllers. These detectors extract amplitude and phase of the fast oscillating RF field. The setup is shown in Figure 2.8.

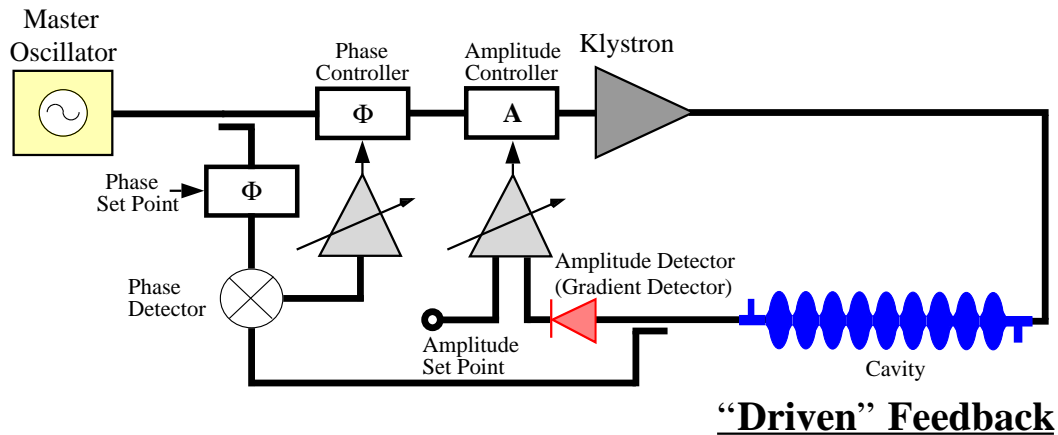


Figure 2.8: Basic principle of a driven feedback system. The reference signal from a master oscillator is controlled by actuators. This signal is amplified by a klystron and guided to an RF cavity.

## Self-Excited Loop

In the self-excited loop, the cavity field-probe signal is directly applied to the actuators (phase and amplitude controllers) which control the incident wave. Figure 2.9 shows the principle of a self-excited loop. The loop phase  $\phi_{Loop}$  has to be set in such a way that the

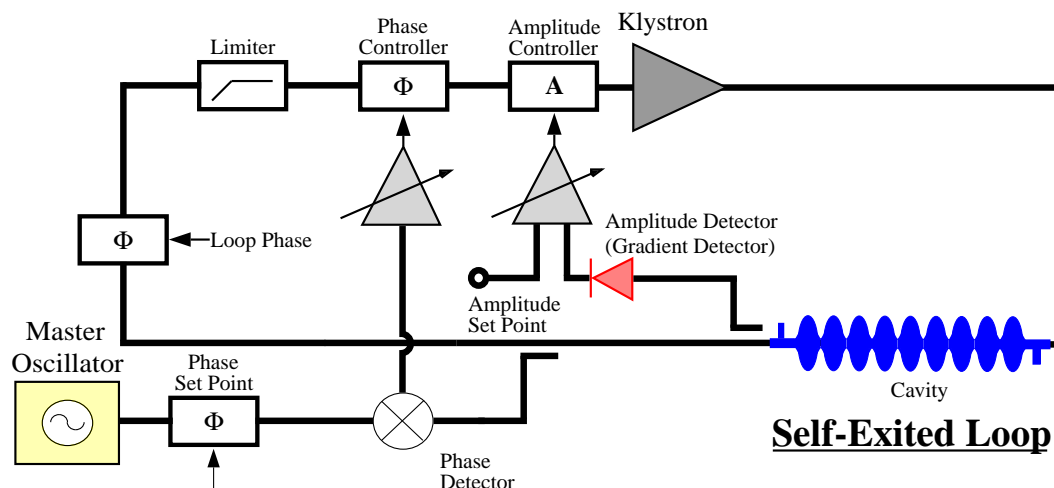


Figure 2.9: Basic principle of a self-excited loop system.

condition for self-excited oscillation is fulfilled, i.e. it has to be a multiple of  $2\pi$ . Then, the oscillations of the RF field in the cavity start by themselves from noise on the incident wave. A limiter in the loop ensures that the amplitude remains bounded. As in a driven feedback system, field detectors extract amplitude and phase information from the RF signal and feed it to the feedback controller. The phase of the cavity is regulated with respect to an external master oscillator.

### ”Direct” RF Feedback

In contrast to the two previous systems, the cavity RF field probe signal is directly compared with a reference signal on the RF level. In the direct RF feedback system (Figure 2.10), no gradient and phase detectors are necessary. Combining the two RF signals results in an error signal which drives the klystron. Amplitude and phase of the reference signal are set by actuators.

## 2.3.2 RF Vector Control

Apart from the direct RF feedback all other introduced RF control systems include elements to detect amplitude and phase of the RF field. In general, an RF field is described

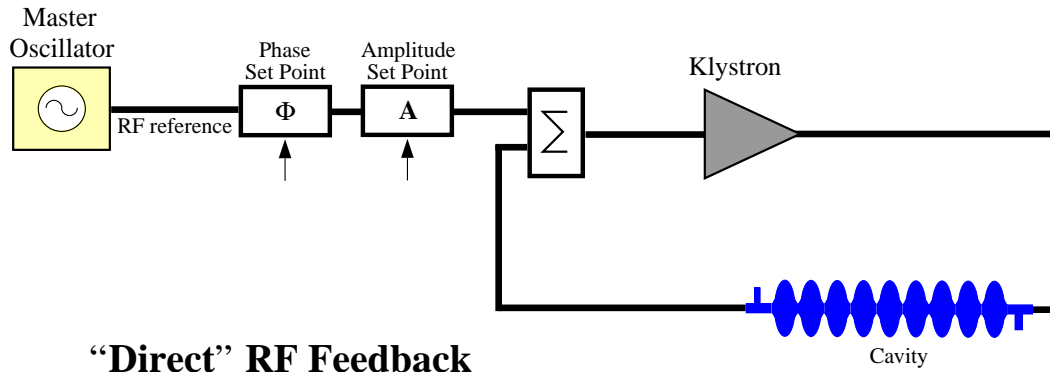


Figure 2.10: Basic principle of a direct RF feedback system.

by a vector in the complex plane. This RF vector can be represented either by its amplitude and phase with respects to a reference oscillator or by its real and imaginary parts. These are sometimes called the I (in-phase,  $0^\circ$ ) and the Q (quadrature,  $90^\circ$ ) components of a vector which is a commonly used but misleading notation. The appropriate choice of representation depends on the requirements. An amplitude detector is usually a Schottky diode and a widely used phase detector is a double balanced RF mixer. The determination of real and imaginary parts is completely based on RF mixers. Phase noise from the master oscillator directly influences the measurement of real and imaginary parts while in the traditional amplitude and phase control only the phase measurement is affected. If the disturbance of the RF field is mainly on the amplitude, gradient and phase control might be preferable. On the other hand, vector control by real and imaginary parts is preferred in systems with large errors in amplitude and phase where sufficiently high feedback gains have to be used. It should be noted that a phase controller can cause a phase correction in a wrong quadrant if the gain is too high (for example, phase error of  $2^\circ$  with a feedback gain of 100 results in a phase correction of  $200^\circ$  which is the third quadrant). Besides that, the phase is not well defined if the input signal of the phase detector is too small. As a result it is not possible to control the zero set point with amplitude and phase controllers.

In the linac of the TESLA Test Facility the cavities are operated with a driven feedback system. Lorentz force detuning and microphonics lead to considerable amplitude and phase disturbances in the superconducting cavities with their high quality factors. The expected errors are in the order of a few percent for amplitude and above  $20^\circ$  for the phase during the  $800 \mu\text{s}$  long beam pulse. Therefore, a vector control has been chosen. RF mixers decompose the cavity RF vector into the real and imaginary parts. The incident RF wave is regulated by a vector modulator. In principle, the feedback controller can be realized as an analog or a completely digital system. In the case of a digital system analog digital convertors (ADC) digitize the decomposed RF signal from the cavity. A following digital

signal processing stage performs the feedback algorithm before the calculated actuator signals are reconverted to analog signals. For the RF control in the TESLA Test Facility a fully digital system has been implemented. It provides a much higher flexibility and operability than an analog system. A detailed description is given in chapter 4.

# Chapter 3

## Theory of RF Cavities

### 3.1 Cavity with Beam Coupled to RF Generator

Resonant modes in cavities can be described by means of resonant LCR circuits. A rigorous justification is given in [Mon 48]. First, we shall concern ourselves with a single-cell cavity which can be a pillbox in the simplest case. When a particle passes through an RF cavity, the accelerating field  $E(z, t)$  on the cavity axis changes due to the time varying RF field. The cavity voltage  $V_{cav}$  is defined as the maximum accelerating voltage acting on a particle. The transit time effect is included. This definition implies that the electric field assumes its maximum when the particle passes the center of the cavity (so-called 'on crest' acceleration). The accelerating voltage for a bunch passing the cavity with a time delay  $t_b$  (see appendix A.1) is

$$V_{acc}(t_b) = V_{cav} \cdot \cos \phi_b = V_{cav} \cdot \cos(\omega t_b) .$$

To feed a cavity with RF power, an input coupler is necessary. Building a linear accelerator with single-cell cavities would be very expensive, and it would require a great deal of effort to equip every cavity with a separate coupler. Therefore, several cells are coupled weakly to a coupled-resonator structure with a single RF feed point. The coupling from cell to cell can be magnetic and/or electric. The resonator in the TESLA Test Facility consists of nine electrically coupled cells and is usually called 'cavity'. In Figure 3.1, an equivalent LCR circuit model with magnetic coupling is shown. A structure with nine coupled cells has nine normal modes, called passband modes. The corresponding nine resonance frequencies of a TESLA cavity are shown in Figure 3.2. The passband modes are labeled by their phase shift from cell to cell. The TESLA Test Facility is operated in the  $\pi$ -mode, which means that the RF fields in adjacent cells have a phase difference of  $\pi$ . The passband mode closest to the accelerating mode is the  $\frac{8}{9}\pi$ -mode which is separated by approximately 800 kHz. Every passband mode can be modelled by an LCR circuit which is parallel to the others. The quantities  $L$ ,  $C$  and  $R$  refer to the whole nine-cell structure. The following considerations are restricted to the  $\pi$ -accelerating mode.

An RF field induces surface currents in the cavity walls resulting in power dissipation  $P_{diss}$ . Modelling a resonant cavity by an LCR circuit, the resistor  $R$  is defined as a resistor

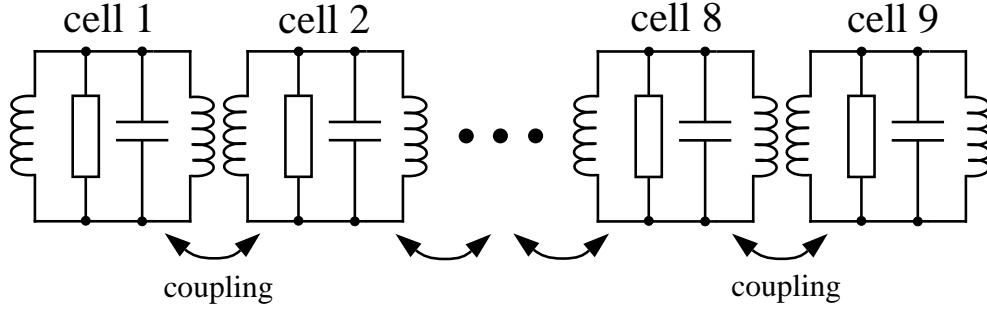


Figure 3.1: Equivalent circuit representation for a chain of nine magnetically coupled, resonant single-cell cavities.

in which the same power is dissipated as in the cavity.

$$P_{diss} = \frac{1}{2} \cdot \frac{V_{cav}^2}{R} = \frac{V_{cav}^2}{R_{sh}}. \quad (3.1)$$

In linear accelerator physics however, a resistor  $R_{sh}$  is defined as the shunt impedance of a cavity. It is also defined by the power dissipation in the cavity but includes the factor  $1/2$  of the time average. The definition (3.1) of the shunt impedance  $R_{sh}$  is widely used

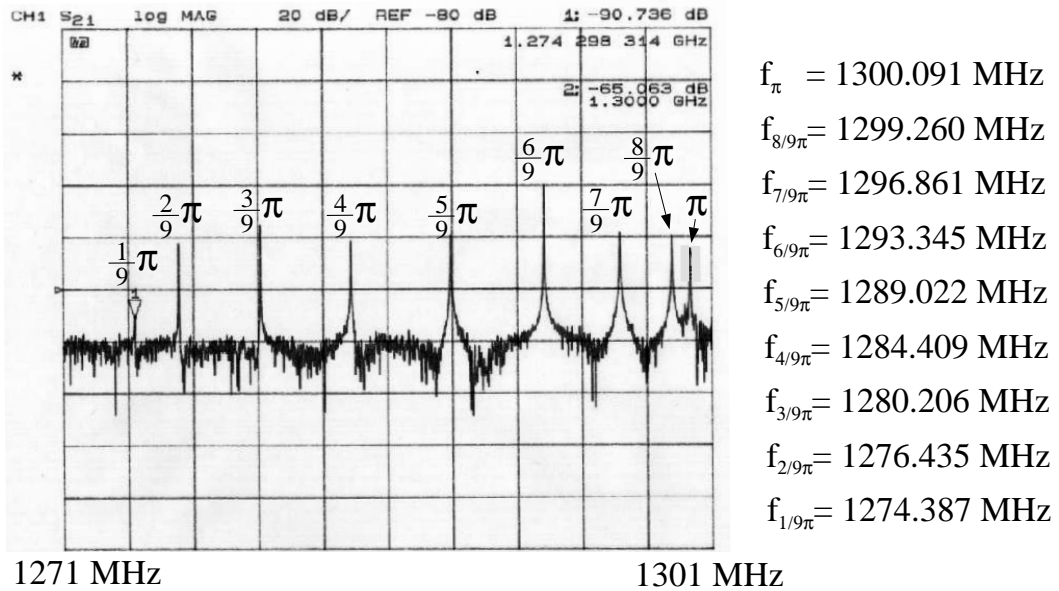


Figure 3.2: Passband modes of a TESLA nine-cell cavity [Kre].

in linear accelerator physics but confusing in describing a cavity by an LCR circuit. The unfortunate definition of a normalized shunt impedance ( $r/Q$ ) (which will be defined later on) is based on  $R_{sh}$ . Throughout this thesis, only the resistor  $R$  is used, whilst the linear accelerator definition of the normalized shunt impedance is kept. This leads to the strictly applied relation

$$R = \frac{1}{2} \cdot R_{sh} = \frac{1}{2} \cdot \left(\frac{r}{Q}\right) \cdot Q_0 \quad (3.2)$$

The excitation of the cavity by the generator and by the beam can be described by current sources in the equivalent circuit model. For relativistic particles ( $v \approx c$ ), the beam current remains unchanged during acceleration in the cavity. If the beam is non-relativistic, the cavity field will raise the velocity of the beam and thereby also the beam current. In such a case, the beam current becomes a function of cavity voltage. In the following only relativistic beams will be considered. Our RF power source is a klystron. It can be modelled as an output cavity driven by a current source  $I_{kly}$  as shown in Figure 3.3. The couplings from the output cavity of the klystron to the transmission line and from

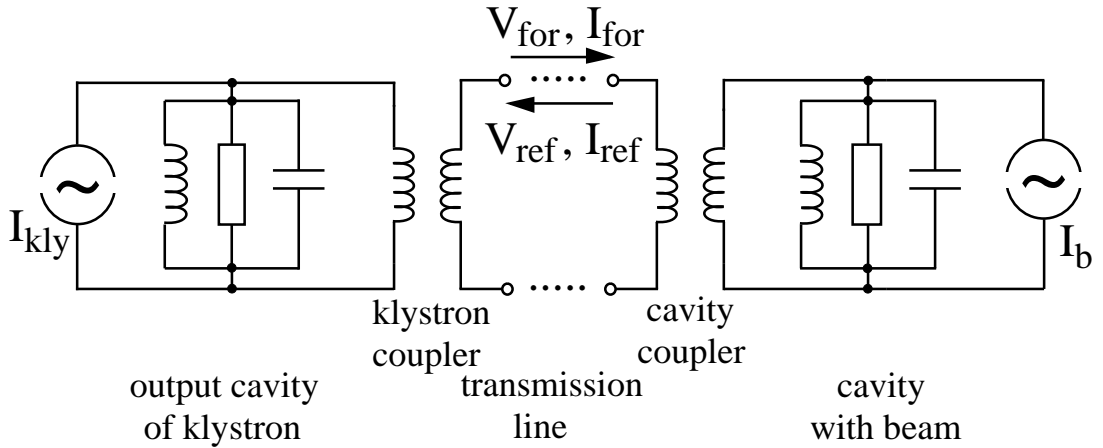


Figure 3.3: Model of a cavity with beam coupled to a klystron by couplers and transmission lines.

the transmission line to the cavity are represented by lossless transformers. The input coupler of the cavity has a transformation ratio of 1:N (see Figure 3.4). The transformation equations are

$$V_2 = N \cdot V_1, \quad I_2 = \frac{1}{N} \cdot I_1 \quad (3.3)$$

and therefore input and output impedance are related by

$$Z_2 = N^2 \cdot Z_1. \quad (3.4)$$

The transmission line can be a waveguide or a coaxial cable. In the transmission line, forward and backward travelling waves occur due to mismatches of the input and output

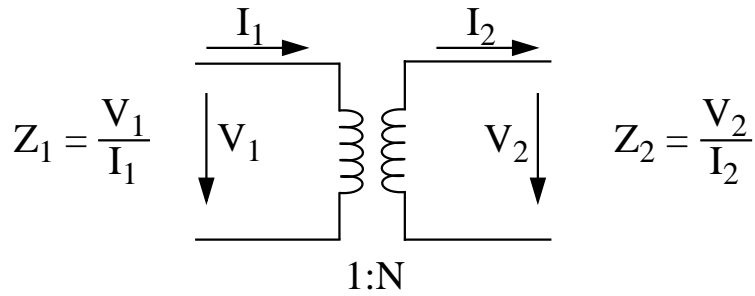


Figure 3.4: Input coupler representation as an ideal transformer.

impedances. For the present purpose, it is sufficient to disregard the complexities of microwave generation in a klystron and to represent the klystron as an RF current source coupled to a transmission line. This provides the simplified circuit diagram of Figure 3.5. A circulator is inserted into the transmission line which directs the RF wave from

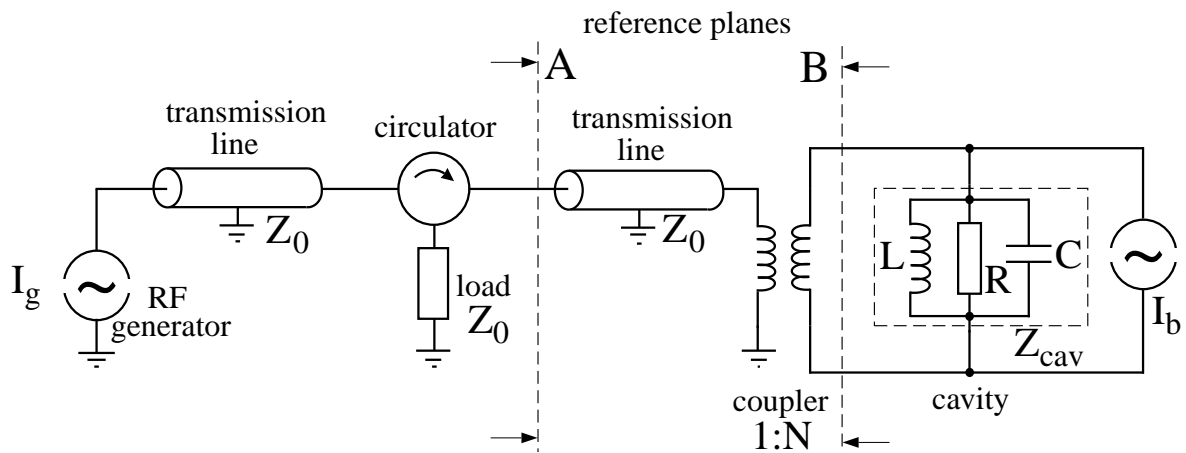


Figure 3.5: Simplified model of cavity coupled to an RF generator by coupler and transmission lines.

the generator to the cavity and deviates any waves which are reflected at the cavity to a matched load with impedance  $Z_0$ . This is necessary since the klystron may be destroyed by reflected waves. In the following, the circuit model is split up into three sections which are separated by the reference planes indicated in Figure 3.5.

When viewed from the generator (left side of reference plane A), the transmission line is always properly terminated (Fig. 3.6a) since the circulator guarantees that no reflected wave is traveling back to the klystron.

Looking towards the cavity at reference plane B, the transmission line is terminated by the transformed cavity impedance  $Z'_{cav}$ .

$$Z'_{cav} = \frac{1}{N^2} \cdot Z_{cav}$$

All voltages, currents and impedances on the generator side of the coupler are labeled with a prime with the exception of the transmission line impedance which is denoted by  $Z_0$ . Unprimed quantities correspond to the 'cavity side' of the coupler. The equivalent model at reference plane B is shown in Figure 3.6b. In this, the beam current  $I_b$  is transformed to  $I'_b$  at the generator side which is fed directly at the cavity impedance  $Z'_{cav}$ . It is only the generator current that is conducted to the cavity through a transmission line.

In circuit 3.6c, all currents and voltages are transformed to the cavity side. Moreover, the transmission line, which is properly terminated by the load  $Z_0$ , acts as a parallel load to the cavity resistor  $R$ . The energy stored in the LC circuit is only partly dissipated in resistor  $R$  (representing the losses in the cavity walls) but the major part is coupled out and dissipated in the external load  $Z_{ext}$ . All other losses in the coupler, the transmission line itself, etc. are included in the load  $Z_{ext}$ . This representation is very useful when describing the behavior of the cavity; however, one has to keep in mind that the model shown in Figure 3.6c uses a fictitious generator current  $\tilde{I}_g$ . The real current supplied by the klystron is only  $I_g$  which will be derived in section 3.3. It will be shown that the fictitious current is related to the true current  $I_g$  (with  $I_g = (1/N) \cdot I'_g$  from Figure 3.6a) by

$$\tilde{I}_g = 2 I_g . \quad (3.5)$$

The fictitious current  $\tilde{I}_g$  is introduced to represent the effect of the circulator as seen from the cavity. The model of Figure 3.6c abandons the description with the transmission line. The current  $\tilde{I}_g$  has to be derived from the RF power delivered by the generator.

In section 3.3, the power calculations are carried out with the transmission line model shown in Figure 3.6b.

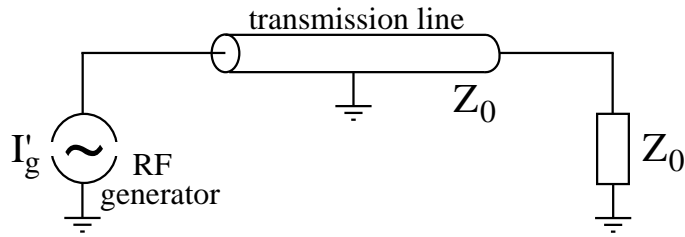
## 3.2 General Cavity Equations and Definitions

Since a cavity is a resonant device, it is useful to define a measure for its quality, the so-called quality factor  $Q$  defined as

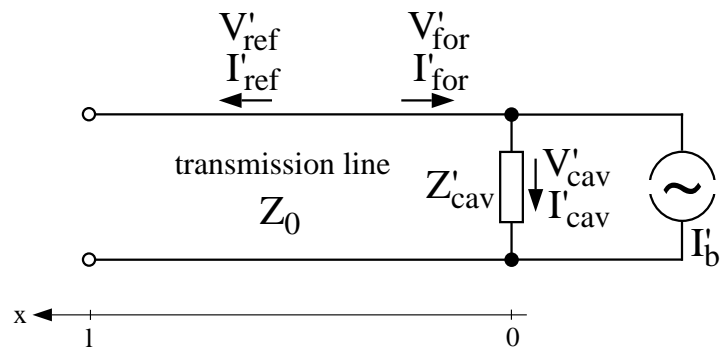
$$Q = 2\pi \frac{\text{stored energy in cavity}}{\text{dissipated energy per cycle}} = \frac{\omega_0 W}{P_{diss}} \quad (3.6)$$

where  $W$  is the stored energy,  $\omega_0$  is the resonance frequency, and  $P_{diss}$  the dissipated power. When only the losses occurring in the cavity walls caused by the RF surface resistance (which are also present for superconducting materials) are taken into account, one arrives at the unloaded quality factor  $Q_0$ . Taking into account basic formulas from circuit theory ( $W = 1/2 C V_0^2$  ;  $P_{diss} = V_0^2 / (2R)$ ),

a) left side of reference plane A:



b) right side of reference plane A:



c) right side of reference plane B:

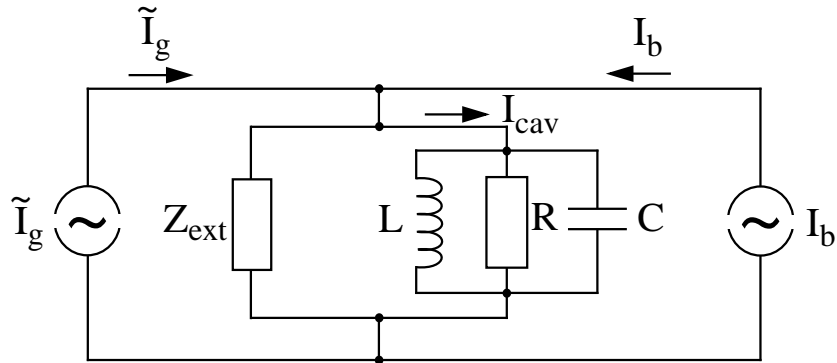


Figure 3.6: Subdivisions of the circuit diagram of Figure 3.5.

a) Generator side. On account of the circulator, the transmission line is always properly terminated with forward travelling waves only.

b) The transmission line from the circulator to the input coupler of the cavity is terminated with the transformed cavity impedance  $Z'_{cav}$  which in general is different from  $Z_0$ .

c) The cavity circuit. The external load  $Z_0$  is transformed to the cavity side of the coupler to  $Z_{ext} = N^2 \cdot Z_0$ .

the quality factor  $Q_0$  can be written as

$$Q_0 = \frac{2\pi}{T} \cdot \frac{\frac{1}{2} CV_0^2}{\frac{1}{2} \frac{V_0^2}{R}}$$

where  $V_0$  is the amplitude of the oscillating voltage and  $T$  the time period of an RF cycle. In terms of the resonance frequency of an undamped LC circuit  $\omega_0 = \frac{1}{\sqrt{LC}}$ , the unloaded quality factor  $Q_0$  can be expressed as

$$Q_0 = \omega_0 RC = \frac{R}{L\omega_0} = \frac{\omega_0 W}{P_{diss}} \quad (3.7)$$

(with  $C = \frac{1}{L\omega_0^2}$ )

Energy is not only dissipated in the cavity walls but also extracted through the power coupler and dissipated in an external load. An external quality factor  $Q_{ext}$  is defined as

$$Q_{ext} = 2\pi \frac{\text{stored energy in cavity}}{\text{dissipated energy in external devices per cycle}} = \frac{\omega_0 W}{P_{ext}} \quad (3.8)$$

where  $P_{ext}$  is the dissipated power in all external devices. Finally, the loaded quality factor  $Q_L$  is defined as

$$Q_L = 2\pi \frac{\text{stored energy in cavity}}{\text{total energy loss per cycle}} = \frac{\omega_0 W}{P_{tot}} \quad (3.9)$$

Energy conservation yields

$$P_{tot} = P_{diss} + P_{ext} \quad (3.10)$$

and with eq. (3.7), (3.8) and (3.9)

$$\frac{1}{Q_L} = \frac{1}{Q_0} + \frac{1}{Q_{ext}} \quad (3.11)$$

For superconducting cavities, the unloaded  $Q_0$  is typically several orders of magnitude larger than the external  $Q_{ext}$  ( $Q_0 \gg Q_{ext}$ ), so  $Q_L \approx Q_{ext}$ .

As displayed in Fig. 3.6c, the transformed external load  $Z_{ext}$  acts as a parallel resistor to the cavity resistor  $R$ . Therefore, these two resistors can be replaced by a single resistor  $R_L$ , the loaded shunt impedance.

$$\frac{1}{R_L} = \frac{1}{R} + \frac{1}{Z_{ext}} \quad (3.12)$$

The load  $Z_{ext}$  is a real quantity (characteristic impedance of a coaxial cable: 50  $\Omega$  (real)). From equation (3.7) we obtain

$$\frac{R}{Q_0} = \omega_0 L = \frac{1}{\omega_0 C} = \sqrt{\frac{L}{C}}.$$

The ratio  $\frac{R}{Q_0}$  only depends on the quantities  $L$ ,  $C$  and  $\omega_0$ . It is characteristic of the geometry of a cavity and independent of the surface resistance. Unfortunately, the definition is made in terms of the shunt impedance  $R_{sh}$  instead of  $R$  leading to the definition (with equation (3.2))

$$\frac{r}{Q} := \frac{R_{sh}}{Q_0} = \frac{2 \cdot R}{Q_0} \quad (3.13)$$

The shunt impedance of the TESLA cavities is 1041  $\Omega$ .

Instead of the transformation ratio 1:N, it is useful to describe the coupling between transmission line and cavity by the so-called coupling factor  $\beta$ . This factor  $\beta$  is defined as the ratio of the resistor  $R$  in the LCR circuit to the transformed external load  $Z_{ext}$

$$\beta = \frac{R}{Z_{ext}} = \frac{R}{N^2 Z_0}, \quad N = \sqrt{\frac{R}{\beta Z_0}}. \quad (3.14)$$

With this definition, equation (3.12) can be written as

$$R_L = \frac{R}{1 + \beta} \quad (3.15)$$

and therefore (with eq. (3.13))

$$Q_L = \frac{Q_0}{1 + \beta}$$

The coupling factor  $\beta$  is frequently used to describe the behavior of normal conducting cavities where  $\beta$  is in the order of one. For superconducting resonators with  $Q_0 \gg Q_L$ , the coupling factor  $\beta$  is in the order of  $10^3$  to  $10^4$ . For TESLA cavities, the objective is to reach unloaded quality factors of more than  $5 \cdot 10^9$  while the loaded  $Q_L$  is  $3 \cdot 10^6$ . In the following, we will see that the properties of a loaded superconducting cavity are mainly determined by the loaded  $Q_L$  except for the cryogenic load (RF loss) which depends only on  $Q_0$ . In this case, the relevant quantities are  $(r/Q)$  and  $Q_L$  instead of  $\beta$ . Therefore, both representations will be given.

The preceding definitions are used to calculate the stored energy in a resonator with accelerating voltage  $V_{cav}$  (with eq. (3.1), (3.7), (3.13)) as

$$W = \frac{V_{cav}^2}{\omega_0 \left(\frac{r}{Q}\right)}.$$

Taking the 9-cell TESLA cavity as an example, we get for the stored energy at  $V_{cav}=25$  MV,  $\left(\frac{r}{Q}\right) = 1040 \Omega$  and  $f = \frac{\omega}{2\pi} = 1.3$  GHz

$$W = 73.5 \text{ J}$$

The starting point for modelling cavities in an RF system is the externally driven LCR circuit. The external load is included in  $R_L$ . Inserting in Kirchhoff's rule

$$I_C + I_R + I_L = I$$

the formulas  $\dot{I}_L = V/L$ ;  $\dot{I}_R = \dot{V}/R_L$ ;  $\dot{I}_C = C\ddot{V}$  and replacing the inductance  $L$  and capacitance  $C$  by the quantities  $Q_L$  and  $\omega_0$  ( $\frac{1}{R_L C} = \frac{\omega_0}{Q_L}$  and  $\frac{1}{LC} = \omega_0^2$ ), we obtain the differential equation for a driven LCR circuit.

$$\begin{aligned}\ddot{V}(t) + \frac{1}{R_L C} \dot{V}(t) + \frac{1}{LC} V(t) &= \frac{1}{C} \dot{I}(t) \\ \ddot{V}(t) + \frac{\omega_0}{Q_L} \dot{V}(t) + \omega_0^2 V(t) &= \frac{\omega_0 R_L}{Q_L} \dot{I}(t)\end{aligned}\quad (3.16)$$

If the applied current  $I$  is harmonic ( $I(t) = \hat{I}_0 \sin(\omega t)$ ), the driving term on the right side of equation (3.16) will be proportional to  $\cos(\omega t)$ , and the stationary solution of the differential equation (3.16) (which is the particular solution) is given by

$$V(t) = \hat{V} \cdot \sin(\omega t + \psi) \quad (3.17)$$

$$\text{with} \quad \tan \psi = R_L \cdot \left( \frac{1}{\omega L} - \omega C \right) \quad (3.18)$$

$$\text{and} \quad \hat{V} = \frac{R_L \hat{I}_0}{\sqrt{1 + \left[ R_L \left( \frac{1}{\omega L} - \omega C \right) \right]^2}} \quad (3.19)$$

The phase angle  $\psi$  between the driving current  $I$  and the voltage  $V$  is defined as the tuning angle of the cavity. Replacing the quantities  $L$  and  $C$  with  $\omega_0$  and  $Q_L$  (similar as in eq. (3.7)), we get

$$\tan \psi = \frac{\omega_0}{\omega} \cdot \underbrace{\frac{R_L}{\omega_0 L}}_{Q_L} - \frac{\omega}{\omega_0} \cdot \underbrace{\omega_0 R_L C}_{Q_L} = Q_L \left( \frac{\omega_0}{\omega} - \frac{\omega}{\omega_0} \right) \quad (3.20)$$

$$\hat{V} = \frac{R_L \hat{I}_0}{\sqrt{1 + Q_L^2 \left( \frac{\omega_0}{\omega} - \frac{\omega}{\omega_0} \right)^2}} = \frac{R_L \hat{I}_0}{\sqrt{1 + \tan^2 \psi}} \quad (3.21)$$

If the generator frequency  $\omega$  is very close to the cavity resonance frequency  $\omega_0$ , we can rewrite eq. (3.20) and (3.21) to

$$\begin{aligned}\tan \psi &\approx 2Q_L \frac{\Delta\omega}{\omega} = 2Q_L \frac{\Delta f}{f} \\ \hat{V}(\Delta\omega) &\approx \frac{R_L \hat{I}_0}{\sqrt{1 + (2Q_L \frac{\Delta\omega}{\omega})^2}}\end{aligned}\quad (3.22)$$

where  $\Delta\omega = \omega_0 - \omega$ . The frequency dependence of the amplitude is known as Lorentz curve and is shown together with the phase in Fig. 3.7. The bandwidth  $\omega_{1/2}$  of a loaded cavity is defined as the frequency bandwidth where the voltage drops to  $1/\sqrt{2}$  (-3 dB)

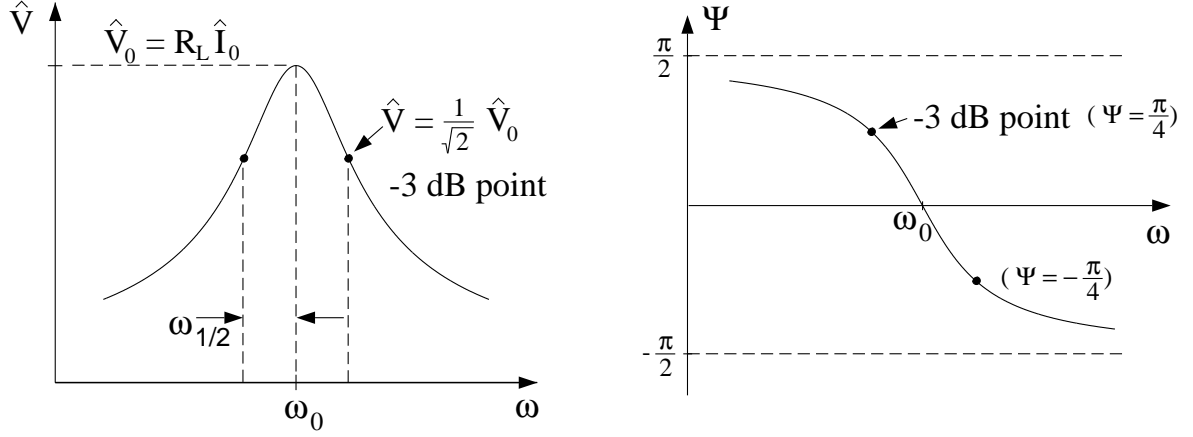


Figure 3.7: Resonance curves for amplitude and phase of a cavity. The -3 dB point is marked in both diagrams.

of its maximum  $\hat{V}_0 = R_L \hat{I}_0$ . The stored energy therefore drops by half. From equation (3.21) and (3.22), we get

$$|\tan(\psi)| = 1 \quad \Longleftrightarrow \quad \psi = \pm \frac{\pi}{4}$$

$$\omega_{1/2} = \frac{\omega}{2Q_L}.$$

Alternatively, amplitude and phase can be deduced directly by means of complex impedances (appendix A.2).

### 3.3 Dissipated and Reflected Power of a Cavity

Part of the RF power supplied to a cavity can be reflected at the input coupler. The amount of reflected power depends on the coupling ratio and on the presence of beam in the cavity. All voltages and currents are represented by complex quantities which will be written in bold-face letters.

#### 3.3.1 Cavity without Beam Loading

Our first approach is concerned with a cavity without beam loading coupled to a lossless transmission line with wave impedance  $Z_0$ . The wave equations of the transmission line are derived in A.3 and read

$$\frac{\partial^2 \mathbf{V}}{\partial x^2} = L' C' \frac{\partial^2 \mathbf{V}}{\partial t^2}, \quad \frac{\partial^2 \mathbf{I}}{\partial x^2} = L' C' \frac{\partial^2 \mathbf{I}}{\partial t^2}. \quad (3.23)$$

According to A.3, the general solution of these two equations can be written as

transmission line:

$$\mathbf{V}(x, t) = \mathbf{V}_{for}(x, t) + \mathbf{V}_{ref}(x, t) \quad (3.24)$$

$$= \hat{\mathbf{V}}_+ e^{i(\omega t - kx)} + \hat{\mathbf{V}}_- e^{i(\omega t + kx)} \quad (3.25)$$

$$\mathbf{I}(x, t) = \mathbf{I}_{for}(x, t) + \mathbf{I}_{ref}(x, t) \quad (3.26)$$

$$= \frac{\hat{\mathbf{V}}_+}{Z_0} e^{i(\omega t - kx)} - \frac{\hat{\mathbf{V}}_-}{Z_0} e^{i(\omega t + kx)} \quad (3.27)$$

with forward wave:

$$\mathbf{V}_{for}(x, t) = \hat{\mathbf{V}}_+ e^{i(\omega t - kx)} \quad (3.28)$$

$$\mathbf{I}_{for}(x, t) = \frac{\hat{\mathbf{V}}_+}{Z_0} e^{i(\omega t - kx)} = \frac{\mathbf{V}_{for}(x, t)}{Z_0} \quad (3.29)$$

and reflected wave:

$$\mathbf{V}_{ref}(x, t) = \hat{\mathbf{V}}_- e^{i(\omega t + kx)} \quad (3.30)$$

$$\mathbf{I}_{ref}(x, t) = -\frac{\hat{\mathbf{V}}_-}{Z_0} e^{i(\omega t + kx)} = -\frac{\mathbf{V}_{ref}(x, t)}{Z_0} \quad (3.31)$$

The minus sign of  $\mathbf{I}_{ref}$  indicates the counterflowing current while the voltages of forward and backward waves add up.

The transmission line is terminated with an impedance  $Z'_{cav}$  at the input of the power coupler. To determine the forward power (incident towards the cavity) and the reflected power (due to a mismatch to the line impedance), the LCR circuit of the cavity has to be transformed to the generator side of the coupler.

In order to calculate forward and reflected waves, the model shown in Figure 3.6b is applied. The defined tuning angle  $\psi$  (eq. (3.20)) is the angle between the forward current  $\mathbf{I}'_{for}$  (which is the driving current of the circuit) and the voltage across the loaded LCR circuit  $\mathbf{V}'_{cav}$ . The cavity impedance  $Z_{cav}$  (cavity side of coupler) at the end of the transmission line is similar to equation (A.4) but with  $R_L$  having been replaced by  $R$ .

The impedance of the unloaded cavity is

$$Z_{cav} = \frac{R}{1 - iR \left( \frac{1}{\omega L} - \omega C \right)}$$

with equation (3.18) and (3.15)

$$\begin{aligned} \tan \psi &= R_L \left( \frac{1}{\omega L} - \omega C \right) = \frac{R}{(1 + \beta)} \left( \frac{1}{\omega L} - \omega C \right) \\ \Rightarrow Z_{cav} &= \frac{R}{1 - i(\beta + 1) \tan \psi} \end{aligned} \quad (3.32)$$

Transformed to the waveguide side we obtain

$$\begin{aligned}
Z'_{cav} &= \frac{1}{N^2} \cdot Z_{cav} \\
\text{or with equation (3.14)} \\
Z'_{cav} &= \frac{\beta Z_0}{R} \cdot Z_{cav} \\
Z'_{cav} &= \frac{\beta Z_0}{1 - i(\beta + 1) \tan \psi}
\end{aligned} \tag{3.33}$$

For the transformed cavity voltage we obtain

$$\mathbf{V}'_{cav} = \mathbf{V}'_{for} + \mathbf{V}'_{ref} \tag{3.34}$$

and for the transformed cavity current

$$\mathbf{I}'_{cav} = \mathbf{I}'_{for} + \mathbf{I}'_{ref} = \frac{\mathbf{V}'_{for}}{Z_0} - \frac{\mathbf{V}'_{ref}}{Z_0}.$$

In the equation

$$\mathbf{V}'_{cav} = Z'_{cav} \cdot \mathbf{I}'_{cav} = \frac{Z'_{cav}}{Z_0} (\mathbf{V}'_{for} - \mathbf{V}'_{ref})$$

$\mathbf{V}'_{ref}$  is eliminated using equation (3.34). Then

$$\begin{aligned}
\mathbf{V}'_{cav} &= \frac{Z'_{cav}}{Z'_{cav} + Z_0} \cdot 2\mathbf{V}'_{for} \\
\mathbf{I}'_{cav} &= \frac{1}{Z'_{cav} + Z_0} \cdot 2\mathbf{V}'_{for}.
\end{aligned}$$

With  $Z'_{cav}$  from equation (3.33), the voltage  $\mathbf{V}'_{cav}$  and current  $\mathbf{I}'_{cav}$  can be expressed as

$$\mathbf{V}'_{cav} = \frac{2\beta}{\beta + 1} \cdot \frac{1}{1 + \tan^2 \psi} \mathbf{V}'_{for} (1 + i \tan \psi) \tag{3.35}$$

$$\mathbf{I}'_{cav} = \frac{2}{\beta + 1} \cdot \frac{1}{1 + \tan^2 \psi} \frac{\mathbf{V}'_{for}}{Z_0} (1 + (\beta + 1) \tan^2 \psi - i\beta \tan \psi). \tag{3.36}$$

The power is given in terms of complex voltages and currents by

$$P = \frac{1}{2} \text{Re}\{\mathbf{V} \cdot \mathbf{I}^*\}$$

where  $\text{Re}\{\}$  is the real part and  $*$  is the complex conjugate. The forward power is with  $\mathbf{I}'_{for} = \frac{\mathbf{V}'_{for}}{Z_0}$

$$P'_{for} = P_{for} = \frac{1}{2} \text{Re}\left\{\frac{\mathbf{V}'_{for} \cdot \mathbf{V}'_{for}^*}{Z_0}\right\} = \frac{|\mathbf{V}'_{for}|^2}{2Z_0}.$$

Furthermore,  $P'_{for}$  is equal to the incident power  $P_{for}$  on the cavity side of the coupler because our assumptions are based on an ideal transformer. This statement is valid for all power calculations (which means that the prime can simply be omitted). The dissipated power in the cavity is given by (with equations (3.35) and (3.36))

$$P'_{diss} = P_{diss} = \frac{1}{2} Re\{\mathbf{V}'_{cav} \cdot \mathbf{I}'_{cav*}\}$$

$$P'_{diss} = P_{diss} = \frac{4\beta}{(\beta+1)^2} \cdot \frac{1}{1+\tan^2\psi} \cdot \frac{|\mathbf{V}'_{for}|^2}{2Z_0} = \frac{4\beta}{(\beta+1)^2} \cdot \frac{1}{1+\tan^2\psi} \cdot P_{for}$$

In principle, the reflected power can be calculated from energy conservation  $P'_{ref} = P'_{for} - P'_{diss}$  but then phase information is lost. Therefore, we determine the reflected voltage  $\mathbf{V}'_{ref}$  and the reflected current  $\mathbf{I}'_{ref}$  first.

$$\mathbf{V}'_{ref} = \mathbf{V}'_{cav} - \mathbf{V}'_{for}$$

$$\mathbf{V}'_{ref} = \frac{1}{\beta+1} \cdot \frac{1}{1+\tan^2\psi} \cdot [(\beta-1) - (\beta+1)\tan^2\psi + i2\beta\tan\psi] \mathbf{V}'_{for}$$

The reflected power is calculated to

$$P'_{ref} = P_{ref} = \frac{1}{2Z_0} Re\{\mathbf{V}'_{ref} \cdot \mathbf{V}'_{ref*}\} \quad (3.37)$$

$$P'_{ref} = P_{ref} = \left(1 - \frac{4\beta}{(\beta+1)^2} \cdot \frac{1}{1+\tan^2\psi}\right) \cdot P_{for} . \quad (3.38)$$

### 3.3.2 Cavity with Beam Loading

The beam is represented by an additional current generator as shown in Figure 3.6b. Since the LCR circuit has been transformed to the waveguide side of the coupler, the beam current has to be transformed as well. A bunched beam provides a pulsed current. Usually, the DC component  $I_{b0}$  is quoted. We have solved the transmission line equation for RF currents and voltages with time dependence  $e^{i\omega t}$ . Consequently, we have to use the Fourier component  $I_b$  of the beam current at the operating frequency  $\omega$ . For bunches whose bunch length is much shorter than the bunch spacing, the Fourier component  $|I_b|$  is twice the DC beam current  $I_{b0}$  (see appendix A.4). It is possible to represent the pulsed beam current by an RF current generator with frequency  $\omega$  if the beam frequency and hence the bunch spacing is synchronized to the same reference frequency as used for the RF generation. Moreover, the bunch length has to be much smaller than the characteristic time constant  $\tau$  of the cavity. The transformation is according to equation (3.3) and (3.14) given by

$$\mathbf{I}'_b = N \cdot \mathbf{I}_b \quad (3.39)$$

$$|\mathbf{I}'_b| = N \cdot |\mathbf{I}_b| = 2 \cdot N \cdot I_{b0}$$

$$|\mathbf{I}'_b| = 2 \sqrt{\frac{R}{\beta Z_0}} I_{b0} . \quad (3.40)$$

The beam current  $\mathbf{I}'_b$  causes a voltage in the transmission line at  $Z'_{cav}$ . This leads to a wave which propagates in backward direction along the transmission line and interferes with the reflected wave which would exist without beam loading. The solutions (equations (3.24) to (3.31)) of the transmission line are still valid with the exception that we have an additional contribution to the reflected current due to the beam. In general, all voltages and currents are complex quantities. To accelerate beam on-crest, the phase between the cavity voltage and the beam current is  $\pi$ . In that case, the beam power is negative, which is equivalent to extracting energy from the cavity by the beam. The beam phase is usually defined as being the difference to this phase  $\pi$ . Currents are represented as complex quantities. Consequently, they have to be added even if the phase difference is  $\pi$  because phase information is already included.

$$\mathbf{V}'_{cav} = \mathbf{V}'_{for} + \mathbf{V}'_{ref} \quad (3.41)$$

$$\begin{aligned} \mathbf{I}'_{cav} &= \mathbf{I}'_{for} + (\mathbf{I}'_{ref} + \mathbf{I}'_b) \\ &= \frac{\mathbf{V}'_{for}}{Z_0} + \left( -\frac{\mathbf{V}'_{ref}}{Z_0} + \mathbf{I}'_b \right) \end{aligned} \quad (3.42)$$

The cavity voltage  $\mathbf{V}'_{cav}$  is related to the current  $\mathbf{I}'_{cav}$  by

$$\mathbf{V}'_{cav} = Z'_{cav} \cdot \mathbf{I}'_{cav} \quad (3.43)$$

Eliminating  $\mathbf{V}'_{ref}$  in equation (3.42) and inserting  $\mathbf{I}'_{cav}$  in equation (3.43) we obtain

$$\begin{aligned} \mathbf{V}'_{cav} &= \frac{Z'_{cav}}{Z'_{cav} + Z_0} \cdot (2\mathbf{V}'_{for} + Z_0 \cdot \mathbf{I}'_b) \\ \mathbf{I}'_{cav} &= \frac{\mathbf{V}'_{cav}}{Z'_{cav}} = \frac{1}{Z'_{cav} + Z_0} \cdot (2\mathbf{V}'_{for} + Z_0 \cdot \mathbf{I}'_b) \end{aligned}$$

Finally, we replace  $Z'_{cav}$  by the explicit expression from equation (3.33).

$$\begin{aligned} \mathbf{V}'_{cav} &= \frac{\beta}{\beta + 1} \cdot \frac{1}{1 + \tan^2 \psi} \cdot (1 + i \tan \psi) \cdot (2\mathbf{V}'_{for} + Z_0 \cdot \mathbf{I}'_b) \\ \mathbf{I}'_{cav} &= \frac{1}{Z_0} \cdot \frac{1}{\beta + 1} \cdot \frac{1}{1 + \tan^2 \psi} \\ &\quad \cdot (1 + (\beta + 1) \tan^2 \psi - i\beta \tan \psi) \cdot (2\mathbf{V}'_{for} + Z_0 \cdot \mathbf{I}'_b) \end{aligned}$$

The cavity voltage consists of two parts: the generator-induced voltage  $\mathbf{V}'_g$  and the beam-induced voltage  $\mathbf{V}'_b$ .

$$\begin{aligned} \mathbf{V}'_{cav} &= \mathbf{V}'_g + \mathbf{V}'_b \\ \text{with } \mathbf{V}'_g &= \frac{\beta}{\beta + 1} \cdot \frac{1}{1 + \tan^2 \psi} \cdot (1 + i \tan \psi) \cdot 2\mathbf{V}'_{for} \\ \mathbf{V}'_b &= \frac{\beta}{\beta + 1} \cdot \frac{1}{1 + \tan^2 \psi} \cdot (1 + i \tan \psi) \cdot Z_0 \cdot \mathbf{I}'_b \end{aligned}$$

It has to be kept in mind that there is no reflected wave if we only have a beam current but no generator current. In this case, the stored power of the beam is coupled out and propagates along the transmission line. Nevertheless, the backward travelling wave is labeled with the index of a reflected wave because it is detected in the same way as a reflected wave. The reflected voltage and current can be calculated as follows

$$\begin{aligned}\mathbf{V}'_{ref} &= \frac{\beta}{\beta+1} \cdot \frac{1}{1+\tan^2\psi} \cdot (1+i\tan\psi) \cdot \left( \frac{(\beta-1)+i(\beta+1)\tan\psi}{\beta} \mathbf{V}'_{for} + Z_0 \cdot \mathbf{I}'_b \right) \\ \mathbf{I}'_{ref} &= -\frac{\mathbf{V}'_{ref}}{Z_0}.\end{aligned}$$

All the currents and voltages are calculated on the waveguide side of the coupler. In reality, however, we are interested in the cavity voltage seen by the beam. Therefore, it is useful to transform the voltages and currents back to the cavity side. For convenience sake, we will express the forward voltage  $\mathbf{V}'_{for}$  in terms of the generator power  $P'_{for} = P_g$ . The transformation equations are (with  $N$  as the coupler transformation ratio,  $N^2 = \frac{R}{\beta Z_0}$ )

$$\begin{array}{ccc}\text{waveguide side of coupler} & & \text{cavity side of coupler} \\ \text{voltages: } \mathbf{V}' & \longrightarrow & \mathbf{V} = N \cdot \mathbf{V}' \\ \text{currents: } \mathbf{I}' & \longrightarrow & \mathbf{I} = (1/N) \cdot \mathbf{I}' .\end{array}$$

The transformed voltages and currents are calculated to

$$\begin{aligned}\mathbf{V}_{for} &= \frac{R}{\beta} \mathbf{I}_{for} ; & |\mathbf{V}_{for}| = V_{for} &= \sqrt{\frac{2R \cdot P_g}{\beta}} \\ \mathbf{V}_{ref} &= \frac{R}{\beta+1} \cdot \frac{1}{1+\tan^2\psi} \cdot (1+i\tan\psi) \cdot \left( \frac{(\beta-1)+i(\beta+1)\tan\psi}{\beta} \mathbf{I}_g + \mathbf{I}_b \right) \\ \mathbf{V}_{cav} &= \frac{R}{\beta+1} \cdot \frac{1}{1+\tan^2\psi} \cdot (1+i\tan\psi) \cdot (2\mathbf{I}_g + \mathbf{I}_b) \\ &= \frac{\beta}{\beta+1} \cdot \frac{1}{1+\tan^2\psi} \cdot (1+i\tan\psi) \cdot \left( 2\mathbf{V}_{for} + \frac{R}{\beta} \mathbf{I}_b \right) \\ &= \frac{\beta}{\beta+1} \cdot \cos\psi \cdot e^{i\psi} \cdot \left( 2\mathbf{V}_{for} + \frac{R}{\beta} \mathbf{I}_b \right) \\ \mathbf{V}_g &= \frac{R}{\beta+1} \cdot \frac{1}{1+\tan^2\psi} \cdot (1+i\tan\psi) \cdot 2\mathbf{I}_g = R_L (1 + e^{i2\psi}) \cdot \mathbf{I}_g \\ &= R_L 2\mathbf{I}_g \cdot \cos\psi \cdot e^{i\psi} = \mathbf{V}_{gr} \cdot \cos\psi \cdot e^{i\psi} \\ \mathbf{V}_{gr} &= 2R_L \mathbf{I}_g \quad (\text{on-resonance amplitude due to generator}) \\ \mathbf{V}_b &= \frac{R}{\beta+1} \cdot \frac{1}{1+\tan^2\psi} \cdot (1+i\tan\psi) \cdot \mathbf{I}_b = R_L \frac{1}{2} (1 + e^{i2\psi}) \cdot \mathbf{I}_b \\ &= R_L \mathbf{I}_b \cdot \cos\psi \cdot e^{i\psi} = \mathbf{V}_{br} \cdot \cos\psi \cdot e^{i\psi} \\ \mathbf{V}_{br} &= R_L \mathbf{I}_b \quad (\text{on-resonance amplitude due to beam})\end{aligned}$$

$$\begin{aligned}
\mathbf{I}_g &= \mathbf{I}_{for} = \frac{\beta}{R} \mathbf{V}_{for} ; & |\mathbf{I}_g| &= |\mathbf{I}_{for}| = I_g = I_{for} = \sqrt{\frac{2\beta \cdot P_g}{R}} \\
\mathbf{I}_{ref} &= -\frac{1}{N^2 Z_0} \mathbf{V}_{ref} = -\frac{\beta}{R} \mathbf{V}_{ref} \\
\mathbf{I}_{cav} &= \frac{1}{\beta + 1} \cdot \frac{1}{1 + \tan^2 \psi} \cdot (1 + (\beta + 1) \tan^2 \psi - i\beta \tan \psi) \cdot (2\mathbf{I}_g + \mathbf{I}_b)
\end{aligned}$$

The general formula for the power emitted by a cavity with beam loading is given by

$$\begin{aligned}
P_{ref} &= \frac{1}{2Z_0} \operatorname{Re}\{\mathbf{V}'_{ref} \cdot \mathbf{V}_{ref}^*\} & (3.44) \\
&= \frac{1}{(\beta + 1)^2} \cdot \frac{1}{1 + \tan^2 \psi} \cdot \left| ((\beta - 1) + i(\beta + 1) \tan \psi) \sqrt{P_g} \cdot e^{-i\Theta} + \sqrt{\frac{\beta R}{2}} \mathbf{I}_b \right|^2 .
\end{aligned}$$

The angle  $\Theta$  is the angle between the positive direction of the real axis and the generator current  $\mathbf{I}_g$ . It is determined by  $\mathbf{V}_g$ ,  $\mathbf{V}_b$  and  $\mathbf{V}_{cav}$  (see Figure 3.9). In terms of amplitudes it can be expressed by

$$\cos \Theta = \frac{V_g^2 + V_b^2 - V_{cav}^2}{2V_g V_b}$$

With the formulas

$$\begin{aligned}
V_b &= R_L I_b \cos \psi ; & V_g &= 2R_L I_g \cos \psi ; \\
V_{acc} &= V_{cav} \cos \phi_b ; & I_b &= 2I_{b0}
\end{aligned}$$

we get

$$\cos \Theta = \frac{I_g^2 + I_{b0}^2 - \frac{V_{acc}^2}{(2R_L \cos \psi \cos \phi_b)^2}}{2I_g I_{b0}} .$$

For superconducting cavities, the description of the voltages, currents and powers in terms of  $\beta$  is not very useful. Since the external  $Q_{ext}$  is much smaller than the unloaded  $Q_0$ , nearly all the properties depend only on the loaded  $Q_L$ . For the special case of  $Q_0 \gg Q_{ext}$  (which means  $\beta \gg 1$ ), the formulas can be expressed by the quantities  $Q_L$  and  $\left(\frac{r}{Q}\right)$  using the approximations

$$\frac{R}{\beta} \approx \frac{R}{\beta + 1} = \frac{1}{2} \left(\frac{r}{Q}\right) Q_L ; \quad \frac{\beta}{\beta + 1} \approx 1$$

Then, we get

$$\begin{aligned}
\mathbf{V}_{for} &= \frac{1}{2} \left(\frac{r}{Q}\right) Q_L \cdot \mathbf{I}_{for} ; & |\mathbf{V}_{for}| &= V_{for} = \sqrt{\left(\frac{r}{Q}\right) Q_L \cdot P_g} \\
\mathbf{V}_{ref} &= \frac{1}{2} \frac{1}{1 + \tan^2 \psi} \cdot (1 + i \tan \psi) \cdot \left(\frac{r}{Q}\right) Q_L \cdot ((1 + i \tan \psi) \mathbf{I}_g + \mathbf{I}_b)
\end{aligned}$$

$$\begin{aligned}
\mathbf{V}_{cav} &= \frac{1}{2} \frac{1}{1 + \tan^2 \psi} \cdot (1 + i \tan \psi) \cdot \left(\frac{r}{Q}\right) Q_L \cdot (2\mathbf{I}_g + \mathbf{I}_b) \\
\mathbf{V}_{cav} &= \mathbf{V}_g + \mathbf{V}_b \\
\mathbf{V}_g &= \frac{1}{1 + \tan^2 \psi} \cdot (1 + i \tan \psi) \cdot \left(\frac{r}{Q}\right) Q_L \cdot \mathbf{I}_g = \cos \psi \cdot e^{i\psi} \cdot \left(\frac{r}{Q}\right) Q_L \cdot \mathbf{I}_g \\
&= \cos \psi \cdot e^{i\psi} \mathbf{V}_{gr} = \frac{1}{2} (1 + e^{i2\psi}) \cdot \mathbf{V}_{gr} \\
V_g &= \frac{1}{\sqrt{1 + \tan^2 \psi}} \cdot 2 \sqrt{\left(\frac{r}{Q}\right) Q_L \cdot P_g} = 2 \cos \psi \cdot \sqrt{\left(\frac{r}{Q}\right) Q_L \cdot P_g} \\
\mathbf{V}_{gr} &= 2 \mathbf{V}_{for} = \left(\frac{r}{Q}\right) Q_L \cdot \mathbf{I}_g \quad (\text{on-resonance amplitude due to generator}) \\
\mathbf{V}_b &= \frac{1}{2} \frac{1}{1 + \tan^2 \psi} \cdot (1 + i \tan \psi) \cdot \left(\frac{r}{Q}\right) Q_L \cdot \mathbf{I}_b = \frac{1}{2} \cos \psi \cdot e^{i\psi} \cdot \left(\frac{r}{Q}\right) Q_L \cdot \mathbf{I}_b \\
&= \cos \psi \cdot e^{i\psi} \mathbf{V}_{br} = \frac{1}{2} (1 + e^{i2\psi}) \cdot \mathbf{V}_{br} \\
\mathbf{V}_{br} &= \frac{1}{2} \left(\frac{r}{Q}\right) Q_L \cdot \mathbf{I}_b \quad (\text{on-resonance amplitude due to beam}) \\
\mathbf{I}_g &= \mathbf{I}_{for} = \frac{2\mathbf{V}_{for}}{\left(\frac{r}{Q}\right) Q_L} ; \quad |\mathbf{I}_g| = |\mathbf{I}_{for}| = I_g = I_{for} = 2 \sqrt{\frac{P_g}{\left(\frac{r}{Q}\right) Q_L}} \\
\mathbf{I}_{ref} &= -\frac{1}{1 + \tan^2 \psi} \cdot (1 + i \tan \psi) \cdot ((1 + i \tan \psi)\mathbf{I}_g + \mathbf{I}_b) \\
\mathbf{I}_{cav} &= -i \frac{\tan \psi}{1 + \tan^2 \psi} \cdot (1 + i \tan \psi) \cdot (2\mathbf{I}_g + \mathbf{I}_b) \\
&\text{and corresponding to equation (3.42)} \\
\mathbf{I}_{cav} &= \mathbf{I}_{for} + (\mathbf{I}_{ref} + \mathbf{I}_b) .
\end{aligned}$$

The generator- and beam-induced voltages vary as a function of the tuning angle  $\psi$  along a circle in the complex plane (Figure 3.8). The quantities  $\mathbf{V}_{gr}$  and  $\mathbf{V}_{br}$  represent the voltages generated by the generator current and by the beam current, respectively, if the cavity is tuned on resonance ( $\psi = 0$ ). In the case of superconducting cavities with  $Q_0 \gg Q_{ext}$ , the voltage  $\mathbf{V}_{gr}$  is twice that of the incident wave  $\mathbf{V}_{for}$  of steady-state. The beam current  $\mathbf{I}_{b0}$  is represented as a complex quantity. In accelerator physics, the beam phase  $\phi_b$  is defined as the angle between the beam current with respect to the cavity voltage  $\mathbf{V}_{cav}$ . The different voltages and angles are displayed in Figure 3.9. In this diagram, the phase of the beam current has been chosen in such a way that the vector  $\mathbf{I}_b$  is directed along the negative real axis. Operating off resonance introduces the tuning angle  $\psi$  between generator current and generator voltage and between beam current and beam voltage. The generator and beam voltages add up to the cavity voltage  $\mathbf{V}_{cav}$ . The accelerating

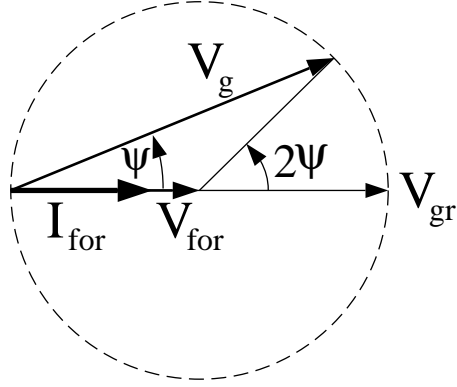


Figure 3.8: Induced cavity voltage as a function of the tuning angle  $\psi$ . The voltage induced by a generator current  $\mathbf{I}_g$  on resonance is denoted by an index 'r'. This applies to both generator- and beam-induced voltages. In the case of superconducting cavities with  $Q_0 \gg Q_{ext}$ , the voltage  $\mathbf{V}_{gr}$  is twice that of the incident wave  $\mathbf{V}_{for}$ .

voltage for the beam is then given by the projection on the direction opposite to  $\mathbf{I}_b$ .

$$V_{acc} = |\mathbf{V}_{cav}| \cdot \cos \phi_b .$$

Now, the reflected voltage can be inserted since the cavity voltage is a superposition of forward and reflected voltage. The angle  $\Theta$  defines the angle of the incident wave (forward wave) with respect to the negative beam current and can be varied by the control system.

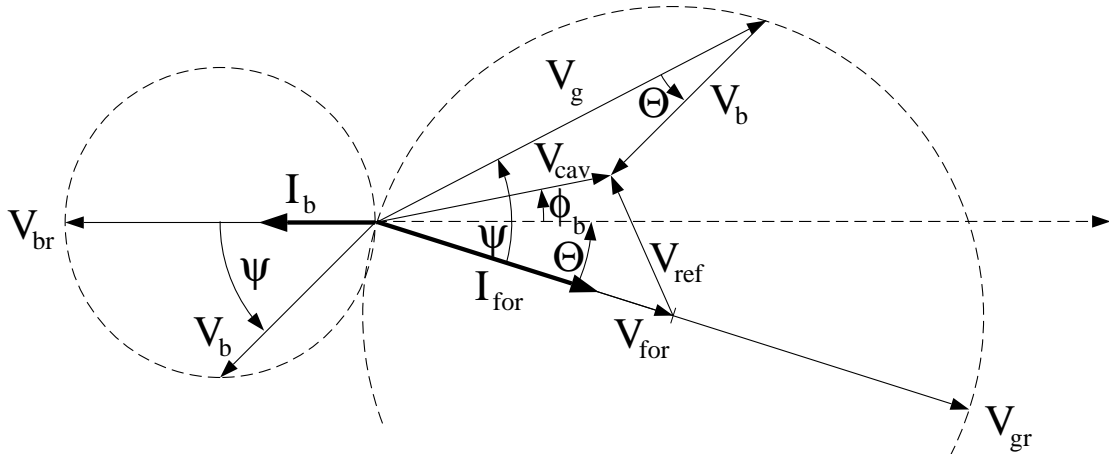


Figure 3.9: Vector diagram of generator- and beam-induced voltages in a detuned cavity. The angle  $\phi_b$  denotes the beam phase and  $\psi$  the tuning angle.

In the case of superconducting cavities with strong external coupling ( $Q_0 \gg Q_{ext}$ ), the reflected power (equation (3.44)) can be approximated by

$$P_{ref} = \frac{1}{1 + \tan^2 \psi} \cdot \left| (1 + i \tan \psi) \sqrt{P_g} \cdot e^{-i\Theta} + \frac{1}{2} \sqrt{\left(\frac{r}{Q}\right) Q_L \mathbf{I}_b} \right|^2$$

The beam current  $\mathbf{I}_b$  is chosen along the negative real axis. The incident wave (forward current) has an angle of  $-\Theta$  with respect to the real axis as seen in Figure 3.9. For a given beam current  $I_{b0}$ , beam phase  $\phi_b$ , tuning angle  $\psi$  and cavity voltage  $|\mathbf{V}_{cav}| = V_{cav}$ , the generator power is calculated to (see appendix A.5).

$$P_g = \frac{V_{cav}^2}{R_L} \frac{\beta + 1}{8\beta} \left( \left[ 1 + \frac{2 R_L I_{b0}}{V_{cav}} \cos \phi_b \right]^2 + \left[ \tan \psi + \frac{2 R_L I_{b0}}{V_{cav}} \sin \phi_b \right]^2 \right) \quad (3.45)$$

In the case of superconducting cavities with  $\beta \gg 1$ , this formula can be simplified to

$$P_g = \frac{V_{cav}^2}{\left(\frac{r}{Q}\right) Q_L} \frac{1}{4} \left( \left[ 1 + \frac{\left(\frac{r}{Q}\right) Q_L I_{b0}}{V_{cav}} \cos \phi_b \right]^2 + \left[ \frac{\Delta f}{f_{1/2}} + \frac{\left(\frac{r}{Q}\right) Q_L I_{b0}}{V_{cav}} \sin \phi_b \right]^2 \right) \quad (3.46)$$

The quantity  $f_{1/2} = \frac{f}{2Q_L}$  is the bandwidth of the cavity. As far as TESLA/TTF is concerned, two special cases exist.

$V_{cav} = 25 \text{ MV}$ ,  $Q_L = 3 \cdot 10^6$ ; no beam:

$$P_g = 50 \text{ kW} \cdot \left( 1 + \left( \frac{\Delta f}{f_{1/2}} \right)^2 \right)$$

$V_{cav} = 25 \text{ MV}$ ,  $Q_L = 3 \cdot 10^6$ ;  $I_b = 8 \text{ mA}$ ;  $\phi_b = 0^\circ$  (on-crest):

$$P_g = 50 \text{ kW} \cdot \left( 4 + \left( \frac{\Delta f}{f_{1/2}} \right)^2 \right)$$

Detuning of the cavity by one bandwidth (for example due to Lorentz force) increases the required power by 25%. In storage rings, it is necessary to operate the cavities off-crest by an angle of  $\phi_b$  to guarantee stability with respect to synchrotron oscillations. In a linear accelerator, it can also be necessary to inject beam with a phase of  $\phi_b$  to minimize the energy spread due to wakefields. In both cases, the required power can be minimized by means of detuning the cavity. Moreover, the coupling of the RF generator to the cavity has to be optimized so as to ensure minimum RF generator power.

Firstly, the optimum tuning has to be found. The second bracket in equation (3.45) depends on the tuning angle  $\psi$ . If the tuning is chosen such that the second bracket vanishes, the required power is minimized.

$$\tan \psi_{opt} = - \frac{2 R_L I_{b0}}{V_{cav}} \sin \phi_b = - \frac{2}{\beta + 1} \frac{R_L I_{b0}}{V_{cav}} \sin \phi_b . \quad (3.47)$$

Then the generator power at optimum tuning becomes

$$(P_g)_{opt} = \frac{V_{cav}^2}{R_L} \frac{\beta + 1}{8\beta} \left[ 1 + \frac{2 R_L I_{b0}}{V_{cav}} \cos \phi_b \right]^2 .$$

Differentiating this expression with respect to the coupling parameter  $\beta$ , the condition for optimum coupling is obtained by

$$\beta_{opt} = 1 + \frac{2 R_L I_{b0}}{V_{cav}} \cos \phi_b$$

The minimum generator power to maintain a cavity voltage  $V_{cav}$  is

$$(P_g)_{min} = \beta_{opt} \cdot \frac{V_{cav}^2}{2 R} .$$

The optimum tuning angle of the cavity can therefore be expressed by

$$\tan \psi_{opt} = - \frac{\beta_{opt} - 1}{\beta_{opt} + 1} \tan \phi_b .$$

In the case of superconducting cavities, we get the simplifications

$$\begin{aligned} \tan \psi_{opt} &= 2Q_L \frac{\Delta\omega_{opt}}{\omega} = - \frac{\left(\frac{r}{Q}\right) Q_L I_{b0}}{V_{cav}} \sin \phi_b \\ \frac{\Delta\omega_{opt}}{\omega} &= - \frac{\left(\frac{r}{Q}\right) I_{b0}}{2V_{cav}} \sin \phi_b \\ (Q_L)_{opt} &= \frac{V_{cav}}{\left(\frac{r}{Q}\right) I_{b0} \cos \phi_b} \\ \tan \psi_{opt} &= - \tan \phi_b \quad \iff \quad \psi_{opt} = -\phi_b \\ (P_g)_{min} &= \frac{V_{cav}^2}{\left(\frac{r}{Q}\right) (Q_L)_{opt}} = V_{cav} \cdot I_{b0} \cdot \cos \phi_b \end{aligned}$$

The optimum coupling, i.e. the optimum loaded  $Q_L$ , has to be adjusted in such a way that the beam-induced voltage equals the cavity voltage. The minimum required power is no more than the power transferred to the beam since the dissipated power can be neglected. For TESLA/TTF the optimum parameters are provided in table 3.1. The cavity voltage is calculated with  $V_{cav} = E_{acc} \cdot l$  and  $l = 1.038$  m.

### 3.3.3 Transient Behavior of a Pulsed RF Cavity with Beam Loading

In the previous section, all formulas for the steady-state have been derived, assuming that both the RF generator and the beam current have been turned on for a long time

	TTF	TTF	TESLA 500	TESLA 500
beam current [mA]	8.0	8.0	8.2	8.2
$E_{acc}$ [MV/m]	15	25	25	40
$(Q_L)_{opt}$	$1.857 \cdot 10^6$ ( $\phi_b = 0^\circ$ )	$3.125 \cdot 10^6$ ( $\phi_b = 0^\circ$ )	$3.024 \cdot 10^6$ ( $\phi_b = -3^\circ$ )	$4.838 \cdot 10^6$ ( $\phi_b = -3^\circ$ )
bandwidth $f_{1/2}$ [Hz]	350	208	215	134
$\Delta f_{opt} = \frac{\Delta\omega_{opt}}{2\pi}$ [Hz]	0	0	+11	+7
$(P_g)_{min}$ per cavity [kW]	124	206	211	337

Table 3.1: Optimum loaded quality factor  $Q_L$  for TTF/TESLA 500 machine parameters. The optimum detuning of the cavity refers to continuous-wave operation. Lorentz force detuning requires a different, gradient-dependent pre-detuning in order to minimize the peak power during the RF pulse. The beam phases have been calculated in [Mos 95].

compared to the characteristic filling time of a cavity. Now, the transient behavior of a cavity will be derived when the RF generator is turned on or off, and the beam is injected after some delay. The starting point is the differential equation for a driven LCR circuit (see equation (3.16)).

$$\ddot{\mathbf{V}}(t) + \frac{\omega_0}{Q_L} \dot{\mathbf{V}}(t) + \omega_0^2 \mathbf{V}(t) = \frac{\omega_0 R_L}{Q_L} \dot{\mathbf{I}}(t) \quad (3.48)$$

A cavity is a weakly damped system ( $\frac{\omega_0}{Q_L} \ll \omega_0$ ). The resonance frequency of this system is in very good approximation  $\omega_{res} = \omega_0$ .

$$\omega_{res} = \omega_0 \sqrt{1 - \frac{1}{4Q_L^2}} \approx \omega_0$$

In the case of TESLA, the loaded  $Q_L$  is in the order of  $3 \cdot 10^6$ . The resonance frequency  $f_0 = 1.3$  GHz of the unloaded cavity changes only by 0.024 Hz. The driving current  $\mathbf{I}_g$  of the RF generator and the Fourier component  $\mathbf{I}_b$  of the pulsed beam are harmonic with a time dependence  $e^{i\omega t}$ . Therefore, we separate the fast RF oscillation from the slowly changing amplitudes and phases or from the real and imaginary parts of the field vector.

$$\begin{aligned} \mathbf{V}(t) &= (V_r(t) + iV_i(t)) \cdot e^{i\omega t} \\ \mathbf{I}(t) &= (I_r(t) + iI_i(t)) \cdot e^{i\omega t} \end{aligned}$$

When we insert this into the differential equation (3.48) and neglect the second-order time derivatives of  $\mathbf{V}$ , we obtain the first-order cavity differential equation for the envelope (see appendix A.6).

$$\begin{aligned}\dot{V}_r + \omega_{1/2} V_r + \Delta\omega V_i &= R_L \omega_{1/2} I_r \\ \dot{V}_i + \omega_{1/2} V_i - \Delta\omega V_r &= R_L \omega_{1/2} I_i\end{aligned}$$

In this,  $\omega_{1/2} = \frac{\omega_0}{2Q_L}$  is the bandwidth and  $\Delta\omega = \omega_0 - \omega$  the detuning of the cavity. In state space formalism, the differential equation is written as

$$\frac{d}{dt} \begin{pmatrix} V_r \\ V_i \end{pmatrix} = \begin{pmatrix} -\omega_{1/2} & -\Delta\omega \\ \Delta\omega & -\omega_{1/2} \end{pmatrix} \cdot \begin{pmatrix} V_r \\ V_i \end{pmatrix} + \begin{pmatrix} R_L \omega_{1/2} & 0 \\ 0 & R_L \omega_{1/2} \end{pmatrix} \cdot \begin{pmatrix} I_r \\ I_i \end{pmatrix}. \quad (3.49)$$

With the matrix definition

$$\begin{aligned}\mathbf{A} &= \begin{pmatrix} -\omega_{1/2} & -\Delta\omega \\ \Delta\omega & -\omega_{1/2} \end{pmatrix} \\ \mathbf{B} &= \begin{pmatrix} R_L \omega_{1/2} & 0 \\ 0 & R_L \omega_{1/2} \end{pmatrix} \\ x &= \begin{pmatrix} V_r \\ V_i \end{pmatrix} \\ u &= \begin{pmatrix} I_r \\ I_i \end{pmatrix}\end{aligned}$$

the differential equation becomes

$$\dot{x}(t) = \mathbf{A} \cdot x(t) + \mathbf{B} \cdot u(t).$$

With  $t_0 = 0$  the general solution is

$$x(t) = e^{\mathbf{A} \cdot t} \cdot x(0) + \int_0^t e^{\mathbf{A} \cdot (t-t')} \cdot \mathbf{B} \cdot u(t') dt'$$

where  $e^{\mathbf{A} \cdot t}$  is the matrix exponential defined by

$$e^{\mathbf{A} \cdot t} = \mathbf{1} + \mathbf{A}t + \frac{1}{2!} \mathbf{A}^2 t^2 + \frac{1}{3!} \mathbf{A}^3 t^3 + \dots$$

and  $x(0) = \begin{pmatrix} V_r(0) \\ V_i(0) \end{pmatrix}$  is the initial state at  $t_0 = 0$ . For matrix  $\mathbf{A}$ , we get

$$e^{\mathbf{A} \cdot t} = e^{-\omega_{1/2} t} \begin{pmatrix} \cos(\Delta\omega t) & -\sin(\Delta\omega t) \\ \sin(\Delta\omega t) & \cos(\Delta\omega t) \end{pmatrix}.$$

In the special case of constant input power being provided, i.e. constant current  $u = \begin{pmatrix} I \\ 0 \end{pmatrix}$  (for  $t > 0$ ), the general solution can be calculated explicitly and is

$$\begin{pmatrix} V_r \\ V_i \end{pmatrix} = \frac{R_L \cdot I \cdot \omega_{1/2}}{\omega_{1/2}^2 + \Delta\omega^2} \cdot \left( e^{-\omega_{1/2}t} \begin{pmatrix} -\omega_{1/2} \cos \Delta\omega t + \Delta\omega \sin \Delta\omega t \\ -\omega_{1/2} \sin \Delta\omega t - \Delta\omega \cos \Delta\omega t \end{pmatrix} + \begin{pmatrix} \omega_{1/2} \\ \Delta\omega \end{pmatrix} \right).$$

For  $t \rightarrow \infty$ , the solution merges into the steady-state

$$\begin{pmatrix} V_r \\ V_i \end{pmatrix}_{t \rightarrow \infty} = \frac{R_L \cdot I \cdot \omega_{1/2}}{\omega_{1/2}^2 + \Delta\omega^2} \begin{pmatrix} \omega_{1/2} \\ \Delta\omega \end{pmatrix}$$

which can be expressed as a complex quantity

$$\begin{aligned} \mathbf{V} &= \frac{1}{1 + \tan^2 \psi} (1 + i \tan \psi) R_L \cdot I \\ \tan \psi &= \frac{\Delta\omega}{\omega_{1/2}} = 2Q_L \frac{\Delta\omega}{\omega_0} \\ |\mathbf{V}| &= |V_r + i V_i| = \frac{R_L \cdot I}{\sqrt{1 + \tan^2 \psi}}. \end{aligned}$$

A comparison with the steady-state equations (see page 35,  $\mathbf{V}_{cav}$ ) shows that the driving current for a cavity is

$$I = |(2\mathbf{I}_g + \mathbf{I}_b)|.$$

In the case of on-crest acceleration ( $\phi_b = 0$ , i.e.  $\mathbf{I}_b$  is opposite to  $\mathbf{V}_{cav}$ ) and on-resonance operation ( $\tan \psi = 0$ ), the absolute value of the current can be simplified to  $I = (2I_g - I_b) = 2(I_g - I_{b0})$ . With the TESLA design parameter of  $V_{cav} = 25$  MV, loaded  $Q_L = 3 \cdot 10^6$  and a DC beam current of  $I_{b0} = 8$  mA, we get  $I = 16$  mA and  $I_g = 16$  mA. Filling a TESLA cavity with RF power of 200 kW ( $\Rightarrow I = 16$  mA) leads to the plot in Figure 3.10. It shows the transient behavior of the cavity displayed in a polar plot by real and imaginary parts of the accelerating field. The different curves represent various values of detuning  $\Delta\omega$ . The crosses indicate the cavity field at the injection time  $t_{inj}$  (defined later on). If no beam is injected, the cavity field increases to the steady-state voltage indicated by the dotted circle. It should be pointed out that the cavity field rises always in the same direction during the first microseconds irrespective of detuning. It is the direction of the driving RF current which has to be chosen along the real axis. This effect is used to determine the phase offset of a cavity due to an arbitrary cable length of the field probe antenna (see chapter 4.4).

Finally, the case of the operation of a resonator on resonance ( $\Delta\omega = 0$ ) will be considered in more detail. Moreover, beam is accelerated on-crest. The complex voltages and currents are written as amplitudes because of the simplified phase relation ( $\phi_b = \Theta = 0^\circ$ ). Filling a cavity with constant forward power results in an exponential increase of the cavity field.

$$V_g = R_L \cdot 2 I_g \left(1 - e^{-\frac{t}{\tau}}\right) \quad (3.50)$$

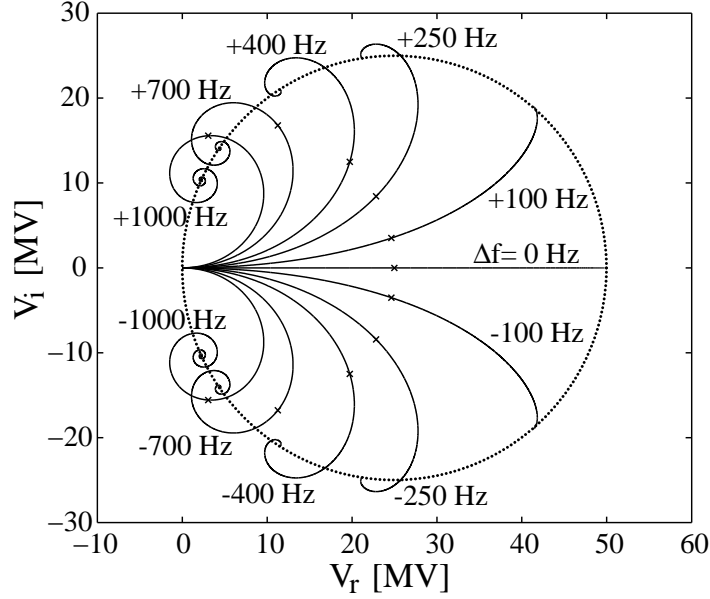


Figure 3.10: Transient behavior of a TESLA cavity with constant input power ( $P_{for} = 200 \text{ kW}$ ;  $Q_L = 3 \cdot 10^6$ ) for selected detuning. The dotted circle indicates the steady-state voltage as a function of the tuning angle  $\psi$ . The crosses mark the cavity field at injection time  $t_{inj} = 510 \mu\text{s}$ .

The same is valid for a beam current of  $I_{b0}$  injected at a time  $t_{inj}$ .

$$V_b = -R_L \cdot 2 I_{b0} \left( 1 - e^{-\frac{1}{\tau}(t-t_{inj})} \right)$$

The time constant  $\tau$  of the cavity is

$$\tau = \frac{1}{\omega_{1/2}} = \frac{2Q_L}{\omega_0} .$$

Due to the linearity of the differential equation, the total cavity voltage is a superposition of RF generator voltage (induced by  $I_g$  for  $t > 0$ ) and beam voltage (induced by the beam current  $I_{b0}$  for  $t > t_{inj}$ ).

$$V_{cav}(t) = V_g + V_b = R_L \cdot 2 I_g \left( 1 - e^{-\frac{t}{\tau}} \right) - R_L \cdot 2 I_{b0} \left( 1 - e^{-\frac{1}{\tau}(t-t_{inj})} \right) \quad \text{for } t > t_{inj}$$

In superconducting cavities, where the generator power is nearly completely transferred to the beam, the injection time can be chosen in such a way as to ensure immediate steady-state condition. This is achieved if the injection takes place when the cavity field has reached half of its maximum.

$$t_{inj} = \ln 2 \cdot \tau$$

The cavity field is then

$$V_{cav}(t) = R_L \cdot I_g = R_L \cdot 2 I_{b0} \quad \text{for } t > t_{inj} .$$

Turning off the RF power at the end of the beam macro pulse yields an exponential decay of the cavity field.

$$V_{cav}(t) = R_L \cdot I_g \cdot e^{-(t-t_{off})/\tau} \quad \text{for } t > t_{off} \quad (3.51)$$

This behavior is shown in Figure 3.11. Energy conservation yields

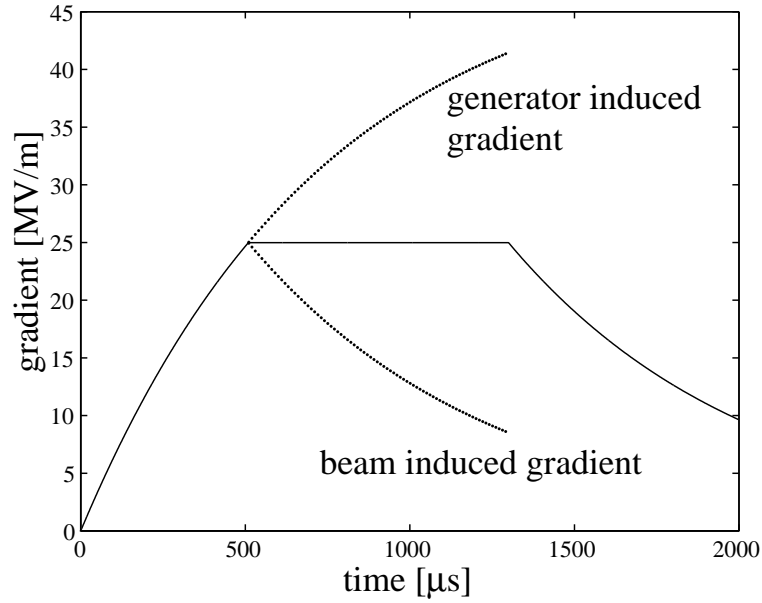


Figure 3.11: Accelerating gradient of a TESLA cavity with constant input power ( $P_{for} = 200$  kW;  $Q_L = 3 \cdot 10^6$ ) being supplied for  $1310 \mu s$  and beam between  $510 \mu s$  and  $1310 \mu s$ . The field induced by the beam cancels the exponential increase of the generator-induced gradient, resulting in a so-called *flattop* operation. Turning off both RF generator and beam current at  $t = 1310 \mu s$  results in an exponential decay of the cavity field.

$$P_g = P_{diss} + P_{ref} + P_{beam} + \frac{dW}{dt} .$$

In contrast to the other terms, the dissipated power can be neglected in the case of superconducting cavities. The beam power is simply  $P_{beam} = V_{cav} \cdot I_{b0}$ , while  $dW/dt$  describes the change of the stored energy in the cavity ( $W = \frac{V_{cav}^2}{(r/Q) \cdot \omega_0}$ ). During the filling

of a cavity with constant input power, the cavity voltage is a superposition of forward and reflected voltage. With the solution from equation (3.50), the reflected voltage is

$$\begin{aligned} V_{ref}(t) &= V_{cav}(t) - V_{for} \\ &= R_L \cdot 2 I_g \left(1 - e^{-\frac{t}{\tau}}\right) - R_L \cdot I_g \end{aligned}$$

and the reflected power

$$P_{ref}(t) = \frac{V_{ref}^2(t)}{R_L} \quad \text{for } 0 \leq t < t_{inj} .$$

Injecting a beam at  $t = t_{inj}$ , when the reflected power approaches zero, brings the whole system in steady-state condition with no reflected power. The turning off of both the RF power and the beam results in

$$P_{ref} = - \frac{dW}{dt} = - \frac{2V_{cav}}{\left(\frac{r}{Q}\right) \cdot \omega_0} \frac{dV_{cav}}{dt} = \left(\frac{r}{Q}\right) \cdot Q_L \cdot I_g^2 \cdot e^{-2t/\tau}$$

or expressed in terms of amplitude (with equation (3.51))

$$V_{ref}(t) = V_{cav}(t) = R_L I_g \cdot e^{-(t-t_{off})/\tau} \quad \text{for } t > t_{off} .$$

The vector diagram of the voltages and the corresponding reflected power is shown in Figure 3.12. The phase of the reflected wave after turning off the RF is phase shifted by  $180^\circ$  compared with that during filling of the cavity.

### 3.4 Mechanical Model for Lorentz Force Detuning

A standing electromagnetic wave in a metallic resonator exerts pressure on the surrounding resonator walls. This radiation pressure is [Beck]

$$P_s = \frac{1}{4} \left( \mu_0 |\vec{H}|^2 - \epsilon_0 |\vec{E}|^2 \right) .$$

The quantities  $\vec{H}$  and  $\vec{E}$  denote the magnetic and electric field on the walls. The radiation pressure results in a deformation of the cavity and consequently in a change in the resonator volume by  $\Delta V$ . The resonance frequency is shifted by a change in volume according to [Sla]

$$\frac{\omega_0 - \omega}{\omega_0} = \frac{\Delta V}{\int_V \left( \epsilon_0 |\vec{E}_0|^2 + \mu_0 |\vec{H}_0|^2 \right) dV} , \quad (3.52)$$

where  $\vec{E}_0$  and  $\vec{H}_0$  are the unperturbed fields. The highest pressure is to be found in regions with high fields. The high electric field near the iris contracts the cell (negative volume

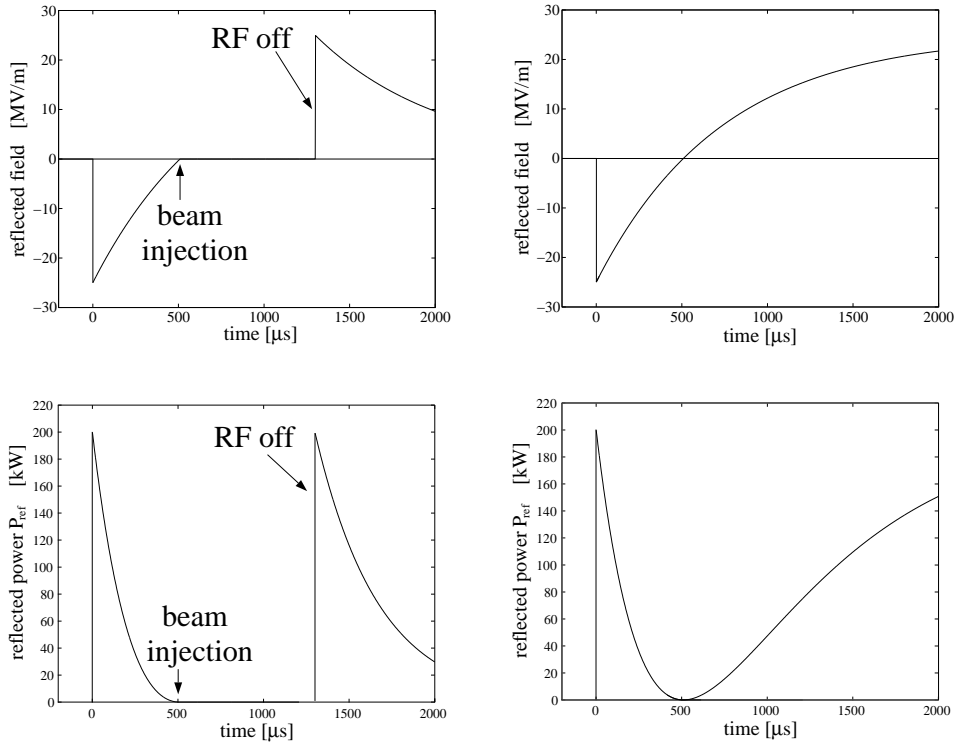
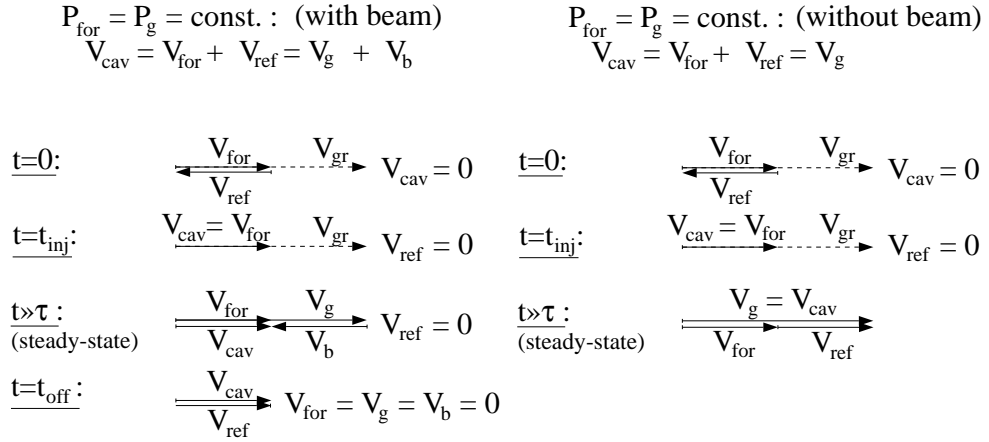


Figure 3.12: Vector diagram of voltages and reflected power ( $P_{for} = 200 \text{ kW}$ ;  $Q_L = 3 \cdot 10^6$ ).

Left side: The beam is injected at time  $t_{inj} = 510 \mu\text{s}$ . RF generator and beam current are turned off at  $t = 1300 \mu\text{s}$ .

Right Side: No beam injection and no power reduction. The cavity field rises to 50 MV/m. At the injection time  $t_{inj}$ , the reflected power has a phase jump of  $180^\circ$ .

change), while the high magnetic field around the equator results in a pressure which is directed outwards (positive volume change). Both effects yield a decreasing resonance frequency as seen in equation (3.52). To reduce this deformation, the TESLA cavities are stiffened. Figure 3.13 shows the deformation of a cavity cell at a gradient of 25 MV/m with and without stiffening rings. The deformation near the iris is negligible due to the stiffening ring, but it remains nearly the same as in the unstiffened cell near the equator. Assuming a linear dependence of the volume change on the radiation pressure, detuning in steady-state operation is proportional to the square of the cavity field.

$$\Delta f_0 = (f_0)_2 - (f_0)_1 = -K \cdot E_{acc}^2 \quad (3.53)$$

$K$  is defined as the Lorentz force detuning constant, while  $E_{acc}$  is the accelerating field,  $(f_0)_1$  the initial resonance frequency at  $E_{acc} = 0$ , and  $(f_0)_2$  the final resonance RF frequency at the steady-state field  $E_{acc}$ . The computed value of the Lorentz force detuning constant of the stiffened TESLA cavities is 1 Hz/(MV/m)<sup>2</sup>. Since this detuning is gradient-dependent and the cavity walls have an inertial mass, there is a transient behavior of the resonance frequency from the initial to the final state. The calculated Lorentz force detuning for a TESLA 9-cell cavity at 25 MV/m with an RF pulse length of 1300  $\mu$ s is -378 Hz due to the  $H$ -field only and -16 Hz due to the  $E$ -field only. Detailed measurements in the test stand of the TESLA Test facility have shown that the calculated and measured detunings are in agreement. To describe the dynamic effect of the detuning during an RF pulse, an approach based on a first-order differential equation is discussed.

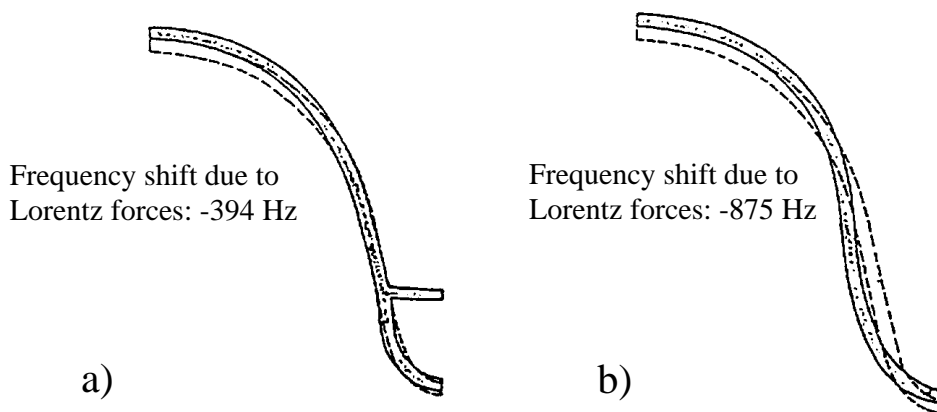


Figure 3.13: Cavity Cell Deformation of a TESLA cavity due to Lorentz force at a gradient of 25 MV/m. The wall thickness of niobium is 2.5 mm.

- a) Cavity cell with stiffening ring
- b) Cavity cell without stiffening ring

Dynamic measurements of Lorentz force acting on a superconducting MACSE cavity

have shown that the mechanical dynamics can be described by a first-order differential equation [Mos 93].

$$\begin{aligned}\tau_m \cdot \Delta\dot{\omega}(t) &= -(\Delta\omega(t) - \Delta\omega_T) - 2\pi K \cdot E_{acc}^2(t) \\ \Delta\omega(t) &= \omega_0(t) - \omega\end{aligned}$$

The equation describes the time variation of the frequency difference  $\Delta\omega$  between the resonance frequency  $\omega_0$  and the RF frequency  $\omega$  of the master oscillator which remains constant.  $\Delta\omega_T$  defines the frequency shift due to a mechanical frequency tuner. In these measurements on a MACSE cavity, the mechanical time constant  $\tau_m$  was determined to be in the order of 0.5 ms. For TESLA cavities, the time constant is expected to be in the order of 1 ms [Mos 94]. The description of Lorentz force detuning by a first-order differential equation implies a quasi instantaneous response of the detuning on the accelerating field. Unlike in second-order differential equations with inertia behavior, the resonance frequency changes immediately by  $\Delta\dot{\omega}(t)$  when the cavity field increases after turning on the RF power supply. Cavity filling to 25 MV/m in 500  $\mu$ s and constant field during the 800  $\mu$ s acceleration cycle results in a change of frequency of about 400 Hz. This is nearly twice the cavity bandwidth ( $Q_L = 3 \cdot 10^6$ ,  $f_{1/2} = 217$  Hz) and demands extra RF power (about 25 %) to maintain a constant gradient. Measurements on the dynamics of Lorentz force detuning have been carried out and will be presented in chapter 6.2.

# Chapter 4

## The Digital RF Control System for the TESLA Test Facility

In chapter 2, it has been shown that the cavity resonance frequency changes during an RF pulse due to Lorentz force detuning and from pulse to pulse due to microphonics. Amplitude and phase of the incident wave have to be controlled in order to maintain a constant accelerating field. The connection of amplitude and phase is described in Figure 4.1. Assuming that the resonator is initially excited on resonance (1), the change of the resonance frequency results in a lower amplitude (2) which is compensated by an increase of the input power (3). The simultaneous phase shift (2) is corrected by applying a phase shift to the driving signal in the opposite direction (3). In this chapter, the principle of sampling an RF signal is illustrated first. Then, the generation of the local oscillator frequency and timing signals is described and a detailed description of the individual components is given. This includes the Digital Signal Processor algorithm. Subsequently, diagnostic tools are introduced before the operational experience made in controlling the vector sum of eight cavities is discussed.

### 4.1 Principle and Components of the Digital Control System

The digital feedback used for TTF is based on the control of the real and imaginary components of the cavity field instead of on the traditional amplitude and phase control. Since it is impracticable to sample an RF field directly at frequencies above 100 MHz, it has to be converted to a lower frequency signal. For the TTF RF control system a sampling rate of 1 MHz has been chosen to guarantee a fast feedback system at reasonable costs. The intermediate frequency is 250 kHz. This choice is based on the principle of measuring real and imaginary parts of the down-converted cavity probe signal. The principle will be explained in the following. The down-conversion of a signal is shown in Figure 4.2. The frequency of the constant local oscillator (LO) signal (constant in amplitude and phase with respect to a master oscillator) is offset by 250 kHz from the operating frequency of

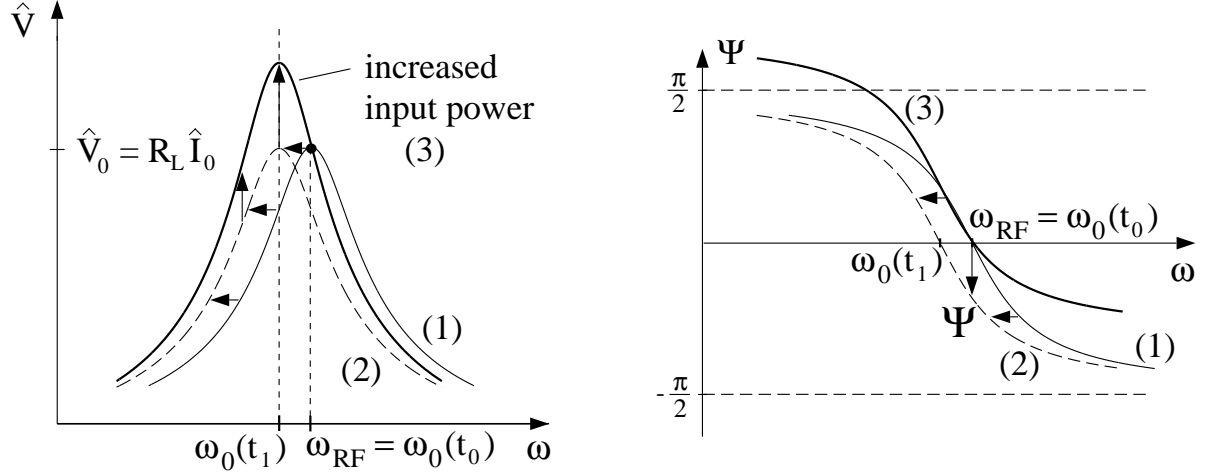


Figure 4.1: Principle of RF control. The change of the resonance frequency (left plot, curve (1) to curve (2)) results in a decreasing amplitude at the operating frequency  $\omega_{RF}$ . This is compensated by adjusting the input power (curve (3)). The resonance frequency variation yields also in a phase shift (right plot) corrected by applying a phase shift in the opposite direction.

the cavities in the TESLA Test Facility. The down-converted intermediate frequency (IF) signal of 250 kHz contains the information of amplitude and phase of the RF field.

An ideal RF mixer acts like a multiplier of two input signals. Assuming two sinusoidal signals

$$V_{RF}(t) = \hat{V}_{RF} \cdot \sin(\omega_{RF}t + \varphi_{RF}) , \quad V_{LO}(t) = \hat{V}_{LO} \cdot \sin(\omega_{LO}t + \varphi_{LO})$$

the intermediate output signal is

$$V_{IF}(t) = \frac{1}{2} \hat{V}_{RF} \hat{V}_{LO} \left( \cos \left( (\omega_{LO} - \omega_{RF})t + (\varphi_{LO} - \varphi_{RF}) \right) - \cos \left( (\omega_{LO} + \omega_{RF})t + (\varphi_{LO} + \varphi_{RF}) \right) \right)$$

A low pass filter removes the high frequency component of  $V_{IF}(t)$ . It remains a signal  $V(t)$  with a frequency which is the frequency difference of the input signals.

$$V_{IF}(t) \approx V(t) = \hat{V} \cos(\omega_{IF}t + \Delta\varphi) ;$$

with

$$\hat{V} = \frac{1}{2} \hat{V}_{RF} \hat{V}_{LO} ;$$

$$\omega_{IF} = \omega_{LO} - \omega_{RF} ;$$

$$\Delta\varphi = \varphi_{LO} - \varphi_{RF}$$

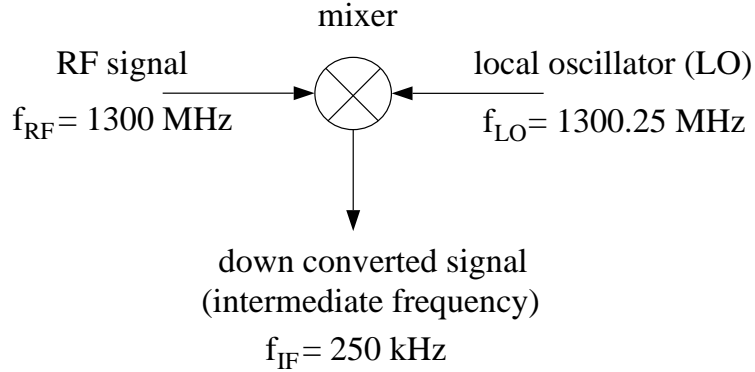


Figure 4.2: Principle of down-conversion of an RF signal to an intermediate frequency. The frequency of the constant local oscillator (LO) signal (constant in amplitude and phase with respect to a master oscillator) is offset by 250 kHz from the operating frequency of the cavities in the TESLA Test Facility. The down-converted intermediate frequency (IF) signal of 250 kHz contains the amplitude and phase information of the RF field.

If the amplitude and phase of the local oscillator signal are constant with respect to a master oscillator, the down-converted signal contains the information of amplitude and phase of the input RF signal. Sampling the 250 kHz intermediate frequency with a sampling rate of 1 MHz yields four samples per period (Figure 4.3). If the IF signal is

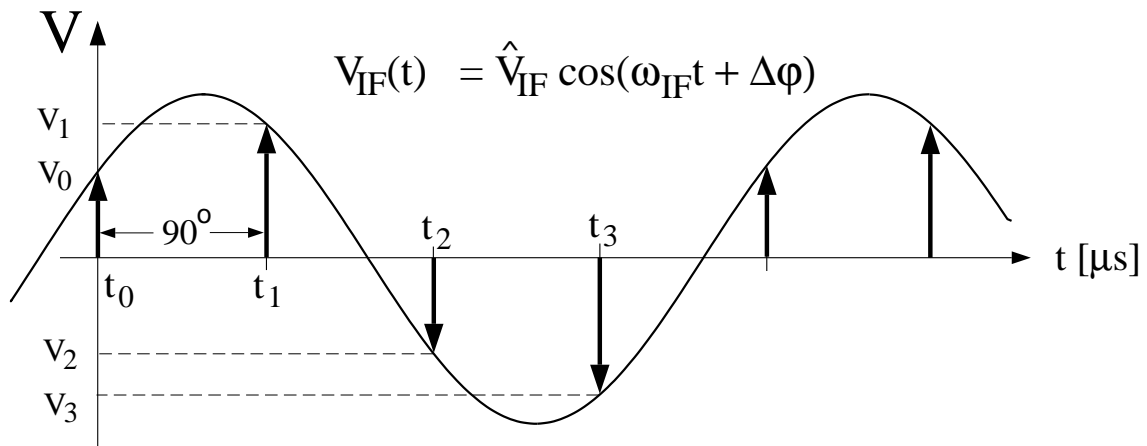


Figure 4.3: Sampling of the intermediate frequency with a sampling rate four times higher yields four samples in one cycle. Two consecutive samples represent a real and imaginary part of a corresponding complex field vector.

constant in amplitude and phase, samples are  $90^\circ$  appart (with  $1 \mu\text{s}$  time difference). Therefore, the previous sample can be referred to the time of the present one.

$$V(t_0) = \hat{V} \cos(\omega_{IF}t_0 + \Delta\varphi) = \hat{V} \cos(\omega_{IF}t_1 - \frac{\pi}{2} + \Delta\varphi) = \hat{V} \sin(\omega_{IF}t_1 + \Delta\varphi)$$

$$V(t_1) = \hat{V} \cos(\omega_{IF}t_1 + \Delta\varphi)$$

The two samples  $V(t_1)$  and  $V(t_0)$  are taken as the real and imaginary parts of the complex field vector<sup>1</sup>:

$$\mathbf{V}(t_1, t_0) = \begin{pmatrix} V_x(t_1) \\ V_y(t_1) \end{pmatrix} = \begin{pmatrix} V(t_1) \\ V(t_0) \end{pmatrix}$$

Since two adjacent samples in a 250 kHz cycle are phase shifted by  $90^\circ$ , the complex field vector receives a  $90^\circ$  rotation every microsecond (Figure 4.4). The different time steps

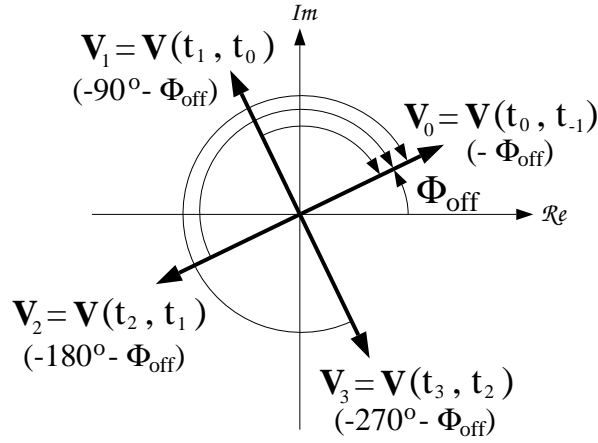


Figure 4.4: Two consecutive samples of the down-converted signal can be represented as a complex field vector  $\mathbf{V}(t_i, t_{i+1})$ . From one time step to the next, this vector is rotated by  $90^\circ$ . In order to compare the measured field vectors they have to be rotated by  $(-\Phi_{off})$ ,  $(-90 - \Phi_{off})$ ,  $(-180 - \Phi_{off})$ , and  $(-270 - \Phi_{off})$ , respectively. The phase offset  $\Phi_{off}$  compensates for the different cable length.

have an index  $k$  which indicates the sampling times  $t_k = k \cdot T_s$  where  $T_s$  is the sampling period. To detect amplitude and/or phase changes, one has to refer these consecutive vectors to a reference vector which is chosen to be the vector at  $t = t_0$ . Therefore, the measured complex field vector has to be rotated at every time step by  $90^\circ$ ,  $180^\circ$  or  $270^\circ$  respectively.

Figure 4.5 shows the schematic of the digital RF system for the TESLA Test Facility. First, an overview of the different components will be given.

<sup>1</sup>The real and imaginary parts sometimes called in-phase (I) and quadrature (Q) component

The incident RF wave coming from a master oscillator is controlled by a vector modulator. Amplitude and phase are set by real (*Re*) and imaginary (*Im*) part control signals. A circulator in the transmission line (waveguide) protects the klystron from power reflection which occurs during cavity filling and after turning off the RF or due to mismatched coupling. RF hybrids distribute the RF power evenly to individual cavities. Directional couplers and a three stub waveguide tuner are inserted in every waveguide path to measure forward and reflected power and to adjust the phase or the loaded  $Q_L$ , respectively. Each 9-cell cavity is equipped with a high power input coupler and a field probe antenna at the opposite side of the cavity. Eight cavities are assembled in one cryomodule. Mechanical frequency tuners are mounted at every cavity to adjust the cavity resonance frequency to an optimum predetuning. All field probe signals are split up in three ways. The first signal is used for feedback. It is down-converted to the 250 kHz intermediate frequency and sampled with a high-resolution fast ADC which transmits the data to a digital signal processor (DSP). The second is the input signal of a so-called transient detection board which detects the beam-induced transients on the amplitude of the cavity fields. This signal is used to perform a beam-based vector sum calibration (see section 4.4). The third field probe signal is also down-converted to 250 kHz, but sampled by an ADC (12-bit) of lower resolution than used for feedback. This ADC belongs to a set of monitoring ADCs which sample also the forward and reflected waves of each cavity. One digital signal processor receives the digitized field vector sum. The control system for 16 cavities requires four DSPs. All of them transmit their data to a final DSP which determines the complete vector sum and applies to it the control algorithm. The new settings for the vector modulator are converted to analog signals by two DACs. All the DSPs and monitoring ADC boards are located in an Euro-crate with VME-bus interface. Data and parameter settings are accessible via an embedded micro-computer (SUN) which is part of the main control system of the linac. A detailed description of the system will be given in the next section.

## 4.2 Local Oscillator and Timing

Sampling the down-converted 250 kHz four times per cycle requires a 1 MHz clock which is synchronized to the RF and to the local oscillator (LO) frequency. All frequencies are derived and phase locked to a master frequency. For the TESLA Test Facility, the reference has been chosen as  $f_{ref} = 9.027775$  MHz. There are several derived frequencies as shown in Figure 4.6. The RF operating frequency 1299.9996 MHz which is usually designated as 1.3 GHz is generated from  $f_{ref}$  by multiplication with 144. A clock frequency  $f_c$  is derived from the reference by  $f_c = \frac{10}{9}f_{ref} = 10.030861$  MHz. This frequency is distributed along the linac. A timing module in the low level RF system generates the sampling frequency by a countdown clock  $f_s = \frac{1}{10}f_c$ . In principle, the RF diagnostic frequency

(local oscillator), which is approximately 250 kHz<sup>2</sup> above the RF operating frequency, can also be synthesized by  $f_{LO} = (144 + \frac{1}{36})f_{ref}$ . Usually this is achieved by phase-locking a second oscillator to the master oscillator on the 10 MHz level. Down-conversion of the RF operating frequency with this LO-frequency leads to the 250 kHz intermediate frequency as mentioned in section 4.1. In the TESLA Test Facility, a different method for LO generation has been chosen. For the detection of real and imaginary components, it is important to have a 90° shift between two consecutive samples. This can also be achieved by shifting the local oscillator phase by 90° every microsecond. The down-converted signal is then a 250 kHz step function (see Figure 4.7). The phase shift is performed by a table-driven DAC board, called I/Q-driver. It consists of a universal programmable two-channel function generator. The input frequency is the operating frequency  $f_{RF}$  of the master oscillator. The real and imaginary control signals are generated by two 16 bit DACs receiving the digital input from two 32k RAM blocks. They contain data tables for real and imaginary components which can be adjusted by the operator. The DACs are clocked by a 1 MHz frequency signal derived from the clock frequency  $f_c$ . The periodic step function is delayed with respect to the sampling time to assure that the sampling occurs on the plateau of the step and not at the time when the 90° shift is performed. The reasons underlying the decision to generate the local oscillator signal in this way are as follows: Firstly, this method is insensitive to time jitter of the clock signal. Secondly, the measured phase between two consecutive samples is always well defined after turning on the master oscillator, while in the case of a second oscillator being locked to the reference frequency one has to ensure the correct phase relation between them in order to prevent 90° phase jumps after powering up. Finally, it provides an enormous flexibility of the digital system. Changes of the sampling frequency and thus the LO frequency are achieved by software by means of setting new tables. It is also possible to reduce the harmonic components of the 250 kHz step signal by introducing smaller phase shifts at a higher rate (up to 10 MHz) to get a better approximation of a sinusoidal signal.

## 4.3 Digital Signal Processing

### 4.3.1 Hardware

#### DSP System

The sampling rate of 1 MHz demands a high processing speed and a large input/output (I/O) capability in order to handle the high data rate. The DSP C40 (floating-point parallel digital signal processor TMS320C40 made by Texas Instruments) with 32-bit address and data busses represents the best choice at the present time. It provides six processor-to-processor communication interfaces, the so-called communication ports. The

---

<sup>2</sup>The exact frequency of the RF diagnostic frequency is a quarter of the sampling frequency  $f_s$  and is calculated to 250.7715 kHz

DSP is mounted on a module following the TIM-40<sup>3</sup> standard. The carrier board DBV44 from Loughborough Sound Images is a VME slave board with a modular architecture. Each DBV44 board can accommodate up to four modules. Three communication ports of each site are routed to front panel connectors and the rest are on-board links. The module type which is used for the TESLA Test Facility is the single module MDC40S2-40 with 40 MHz clock rate. The data transfer of the 32-bit words between the three DSPs is performed through the on-board communication port links on a byte-to-byte basis at a maximum rate of 20 Mbps. Data transmission is asynchronous due to FIFO (first-in-first-out) I/O buffers. The schematic of the DSP board connected to ADC and DAC boards is shown in Figure 4.8.

---

<sup>3</sup>Texas Instruments' TMS320C4x Module Specification

# TTF RF scheme

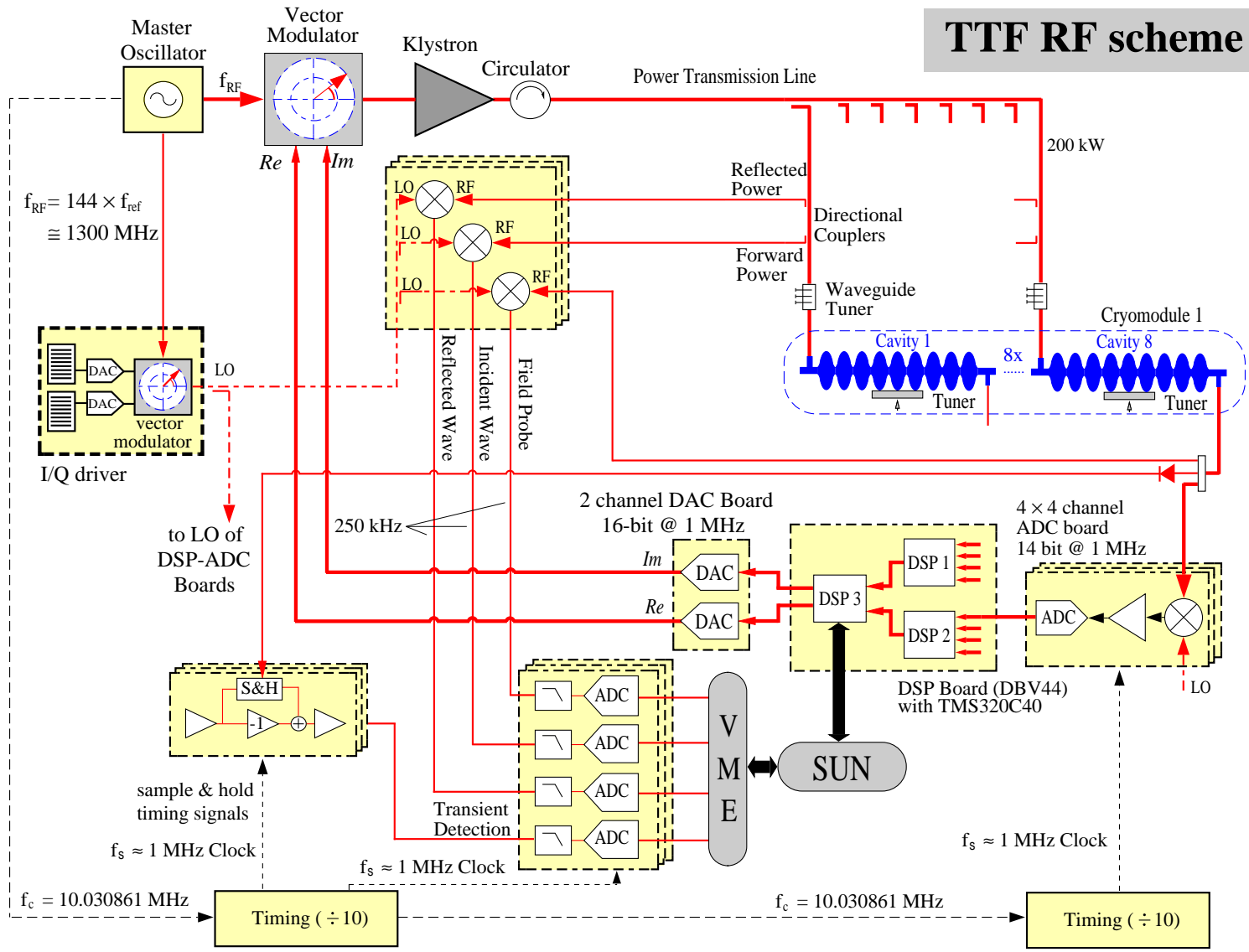


Figure 4.5: TTF RF control scheme for 8 cavities per klystron. A detailed description is given in the text.

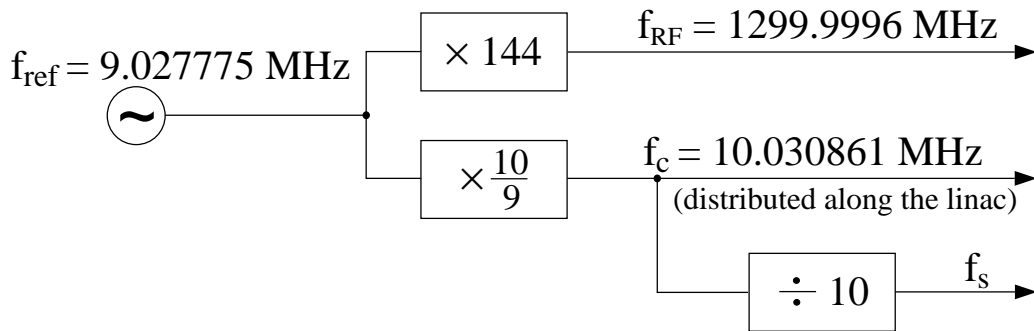


Figure 4.6: TTF RF scheme for RF frequency generation and timing signals

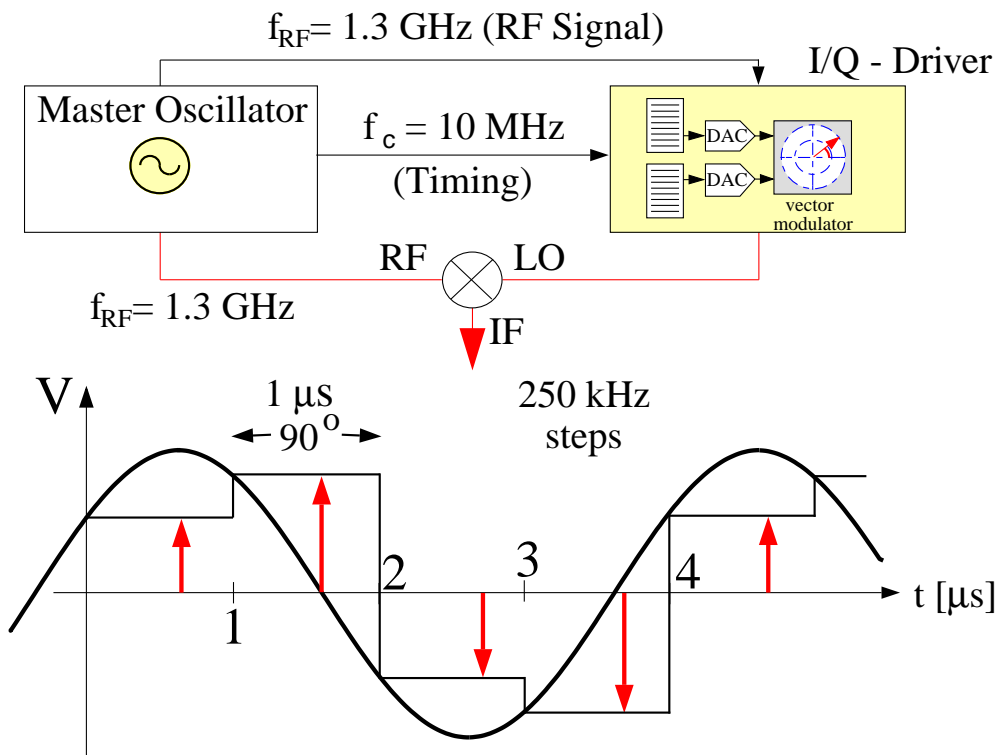


Figure 4.7: Local oscillator frequency generation with I/Q-driver.  
 Figure above: A two channel functional generator drives a vector modulator which switches the LO phase in  $90^\circ$  increments.  
 Figure below: The down-converted signal of an RF mixer is a 250 kHz step signal which is sampled with a frequency of 1 MHz. The sampling time is indicated by arrows.

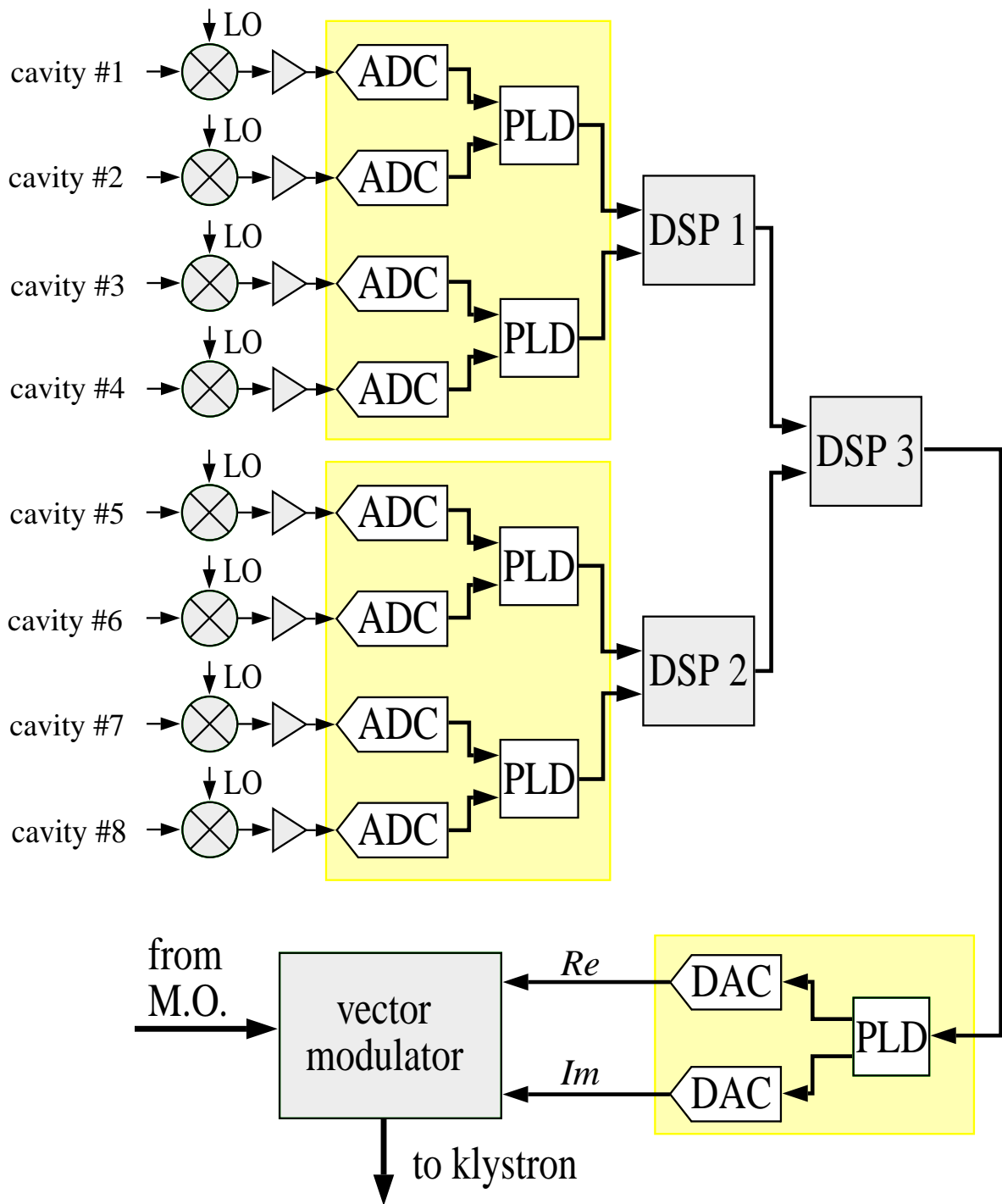


Figure 4.8: Digital signal processing hardware

## ADC and DAC Boards

The ADC and DAC boards are in-house developed boards designed as 6U (six units) Eurocards. Both of them have interfaces to the standard communication ports of Texas Instruments DSPs with handshake protocols.

The ADC board consists of four independent ADC channels with 14-bit A/D converters (Datel ADS 929, maximum sampling rate 2 MHz) operated at 1 MHz sampling frequency. Input amplifiers with a gain of 30 and a bandwidth of 9 MHz amplify the signal to the maximum sampling range of  $\pm 5$  V to get highest resolution. Two ADCs transmit their data to a programmable logic device (PLD). The PLD is connected with the DSP through the communication port interface. The data of two ADC channels is pipelined to one communication port of the DSP. Therefore, a total of six ADC channels can be connected to one DSP (3 front panel connectors). To save conversion time from integer (ADC) to floating point (DSP) format, this conversion is already performed in the PLD. The total delay time between ADC input and DSP input is approximately 900 ns.

The DAC board is a two-channel board with 16-bit D/A converters (AD768). Similar to the ADC board, it has a programmable logic device which is connected to the DSP through the standard communication port. The floating point data from the DSP is converted to integer format for the DAC. Because of the external conversion, valuable computing time is saved once more in the DSP. Additionally, the PLD logic checks the incoming data and limits it to the valid input range for the DAC. The delay time through the DAC board is about 500 ns.

The choice of 14-bit A/D and 16-bit D/A converters was made on the basis of requirements, safety margins and cost considerations. For example, correlated amplitude errors have to be suppressed to a value better than  $3 \cdot 10^{-4}$  and correlated phase errors to better than  $0.1^\circ$  (chapter 2.2.1) demanding an approximately 10 times better resolution in the measurement ( $\rightarrow$  14-bit necessary).

## RF Mixer

RF signals can be converted to low frequency signals with RF mixers and Schottky diodes. With the latter, only the amplitude of the RF signal can be measured. To determine both amplitude and phase RF mixers are used. In the TTF, high precision is required for the detection of real and imaginary components. Down-conversion to a 250 kHz sinusoidal signal or to a step function results in harmonic components of the 250 kHz base frequency. Tests with two different mixers have been performed to improve the linearity of the down-converted signal. For  $10^{-3}$  linearity we need -60 dBc for harmonics. The comparison of the low-level mixer ZFM 2000 (Mini Circuits; with +7 dBm at the LO input) and the high-level mixer RAY11 (Mini Circuits; with +23 dBm at the LO input) is shown in Figure 4.9. For example, at 0 dBm RF input power the first harmonic at 500 kHz is only suppressed by -19 dB with the ZFM 2000 while the suppression is about -58 dB with the

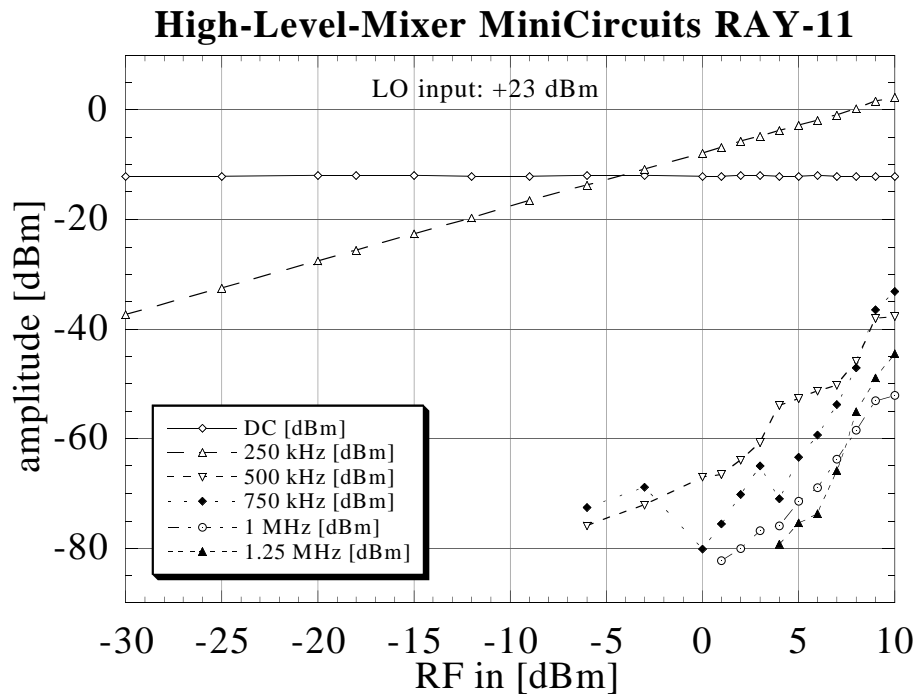
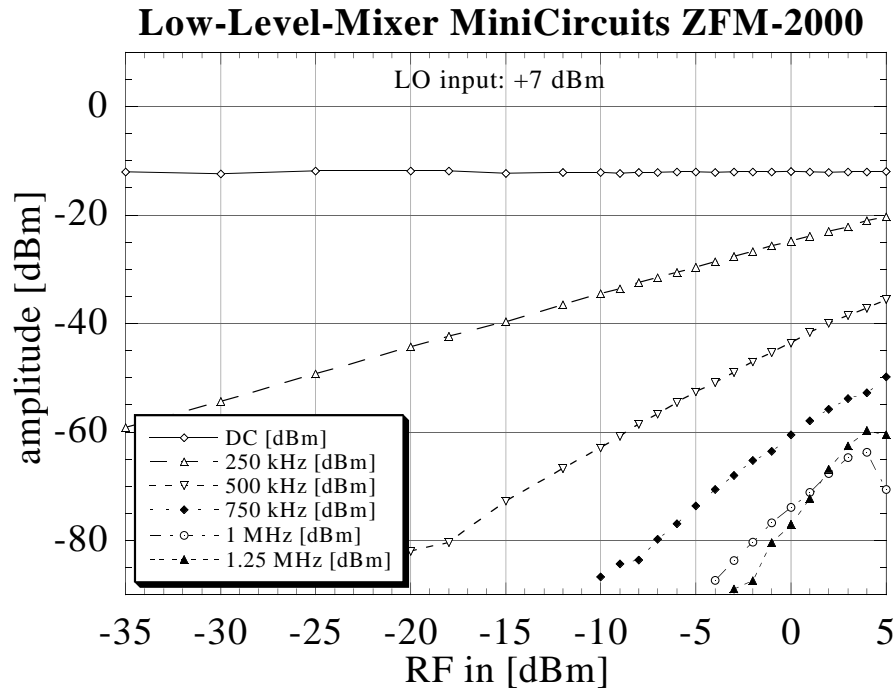


Figure 4.9: Low-level RF mixer ZFM 2000 and high-level mixer RAY11. The RF output power is plotted versus the RF input power for the 250 kHz base frequency and some of its harmonics.

high-level mixer RAY11. Based on these measurements, the high-level mixer RAY11 has been chosen despite the fact that large LO power is needed to supply all the mixers for the cavity field probe, incident wave and reflected wave signals.

### 4.3.2 Digital Signal Processor Code

The TTF control algorithm for 8 cavities has been implemented on the TMS320C40 parallel processor system and is distributed over 3 DSPs. The C40 internal communication ports are used to send signals between this group of processors. DSPs 1 and 2 read cavity data from the ADC with a sampling period of 1  $\mu$ s, perform the multiplication of the individual complex vectors (*Re/Im*) with the rotation matrices, and calculate the vector sum for 4 cavities. The complex field vector of cavity  $j$  consists of the present and the previous sampled signal as shown in section 4.1.

$$\mathbf{V}_j(t_k) = \begin{pmatrix} V_{xj}(t_k) \\ V_{yj}(t_k) \end{pmatrix} = \begin{pmatrix} V_j(t_k) \\ V_j(t_{k-1}) \end{pmatrix}$$

Beside the 90° phase shifts, every measured vector is rotated and scaled to compensate phase differences (offset  $(\Phi_{off})_j$  for cavity  $j$ ) due to different cable lengths and to calibrate the accelerating fields in the different cavities (scaling factor  $g_j$  for cavity  $j$ ). Consequently, the input vector for four consecutive time steps has to be multiplied by different matrices.

$$\begin{aligned} t_k & : \mathbf{M}_j(t_k) &= \begin{pmatrix} a_j & -b_j \\ b_j & a_j \end{pmatrix} \\ t_{k+1} \quad (-90^\circ) & : \mathbf{M}_j(t_{k+1}) &= \begin{pmatrix} 0 & 1 \\ -1 & 0 \end{pmatrix} \cdot \begin{pmatrix} a_j & -b_j \\ b_j & a_j \end{pmatrix} = \begin{pmatrix} b_j & a_j \\ -a_j & b_j \end{pmatrix} \\ t_{k+2} \quad (-180^\circ) & : \mathbf{M}_j(t_{k+2}) &= \begin{pmatrix} -1 & 0 \\ 0 & -1 \end{pmatrix} \cdot \begin{pmatrix} a_j & -b_j \\ b_j & a_j \end{pmatrix} = \begin{pmatrix} -a_j & b_j \\ -b_j & -a_j \end{pmatrix} \\ t_{k+3} \quad (-270^\circ) & : \mathbf{M}_j(t_{k+3}) &= \begin{pmatrix} 0 & -1 \\ 1 & 0 \end{pmatrix} \cdot \begin{pmatrix} a_j & -b_j \\ b_j & a_j \end{pmatrix} = \begin{pmatrix} -b_j & -a_j \\ a_j & -b_j \end{pmatrix} \end{aligned}$$

where the quantities  $a_j$  and  $b_j$  denote

$$a_j = g_j \cdot \cos(\Phi_{off})_j \quad ; \quad b_j = g_j \cdot \sin(\Phi_{off})_j .$$

The partial vector sum at every time step is calculated to

$$\mathbf{V}(t_k) = \begin{pmatrix} V_x(t_k) \\ V_y(t_k) \end{pmatrix} = \sum_{j=1}^4 \mathbf{M}_j(t_k) \cdot \mathbf{V}_j(t_k) .$$

All calculations must be carried out within the sampling period of one microsecond. The elaborate computation of the partial vector sum requires 16 multiplications and 14 additions. This is possible since a 40 MHz DSP executes 20-40 instructions per microsecond in parallel processing. For example, multiplication and summation can be performed simultaneously in a single 50 ns cycle. Furthermore, partial calculations performed at a time step  $t_k$  can be used in the following time step  $t_{k+1}$ . The rotation of the incoming four cavity samples and their vector sum is written as:

$$\begin{aligned}
t_k : \quad \begin{pmatrix} V_x(t_k) \\ V_y(t_k) \end{pmatrix} &= \sum_{j=1}^4 \begin{pmatrix} a_j & -b_j \\ b_j & a_j \end{pmatrix} \cdot \begin{pmatrix} V_j(t_k) \\ V_j(t_{k-1}) \end{pmatrix} \\
&= \sum_{j=1}^4 \begin{pmatrix} a_j V_j(t_k) - b_j V_j(t_{k-1}) \\ b_j V_j(t_k) + a_j V_j(t_{k-1}) \end{pmatrix} \\
t_{k+1} : \quad \begin{pmatrix} V_x(t_{k+1}) \\ V_y(t_{k+1}) \end{pmatrix} &= \sum_{j=1}^4 \begin{pmatrix} b_j & a_j \\ -a_j & b_j \end{pmatrix} \cdot \begin{pmatrix} V_j(t_{k+1}) \\ V_j(t_k) \end{pmatrix} \\
&= \sum_{j=1}^4 \begin{pmatrix} b_j V_j(t_{k+1}) + a_j V_j(t_k) \\ -a_j V_j(t_{k+1}) + b_j V_j(t_k) \end{pmatrix} \\
t_{k+2} : \quad \begin{pmatrix} V_x(t_{k+2}) \\ V_y(t_{k+2}) \end{pmatrix} &= \sum_{j=1}^4 \begin{pmatrix} -a_j & b_j \\ -b_j & -a_j \end{pmatrix} \cdot \begin{pmatrix} V_j(t_{k+2}) \\ V_j(t_{k+1}) \end{pmatrix} \\
&= \sum_{j=1}^4 \begin{pmatrix} -a_j V_j(t_{k+2}) + b_j V_j(t_{k+1}) \\ -b_j V_j(t_{k+2}) - a_j V_j(t_{k+1}) \end{pmatrix} \\
t_{k+3} : \quad \begin{pmatrix} V_x(t_{k+3}) \\ V_y(t_{k+3}) \end{pmatrix} &= \sum_{j=1}^4 \begin{pmatrix} -b_j & -a_j \\ a_j & b_j \end{pmatrix} \cdot \begin{pmatrix} V_j(t_{k+3}) \\ V_j(t_{k+2}) \end{pmatrix} \\
&= \sum_{j=1}^4 \begin{pmatrix} -b_j V_j(t_{k+3}) - a_j V_j(t_{k+2}) \\ a_j V_j(t_{k+3}) + b_j V_j(t_{k+2}) \end{pmatrix}
\end{aligned}$$

The second part of each vector is already calculated one microsecond beforehand and then stored in the memory. Handling the data in this way allows the rotation and calculation of the vector sum of four cavity vectors in 18 cycles with 20 cycles being the maximum of a 40 MHz DSP. Moreover, careful memory allocation for data and parameters is necessary to prevent internal bus conflicts.

A more extensive set of computations is carried out in the DSP 3, which receives partial vector sums from two DSPs, calculates the vector sum of all 8 cavities and executes the feedback algorithm. The present feedback algorithm applies proportional gain to the error signal and uses a digital low-pass filter to reduce the sensor noise. The low pass filter is expressed by

$$\bar{\mathbf{V}}(t_{k+1}) = \left(1 - \frac{1}{N}\right) \cdot \bar{\mathbf{V}}(t_k) + \frac{1}{N} \cdot \mathbf{V}(t_k)$$

$$\begin{pmatrix} \bar{V}_x(t_{k+1}) \\ \bar{V}_y(t_{k+1}) \end{pmatrix} = \left(1 - \frac{1}{N}\right) \cdot \begin{pmatrix} \bar{V}_x(t_k) \\ \bar{V}_y(t_k) \end{pmatrix} + \frac{1}{N} \cdot \begin{pmatrix} V_x(t_k) \\ V_y(t_k) \end{pmatrix}. \quad (4.1)$$

The variable  $N$  is defined as the filter parameter. Setting  $N = 1$  is equivalent to the absence of filtering. Increasing  $N$  means a reduced contribution of the present measured value to the next mean value. The proportional gain feedback is applied to the calculated mean vector at time  $t = t_k$ .

$$\begin{pmatrix} V_{ctrl,x}(t_k) \\ V_{ctrl,y}(t_k) \end{pmatrix} = \begin{pmatrix} K_x & 0 \\ 0 & K_y \end{pmatrix} \cdot \begin{pmatrix} V_{set,x}(t_k) - \bar{V}_x(t_k) \\ V_{set,y}(t_k) - \bar{V}_y(t_k) \end{pmatrix} + \begin{pmatrix} V_{FF,x}(t_k) \\ V_{FF,y}(t_k) \end{pmatrix}$$

Individual gains ( $K_x, K_y$ ) and setpoints ( $V_{set,x}, V_{set,y}$ ) for the real and imaginary component control signal are set every microsecond. Additionally, feed forward ( $V_{FF,x}, V_{FF,y}$ ) is added at every time step. Feed forward is a control signal which is independent of the measured error signal. In this way, repetitive errors in the RF system like Lorentz force detuning of the cavities or deviation from the flattop of the high-voltage modulator pulse can be compensated in advance by proper actuator settings. Hence, this method reduces periodic perturbations within a pulse. The feedback controller has to suppress only the remaining stochastic fluctuations like microphonics or slowly varying beam parameters. The adaptive feed forward control system is a stand-alone program running in parallel to the RF control system. It identifies the step response of the RF system, measures the error signal during an RF pulse continuously and calculates the required actuator settings averaged over time. A detailed description of this system is given in [Lie 98]. For maximum flexibility all parameters (gain, setpoint and feed forward) are updated from tables. The table size is based on the TESLA/TTF RF pulse structure and adjusted to 2048 values which correspond to a new setting every microsecond. Finally, the control signals are sent to the DACs. A diagram of the feedback algorithm is shown in Figure 4.10. The interrupt service routines are implemented in all DSPs to read data from the communication ports, thus allowing modification of the rotation matrices between pulses, correction of DC offsets for the feed forward table and variation of the pulse length. As time is critical, all programs have been developed in C4x assembly language to increase calculation speed. The internal DSP timer has been used in all DSPs to scale and rotate matrices in case of failure of the TTF timing system. The computational delay including ADC and DAC conversion is  $4.2 \mu\text{s}$ .

## 4.4 Diagnostic Tools

### 4.4.1 Detuning Measurement

The digitized field-probe signals of the cavities provide the basis for extensive diagnostics. The real and imaginary components of the individual cavity fields can be accessed by reading the data directly from the DSP memory or from the monitoring ADCs. In both cases the information of the amplitude and phase can be reconstructed. The phase is

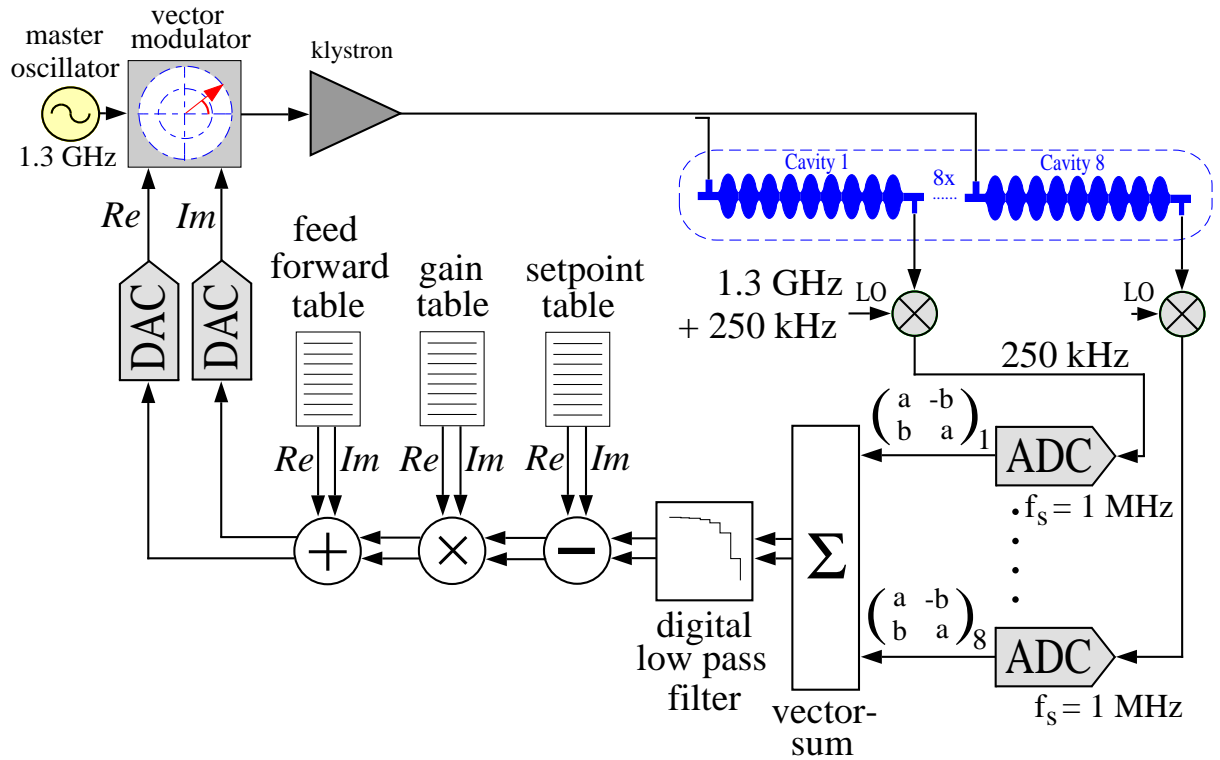


Figure 4.10: Schematic view of the feedback algorithm. Each table consists of individual parameter settings for real ( $Re$ ) and imaginary ( $Im$ ) components for a time period of  $2048 \mu s$ .

referred to the fixed local oscillator frequency. The RF control system has to maintain a constant phase during the  $800 \mu s$  beam acceleration period. Due to microphonics and Lorentz force detuning, the resonance frequency of the cavity varies from pulse to pulse and within each pulse but the master oscillator frequency is kept constant. However, after turning off the RF power, the stored electromagnetic field in the cavity immediately oscillates at the resonance frequency  $\omega_0$  of the cavity. The corresponding frequency jump results in a linear phase variation with time (see Figure 4.11) as long as the resonance frequency remains constant. This effect is used to determine the resonance frequency of all cavities by fitting the phase curves with a straight line. The resulting frequency is the difference frequency with respect to the RF frequency of the reference generator..

#### 4.4.2 Vector Sum Calibration

It has been shown in chapter 2.1.3 that microphonics in combination with gradient and phase calibration errors leads to an energy spread even if the measured vector sum is

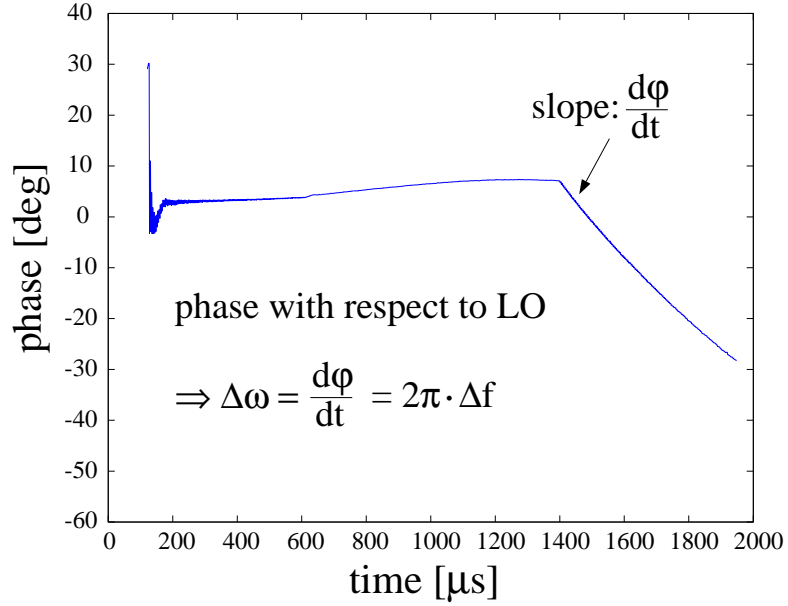


Figure 4.11: Measurement of the detuning

kept constant by the RF control system. The influence of phase calibration errors is stronger than that of gradient calibration errors. If the energy spread contribution must not exceed  $2 \cdot 10^{-4}$  when controlling 16 cavities, accuracies of  $\pm 10\%$  for gradient and of  $\pm 1.5^\circ$  for phase calibration are required. Beside that, closing the feedback loop for the vector sum regulation demands a proper summation of the individual cavity vectors. A rough adjustment of  $\pm 4^\circ$  of the individually measured cavity phases can be achieved by pulsing the cavity with constant forward power and fitting the phase response. Later, a more precise calibration is made using beam-induced transients.

On account of different cable lengths and different attenuations, the measured cavity field vectors have to be rotated and scaled before being added. Phases are determined by pulsing the cavity with constant forward power. In that case, the control signal consists only of the real part at the vector modulator. In chapter 3.3.3 it has been shown that the transient behavior of a cavity results in a spiral curve of the field vector as a function of detuning. The initial increase is along the real axis, independent of detuning. The polar plots of the measured individual cavity fields show the field increase in an arbitrary direction (see Figure 4.12a). By fitting the cavity field curve in the polar plane the phase offset  $(\Phi_{off})_j$  is determined and the corresponding rotation matrix is calculated. This procedure leads to the correct loop phase of the vector sum. The incident RF wave can have different phases  $(\Delta\Phi_{inc})_j$  due to different wave guide lengths to the cavities  $i$ . This can only be measured with beam. Beam acceleration leads to a transient on the acceleration voltage. In the ideal case, in which the phases of all incident waves to the

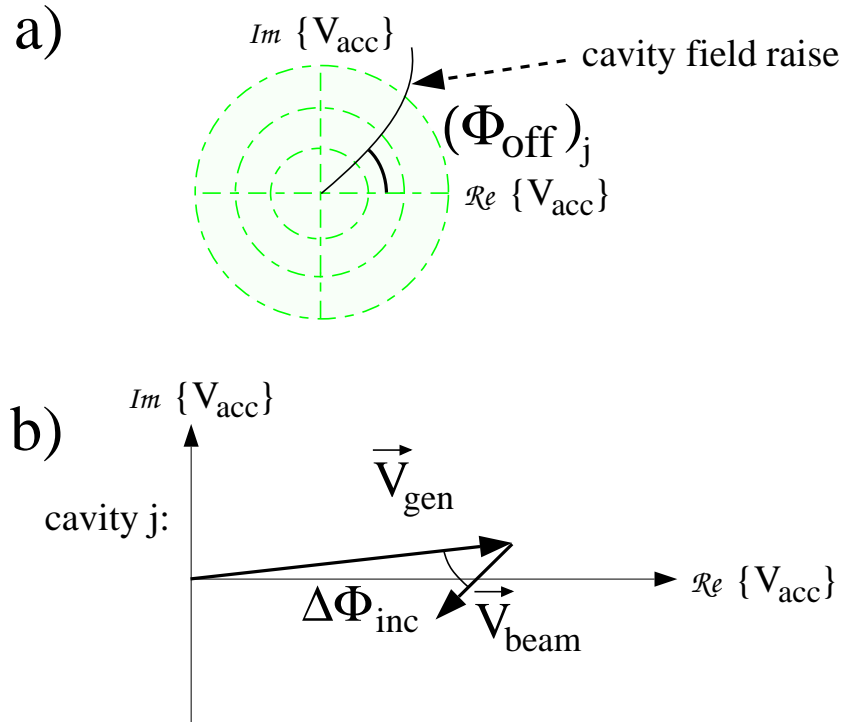


Figure 4.12: a) Measurement of the phase offset of the individual cavities by pulsing with constant forward power.  
b) The beam transient induces a voltage. In the ideal case (beam phase  $0^\circ$ , on-crest operation) the beam-induced voltage is opposite the generator-induced voltage. Different phases of the incident waves leads to different phases  $(\Delta\Phi_{inc})_j$  for cavity  $j$ .

cavities are equal, the beam can be accelerated on-crest (beam phase  $0^\circ$ ). In this case,, all beam transients are opposite to the generator (klystron)-induced acceleration voltage. If the incident waves have different phases, a phase angle between the two voltages is introduced (see Figure 4.12b). To determine this phase angle, a special board has been developed to observe the beam-induced transients (see *transient detection board* in Figure 4.5). A correction of the incident wave can be achieved by using three stub wave guide tuners with which the incident wave can be shifted by  $\pm 30^\circ$  [Hün 98]. Besides the phase information from the transient detection board, the drop of the accelerating voltage due to the beam-induced transients is used for gradient calibration. The bunched nature of the beam results in a sawtooth-like profile on the gradient. With the TTF photo-gun injector (injector II) a single bunch with a total charge of 8 nC induces a transient of  $1.36 \cdot 10^{-3}$  of 25 MV/m in cavities with  $Q_L = 3 \cdot 10^6$ . By measuring the beam current and

the amplitude of the transients, the gradients in the cavities are calibrated in reference to the beam-induced voltages thus providing the individual scaling factors  $g_j$  in the rotation matrices [Lie 98]. The transient detection board acts like an amplifier for the signal structure imposed on the gradient in the flattop range. The principle is shown in Figure 4.13.

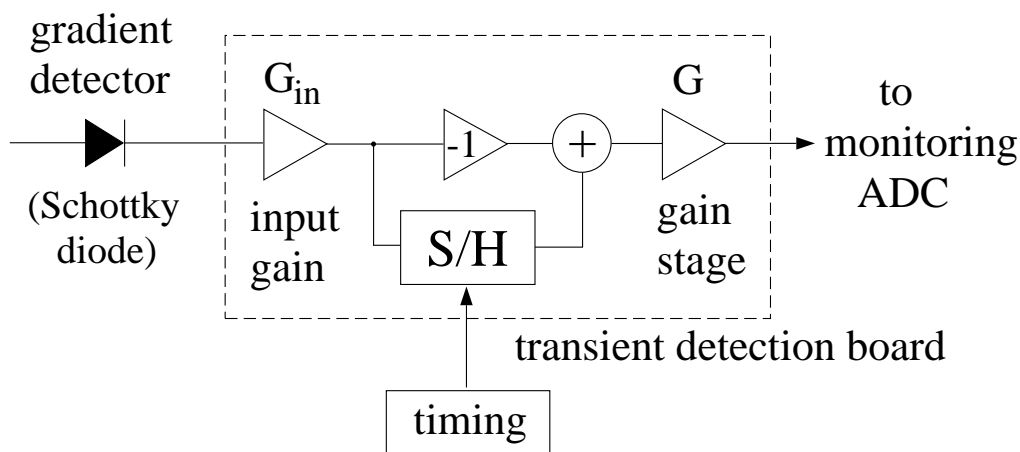


Figure 4.13: Principle of the transient detection board. The cavity field amplitude is measured with a Schottky diode. A sample and hold stage guarantees the subtraction of the offset of the gradient detector voltage just before the beam pulse arrives. The difference signal is amplified with a gain of up to 100 before sampling it with a monitoring ADC.

On this board a Schottky diode is used to measure the amplitude of the cavity fields. Amplifying the transient calls for a subtraction of the gradient detector voltage just before the beam pulse arrives. The timing system provides the required sample and hold signals (S/H). The detected transients are amplified by a gain of up to 100 to the maximum range of  $\pm 5$  V of the ADC to get highest resolution. The achieved accuracy in phase calibration during the first run of the TESLA Test Facility was  $0.5^\circ \pm 0.1^\circ$  [Lie 98].

## 4.5 Operational Experience

Cryomodule 1 with eight 9-cell cavities was operated in different modes. Due to a failure of one mechanical frequency tuner only seven cavities were tuned to the operating frequency. The resonance frequency of the eighth cavity was 110 kHz offset from the RF frequency of 1.3 GHz. The scaling factor for this cavity has been set to zero in the digital signal processor in order to obtain the vector sum from the remaining seven cavities. In the following, the vector sum refers to these seven cavities.

### 4.5.1 Open Loop Operation

First, operation of the module has started without feedback and without beam. Constant power has been applied during the filling of the cavities ( $500 \mu\text{s}$ ) and has then been reduced to a quarter to result in nearly steady-state condition. The RF has been turned off after  $1300 \mu\text{s}$ . The  $800 \mu\text{s}$  time span between filling and turning off the RF power is called *flattop*. The individual gradients and phases of the cavities are plotted versus time in the upper part of Figure 4.14. The two lower plots show the amplitude (in MV) and

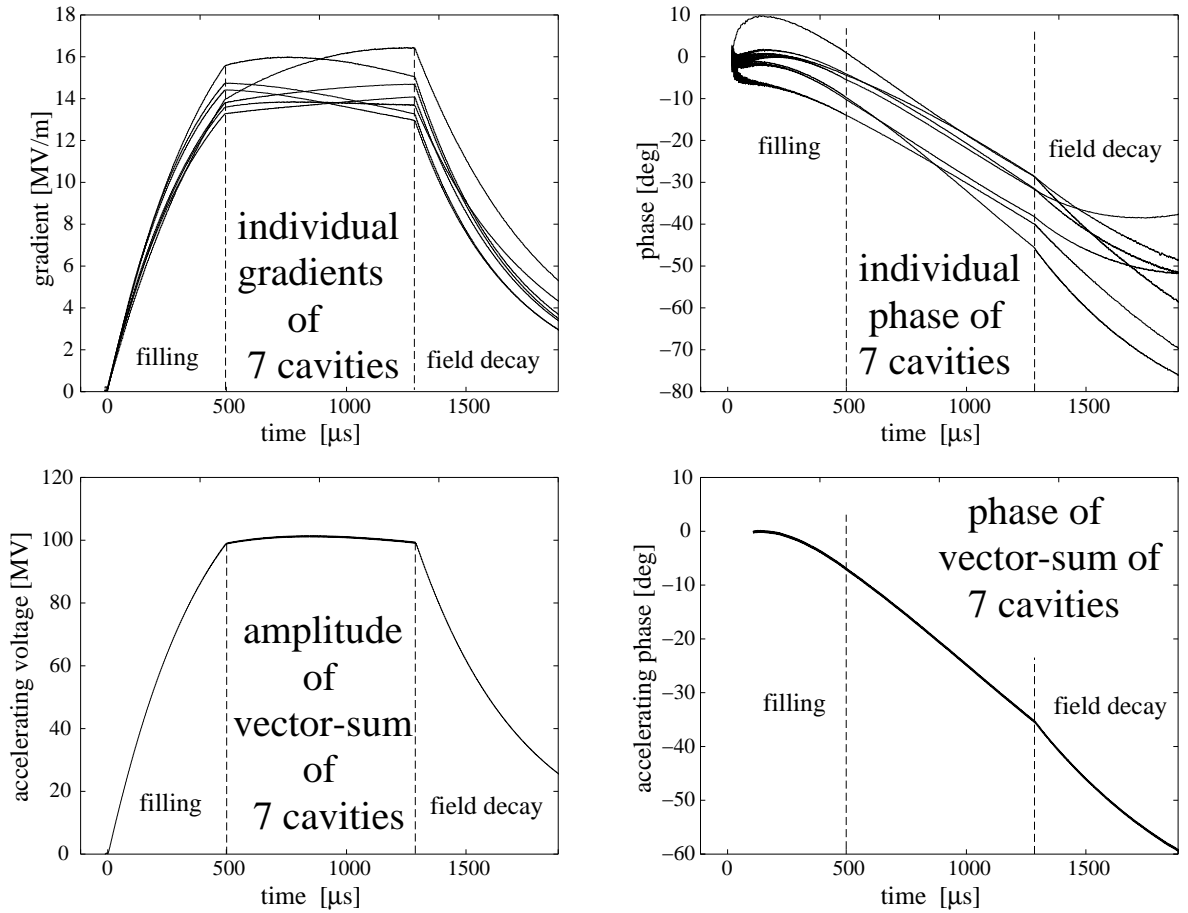


Figure 4.14: Open loop operation of cryomodule 1 with seven cavities tuned on resonance. The upper two plots show the gradients and phases of the individual cavities versus time. The lower two plots display the corresponding accelerating voltage and phase of the vector sum.

phase (in degree) of the vector sum. The cavities have been tuned in such a way so as to be on resonance at the beginning of the RF pulse. Lorentz force detuning results in a monotonous phase shift of nearly  $30^\circ$  during the flattop. With proper predetuning it

can be reduced to approximately  $20^\circ$  [Mos 94]. For gradients of 25 MV/m, the optimum predetuning of a design cavity (with design parameters  $K$  and  $\tau_m$ ) is about 230 Hz, which means that the resonance frequency of the cavity is 230 Hz above the RF frequency  $f_{RF}$ . Due to Lorentz forces, the resonance frequency is shifted towards lower frequencies, passes the RF frequency in the middle of flattop and reaches a frequency approximately 200 Hz below the operating frequency  $f_{RF}$  at the end of the RF pulse. The phase of the cavity increases as long as  $f_0$  is above  $f_{RF}$  and finally decreases ( $f_0 < f_{RF}$ ) ending up with the  $20^\circ$  phase variation in total. The precise calibration of the individual phases is with respect to the beam. However, during this operation no beam was injected. Therefore, the phases in Figure 4.14 are only relative to the master oscillator. The slopes on the individual gradients come from the slightly different loaded  $Q_L$  which varied from  $1.62 \cdot 10^6$  to  $2.21 \cdot 10^6$ . The pulse-to-pulse stability without any feedback was in the range of  $5 \cdot 10^{-4}$ . The repetitive errors were dominating providing large potential for adaptive feed forward.

### 4.5.2 Closed Loop Operation without Beam Acceleration

Before closing the feedback loop, the loop phase has to be adjusted to ensure negative feedback. Amplitude and phase of the vector sum have been regulated as real and imaginary components with a feedback gain of approximately 30 for each one of them. No feed forward has been applied. Parameters such as filling time and beam acceleration time (flattop) have been kept constant. The total accelerating voltage over the module has been set to 115 MV. The plots in Figure 4.15 display the gradients and phases of the individual cavities as well as the magnitude and phase of the vector sum. The rms errors during the 800  $\mu s$  flattop are

$$\left(\frac{\sigma_V}{V}\right)_{rms} = 0.2\% ; \quad (\sigma_\varphi)_{rms} = 0.25^\circ$$

One can see that several cavities powered by one klystron and controlled by a single control loop behave basically like a single cavity. If all individual cavities have the same loaded quality factor  $Q_L$ 's, the decay of the field after turning off the RF follows an exponential curve ( $\sum_i^N \exp(-t/\tau_i) = N \cdot \exp(-t/\tau)$  with  $\tau = \tau_1 = \tau_2 \dots$ ). The  $Q_L$ -values in the first cryomodule in the TESLA Test Facility were slightly different (see above). However, the resulting decay differs only within  $4 \cdot 10^{-3}$  from an exponential curve with a mean loaded  $Q_L$  of  $(1.80 \pm 0.04) \cdot 10^6$ . This has been verified several times during operation.

### 4.5.3 Closed Loop Operation with Beam Acceleration

During the commissioning phase of the TTF linac, radioactive activation due to beam losses had to be minimized. The beam macro pulses were therefore shortened to 30  $\mu s$ . The maximum beam current of TTF injector I is 8 mA. The acceleration of the beam has been performed with different beam currents. Because of the dominating repetitive error sources, an adaptive feed forward correction has been applied. In Figure 4.16, the vector

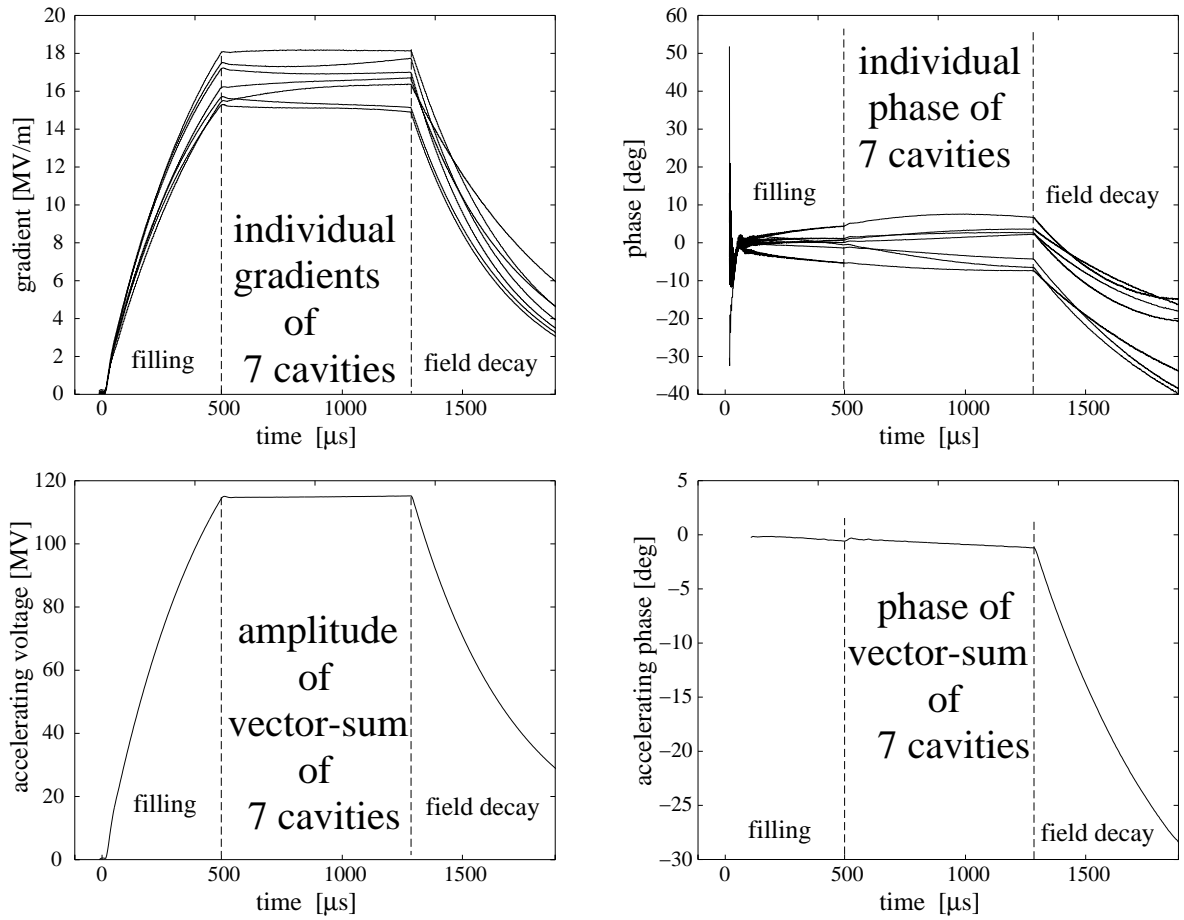


Figure 4.15: Closed loop operation of cryomodule 1 with seven cavities tuned on resonance without beam acceleration. The upper two plots show the gradients and phases of the individual cavities versus time. The lower two plots display the corresponding accelerating voltage and phase of the vector sum. The feedback loop gain was set to 30.

sum amplitude of the acceleration voltage of the cryomodule is plotted versus time, in Figure 4.17 the phase is shown. Beam acceleration with feedback only (feedback gain 70) and with additional adaptive feed forward are compared. Time delay in the feedback loop together with the high gain leads to oscillations in amplitude and phase. The measurements were performed by controlling the vector sum of five cavities. The beam current was 6 mA. The rms errors are calculated for the whole flattop range of 800  $\mu\text{s}$ . The amplitude and phase stabilities achieved were:

$$\begin{aligned}
\text{without feed forward, feedback gain} = 70 : & \quad \left(\frac{\sigma_V}{V}\right)_{rms} = 5 \cdot 10^{-3} ; \quad (\sigma_\varphi)_{rms} = 0.1^\circ \\
\text{with feed forward, feedback gain} = 70 : & \quad \left(\frac{\sigma_V}{V}\right)_{rms} = 5 \cdot 10^{-4} ; \quad (\sigma_\varphi)_{rms} = 0.03^\circ
\end{aligned}$$

The slope on the phase results from Lorentz force detuning during the RF pulse. It is repetitive and was compensated by feed forward.

The comparison of the stability achieved with the requirements for TESLA 500 yields that the measured total amplitude error is a factor of 10 below the tolerable uncorrelated amplitude error ( $5 \cdot 10^{-3}$ ). The measured phase error outperforms the tolerable uncorrelated phase error ( $0.5^\circ$ ) by a factor of 16. It still has to be demonstrated that the attained amplitude and phase stability can also be reached with full beam pulse length of  $800 \mu\text{s}$ .

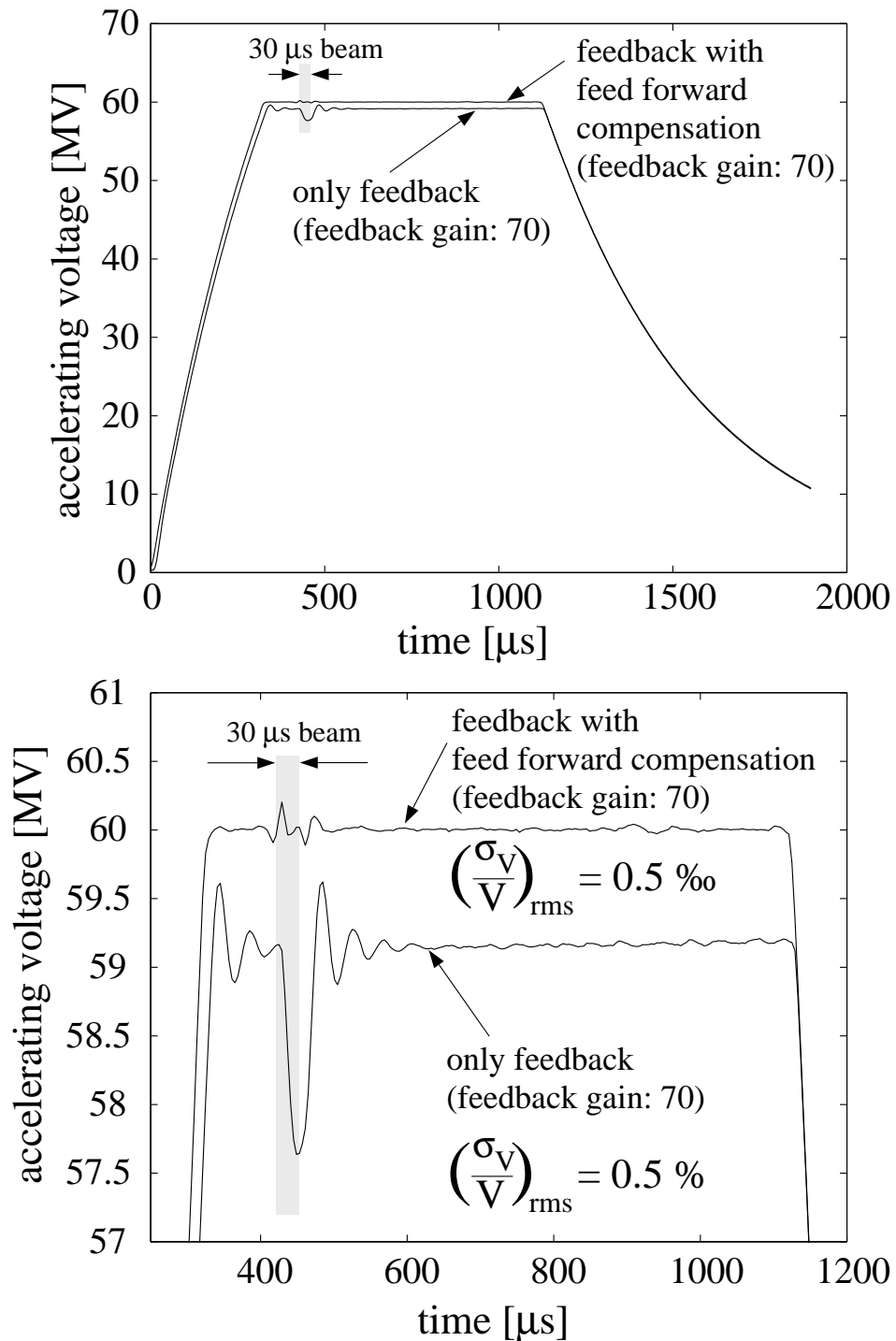


Figure 4.16: Acceleration voltage of cryomodule 1 with five cavities tuned on resonance. The macro beam pulse length was 30  $\mu\text{s}$ . The upper plot show the accelerating voltage versus time. The feedback loop gain was set to 70. The two curves represent the performance with and without feed forward compensation.

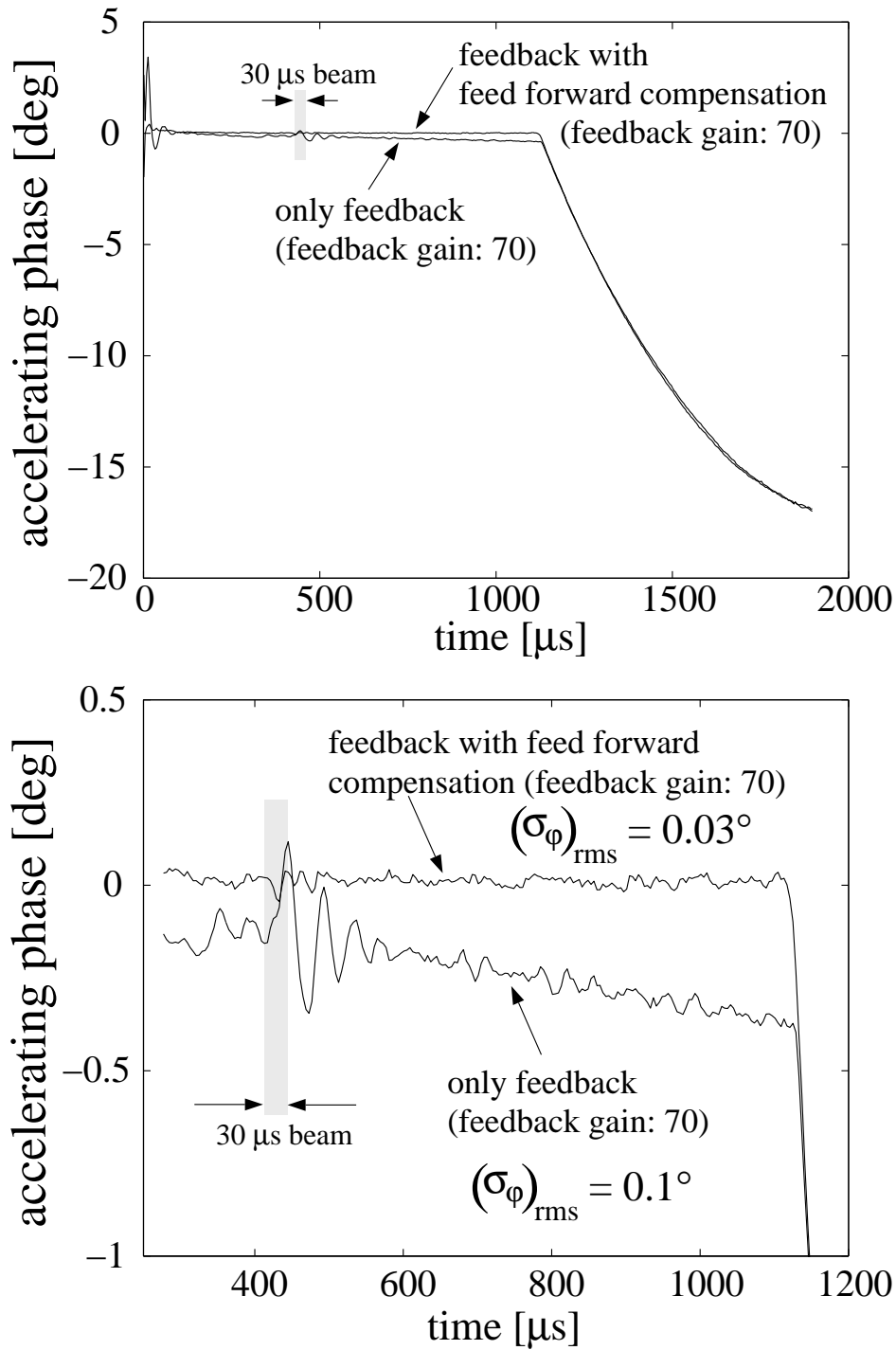


Figure 4.17: Closed loop operation of cryomodule 1 with five cavities tuned on resonance. The macro beam pulse length was  $30 \mu\text{s}$ . The upper plot shows the accelerating phase versus time. In the lower plot the phase of the vector sum is displayed. The feedback loop gain was set to 70. The two curves represent the performance with and without feed forward compensation

## Chapter 5

# Stability Investigations of Feedback System

Modern control theory is applied to investigate the stability and performance of the whole RF system. On the basis of this theory, the system is divided into different blocks as shown in Figure 5.1. Each block is described by an appropriate representation which can be state space or transfer matrix.

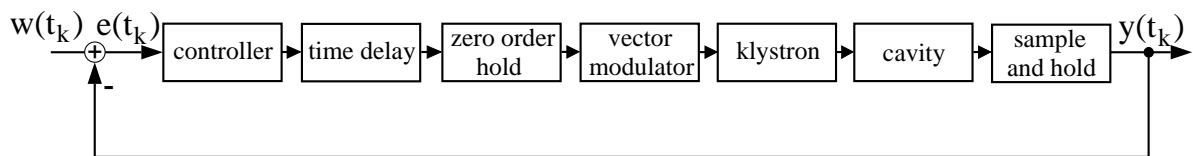


Figure 5.1: Simplified block model for the RF feedback system. The sample and hold block gives discrete time samples of the cavity voltage  $V$  at time  $t_k$ . The input of the controller is the error signal  $e(t_k)$  which is the difference between the setpoint  $w(t_k)$  and the cavity voltage  $y(t_k) = V(t_k)$ .

In the state space representation [Lud 96], each subsystem is characterized by a set of four matrices and a vector called state vector. The relation between system input and output is given by two matrix equations. A series of subsystems can be combined in a state vector composed of the individual state vectors. The corresponding matrices for the total system are a combination of the subsystem matrices. Even the simplified block model (Figure 5.1) yields a fairly complicated description in state space.

In contrast, the transfer matrix representation directly relates the input vector to the output vector by a matrix in the complex frequency domain, namely the transfer matrix. For this purpose, the differential equation which describes a system is transformed into the complex frequency domain by means of Laplace transformation. The output vector of a subsystem is just the input vector of the next subsystem. In our case, the input/output vector consists of two components: the real and imaginary voltages. In chapter 3 it has been shown that the output of the klystron is described by a current. For the purpose of

stability analysis, the use of voltages is more appropriate. The current is transformed into a corresponding voltage. All the transfer matrices of the subsystems are  $2 \times 2$  matrices, as is the transfer matrix of the whole system. Therefore, the representation more appropriate is therefore the transfer matrix representation which will be used in the following section. Since the RF control system is implemented as a digital system, the transition from continuous to discrete representation has to be performed. In this, the model of the cavity includes the  $\pi$ -accelerating mode and the next passband mode, the  $\frac{8}{9}\pi$ -mode. For discrete representation, the transfer matrices (in the Laplace space) have to be transformed into the  $z$ -space by  $z$ -transformation [Lu/We]. In control theory, stability analysis can be effected by different means, using algebraic or geometric stability criterions.

Algebraic methods (Routh criterion, Hurwitz criterion) are based on calculating the poles of a transfer matrix. The location of the poles provides information with regard to stability. The disadvantages of these methods are: it can be difficult to calculate the poles analytically; and, moreover, these methods cannot be extended to systems with time delays. Algebraic methods cannot be applied to discrete systems (digital systems) in which time delays are present [Lu/We], whereas, however, geometric stability criterions can also be applied to systems with time delays. Therefore, we investigate the digital RF control system with geometric methods using Bode and Nyquist criterions. Since every input signal fed into a system can be decomposed into its Fourier components, it is important to know how a system reacts on a harmonic input. This is why a Bode diagram is used in which the frequency response on a harmonic input signal is shown. The response signal is plotted as amplitude and phase versus the logarithmic excitation frequency. In RF systems, it is only the frequency offset to the operating frequency  $f_{RF}$  ( $\omega_{RF}$ ) that is of interest. The frequency on the horizontal axis in the following Bode plots is given by  $\omega_{Bode} = \omega_{RF} - \omega$ .

## 5.1 Transfer Matrix Representation of Discrete System

For the purpose of stability analysis, the open loop transfer matrix of the whole system is required. A discrete system is characterized by the fact that the signal, which has to be controlled, is sampled, and that the output signal of the controller is kept constant between two sampling times (sampling period  $T_s$ ). In the block diagram in Figure 5.1, this is described by the sample and hold block and by the zero-order hold block. In reality, it is the ADC which performs the sampling and the DAC which delivers a constant output for a sampling period  $T_s$ . The feedback controller (digital signal processor) is discrete but vector modulator, klystron and cavity are continuously working devices. The zero-order hold guarantees continuous input to these devices. The transition from a continuous to a discrete representation of a system with both continuous and discrete devices has to be performed in several steps (see Figure 5.2): Firstly, we have to calculate the total transfer matrix of the continuous devices in series. In the transfer matrix representation, we only

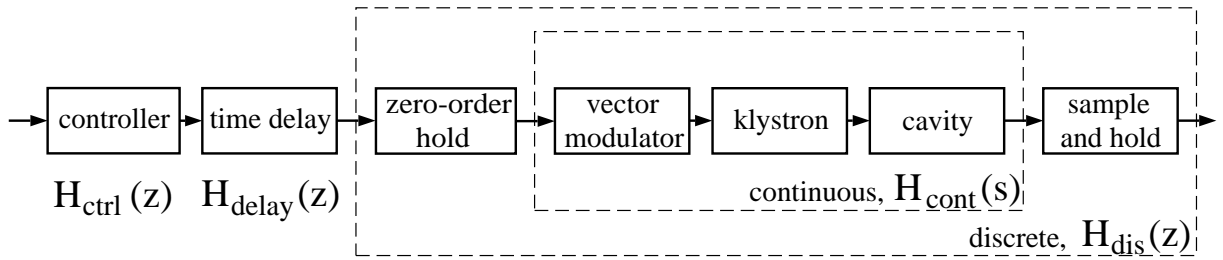


Figure 5.2: Transition from continuous to discrete system model. The continuously working devices are combined in transfer matrix  $H_{cont}$ . It is connected in series with the transfer matrix of the zero-order hold block resulting in the discrete description  $H_{dis}$  of a continuous module with input from a discrete controller.

have to multiply the successive matrices of the individual subsystems. Secondly, the total transfer matrix of the continuous devices is connected in series with the zero-order hold and then transformed into the discrete representation. This includes the sample and hold block at the output of the continuous devices. Finally, the discrete feedback controller and the discrete time delay are connected in series with the discrete transfer matrix of the device so as to get the open loop transfer matrix of the whole system. Before we calculate the transfer matrices of the individual subsystems, the transformation from continuous to discrete is discussed in more detail. A transformation rule will be deduced.

A zero-order hold block gives a constant output  $y(t)$  of the discrete inputs  $u_k = u(t_k)$  at times  $t_k$  between the sample times  $t_k$  and  $t_{k+1} = t_k + T_s$  with  $k = 0, 1, 2, \dots$  (see Figure 5.3). A single step is described by two Heavyside step functions  $\theta(t)$  where  $\theta(t)$  is 1 for

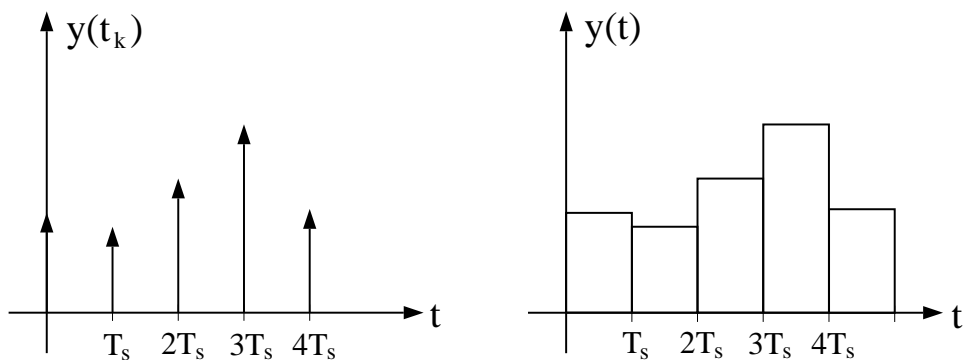


Figure 5.3: Input and output function of a zero-order hold block.

$t \geq 0$  and 0 elsewhere. The steps at the output are given by

$$y(t) = \sum_{k=0}^{\infty} u_k \cdot [\theta(t - k \cdot T_s) - \theta(t - (k + 1) \cdot T_s)]$$

To obtain the transfer matrix of a zero-order hold, we have to apply Laplace transformation to this equation:

$$\begin{aligned} y(s) &= \sum_{k=0}^{\infty} u_k \cdot \left[ \frac{e^{-k \cdot T_s \cdot s}}{s} - \frac{e^{-(k+1) \cdot T_s \cdot s}}{s} \right] = \frac{1 - e^{-T_s \cdot s}}{s} \cdot \sum_{k=0}^{\infty} u_k \cdot e^{-k \cdot T_s \cdot s} \\ &= \frac{1 - e^{-T_s \cdot s}}{s} \cdot u^*(s) \end{aligned}$$

$$\text{with } u^*(s) = \sum_{k=0}^{\infty} u_k \cdot e^{-k \cdot T_s \cdot s} .$$

The input  $u^*(s)$  is defined as the Laplace transformed function of  $u(t)$  which is the discrete impulse function at sample times  $t = k T_s$ :

$$u^*(s) = \mathcal{L} \left\{ \sum_{k=0}^{\infty} u(k \cdot T_s) \cdot \delta(t - k \cdot T_s) \right\}$$

The transfer matrix for a zero-order hold is

$$H_{ZOH}(s) = \frac{1 - e^{-T_s \cdot s}}{s} \cdot \mathbf{1}$$

where the unitary matrix  $\mathbf{1}$  has the dimension of the input vector  $u(k \cdot T_s)$ . The transformation from continuous to discrete requires the zero-order hold and the following continuous transfer matrix to be connected in series. Subsequently, we have to apply inverse Laplace transformation so as to return to the time domain. Inserting the discrete times  $t_k = k \cdot T_s$  and calculating the  $z$ -transformation, we end up in the discrete complex frequency domain. The transition from the continuous to the discrete transfer matrix is illustrated in Figure 5.4. The discrete transfer matrix  $H_{dis}(z)$  of a continuous plant with input from a zero-order block is

$$H_{dis}(z) = \mathcal{Z} \{ \mathcal{L}^{-1} \{ H_{cont}(s) \cdot H_{ZOH}(s) \} |_{t=kT_s} \} .$$

These two transformations are simply written as

$$H_{dis}(z) = \mathcal{Z} \{ H_{cont}(s) \cdot H_{ZOH}(s) \} .$$

With the transfer matrix  $H_{ZOH}(s)$  we get

$$\begin{aligned} H_{dis}(z) &= \mathcal{Z} \left\{ \frac{1 - e^{-T_s \cdot s}}{s} \cdot H_{cont}(s) \right\} \\ &= \mathcal{Z} \left\{ \frac{H_{cont}(s)}{s} \right\} - \mathcal{Z} \left\{ e^{-T_s \cdot s} \cdot \frac{H_{cont}(s)}{s} \right\} . \end{aligned}$$

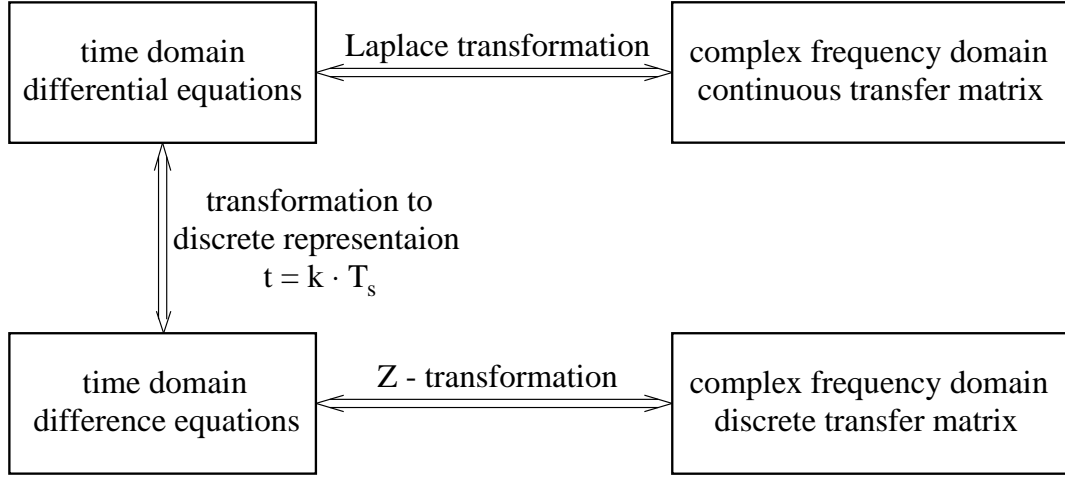


Figure 5.4: Transition from continuous to discrete transfer matrix

The factor  $e^{-T_s \cdot s}$  represents a time delay  $T_s$  in Laplace domain. The corresponding time delay in  $z$ -domain is a multiplication with  $\frac{1}{z}$ . The discrete transfer matrix can be expressed as

$$H_{dis}(z) = \left(1 - \frac{1}{z}\right) \mathcal{Z} \left\{ \frac{H_{cont}(s)}{s} \right\} = \frac{z-1}{z} \cdot \mathcal{Z} \left\{ \mathcal{L}^{-1} \left\{ \frac{H_{cont}(s)}{s} \right\} \Big|_{t=kT_s} \right\} . \quad (5.1)$$

## 5.2 Transfer Matrices of the Subsystems

In this section, the transfer matrices of the individual subsystems (elements) are deduced. The digital feedback controller and the time delay are directly described by discrete transfer matrices while the vector modulator, the klystron and the two passband modes ( $\pi$ - and  $\frac{8}{9}\pi$ -mode) of the cavity are given in a continuous representation. The transformation of these continuous operating devices to a discrete transfer matrix is performed in section 5.3. Most of the transfer matrices for common elements (for example a lowpass filter) can be looked up in standard text books on control theory and are therefore only listed.

### (a): feedback controller

The feedback algorithm is realized as a proportional gain controller with a digital lowpass filter on the input data. The discrete transfer matrix of a proportional gain is

$$H_P(z) = K \cdot \mathbf{1} \quad \text{with gain } K .$$

To calculate the discrete transfer matrix of the digital lowpass filter, we start with the difference equation 4.1.

$$\bar{V}_x(t_{k+1}) = \left(1 - \frac{1}{N}\right) \cdot \bar{V}_x(t_k) + \frac{1}{N} \cdot V_x(t_k)$$

$$\bar{V}_y(t_{k+1}) = \left(1 - \frac{1}{N}\right) \cdot \bar{V}_y(t_k) + \frac{1}{N} \cdot V_y(t_k)$$

To transform this difference equation into  $z$ -space, the following transformation rules have to be applied:

$$\begin{aligned} \text{transformation rule:} \quad \bar{V}(t_{k+1}) &\longrightarrow z \cdot \bar{V}(z) \\ \bar{V}(t_k) &\longrightarrow \bar{V}(z) \\ V(t_k) &\longrightarrow V(z) \end{aligned}$$

Obeying these rules yields

$$\bar{V}_x(z) = \frac{\frac{1}{N}}{z - \left(1 - \frac{1}{N}\right)} \cdot V_x(z)$$

$$\bar{V}_y(z) = \frac{\frac{1}{N}}{z - \left(1 - \frac{1}{N}\right)} \cdot V_y(z)$$

Therefore, the transfer matrix of the digital lowpass filter is

$$H_{filt}(z) = \frac{\frac{1}{N}}{z - \left(1 - \frac{1}{N}\right)} \cdot \mathbf{1}$$

In control theory literature, a first order lowpass filter is given by

$$\begin{array}{ll} \text{continuous transfer function:} & \text{discrete transfer function:} \\ H_{filt}(s) = \frac{\omega_{filt}}{s + \omega_{filt}} & \iff H_{filt}(z) = \frac{1 - e^{-\omega_{filt} \cdot T_s}}{z - e^{-\omega_{filt} \cdot T_s}} \end{array}$$

where  $T_s$  is the sampling period and  $\omega_{filt}$  the roll-off frequency. This frequency is defined as the frequency at which the amplitude of the output decreases to  $1/\sqrt{2}$  of the input amplitude. A comparison between the continuous and discrete representation yields

$$\left(1 - \frac{1}{N}\right) = e^{-\omega_{filt} \cdot T_s} \iff \omega_{filt} = -\frac{1}{T_s} \ln\left(1 - \frac{1}{N}\right)$$

The roll-off frequency for different filter parameters  $N$  is given in table 5.1. The transfer matrix of the digital controller is the product of proportional gain and lowpass filter transfer matrices.

$$H_{ctrl}(z) = H_P(z) \cdot H_{filt}(z) = K \cdot \frac{\frac{1}{N}}{z - \left(1 - \frac{1}{N}\right)} \cdot \mathbf{1}$$

(b): **time delay**

A time delay  $T_d$  is represented in Laplace space by a factor of  $e^{-T_d \cdot s}$  while in discrete

filter parameter $N$	roll-off frequency $f_{filt}$
$N = 1$	no filter
$N = 2$	$f_{filt} = 110$ kHz
$N = 3$	$f_{filt} = 65$ kHz
$N = 4$	$f_{filt} = 46$ kHz
$N = 5$	$f_{filt} = 36$ kHz

Table 5.1: Roll-off frequency of digital lowpass filter

$z$ -domain it is expressed by a factor of  $\frac{1}{z^m}$ . The number  $m$  is an integer multiple of the sampling time  $T_s$ :  $m = \frac{T_d}{T_s}$ . The transfer matrix of a time delay is:

$$H_{delay}(z) = \frac{1}{z^m} \cdot \mathbf{1} \quad \text{with } m = \frac{T_d}{T_s}$$

In the RF control system of the TESLA Test Facility, the total delay in the feedback loop is  $T_d = 5 \mu s$ . With a sampling time of  $T_s = 1 \mu s$  we get  $m = 5$ .

(c): **vector modulator**

A vector modulator can be modelled as a lowpass filter with respect to the operating frequency  $\omega_{RF}$ . The response of a step input has a limited rise time and is similar to a first order lowpass filter with roll-off frequency  $\omega_{vec}$ . Measurements have shown that  $\omega_{vec}/(2\pi)$  is approximately 10 MHz. The transfer function is given by:

$$H_{vec}(s) = \frac{\omega_{vec}}{s + \omega_{vec}} \cdot \mathbf{1}$$

(d): **klystron**

The klystron is a high power RF amplifier with a bandpass characteristic around the operating frequency  $\omega_{RF} = 2\pi \cdot 1.3$  GHz. It consists of five cavities in series. The amplitude of the klystron has been measured versus the RF frequency. The amplitude decreases by 1 dB at a frequency difference of 7 MHz with respect to  $\omega_{RF}$  [Ga]. In the stability analysis, the transfer characteristic of the klystron is described by a first order lowpass filter with a roll-off frequency of  $\omega_{kly} = 2\pi \cdot 8$  MHz.

$$H_{kly}(s) = \frac{\omega_{kly}}{s + \omega_{kly}} \cdot \mathbf{1}$$

(e): **cavity**

The deduction of the transfer matrix of a cavity starts with the differential equation 3.49 for real and imaginary parts.

$$\frac{d}{dt} \begin{pmatrix} V_r(t) \\ V_i(t) \end{pmatrix} = \begin{pmatrix} -\omega_{1/2} & -\Delta\omega \\ \Delta\omega & -\omega_{1/2} \end{pmatrix} \begin{pmatrix} V_r(t) \\ V_i(t) \end{pmatrix} + R_L \cdot \omega_{1/2} \begin{pmatrix} 1 & 0 \\ 0 & 1 \end{pmatrix} \begin{pmatrix} I_r(t) \\ I_i(t) \end{pmatrix} \quad (5.2)$$

Applying Laplace-transformation and solving for  $U_r(s), U_i(s)$  yields (with  $\mathbf{u}(s) = \begin{pmatrix} R_L \cdot I_r(t) \\ R_L \cdot I_i(t) \end{pmatrix}$ )

$$\mathbf{y}(s) = \begin{pmatrix} V_r(s) \\ V_i(s) \end{pmatrix} = \frac{\omega_{1/2}}{\Delta\omega^2 + (s + \omega_{1/2})^2} \begin{pmatrix} s + \omega_{1/2} & -\Delta\omega \\ \Delta\omega & s + \omega_{1/2} \end{pmatrix} \begin{pmatrix} R_L \cdot I_r(s) \\ R_L \cdot I_i(s) \end{pmatrix}. \quad (5.3)$$

The transfer matrix  $H(s)$  defined by  $\mathbf{y}(s) = H(s) \cdot \mathbf{u}(s)$  is therefore given by

$$H_{cav}(s) = \frac{\omega_{1/2}}{\Delta\omega^2 + (s + \omega_{1/2})^2} \begin{pmatrix} s + \omega_{1/2} & -\Delta\omega \\ \Delta\omega & s + \omega_{1/2} \end{pmatrix} = \begin{pmatrix} H_{11}(s) & H_{12}(s) \\ H_{21}(s) & H_{22}(s) \end{pmatrix} \quad (5.4)$$

The off-diagonal elements are the transfer functions which describe the coupling from real to imaginary parts and vice versa. This is illustrated in Figure 5.5.

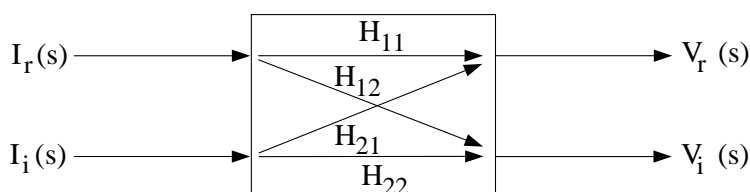


Figure 5.5: Transfer matrix representation of cavity input current to cavity output voltage.

As demonstrated by equation 5.4, real and imaginary parts are completely decoupled for a cavity operated on resonance ( $H_{12} = H_{21} = 0$ ). However, if the cavity is detuned, the amplitude of the direct transfer functions  $H_{11}(s)$  and  $H_{22}(s)$  are proportional to  $\frac{1}{\omega}$  for high frequencies ( $s = j\omega$ ):

$$|H_{11}(s)|, |H_{22}(s)| \sim \frac{1}{\omega} \quad \text{for } |s| \gg \omega_{1/2}, |s| \gg \Delta\omega,$$

which means the amplitude rolls off by 20 dB per decade. In this case, the cross transfer functions  $H_{12}(s)$  and  $H_{21}(s)$  are proportional to  $\frac{1}{\omega^2}$ .

$$|H_{12}(s)|, |H_{21}(s)| \sim \frac{1}{\omega^2} \quad \text{for } |s| \gg \omega_{1/2}, |s| \gg \Delta\omega,$$

which is equivalent to a 40 dB decline per decade. The conclusion is that the coupling of passband mode of a slightly detuned cavity ( $\Delta\omega$  in the order of  $\omega_{1/2}$ ) becomes negligible for high frequencies. The Bode plots of a detuned and a tuned cavity are shown in Figure 5.6. The bandwidth of both is  $f_{1/2} = 215$  Hz, and the detuning is  $\Delta f = 100$  Hz. The transfer matrix  $H(s)$  describes one passband mode. The stability of the RF control system is investigated taking into account the  $\pi$ -accelerating mode and the closest passband mode, the  $\frac{8}{9}\pi$ -mode. Since both

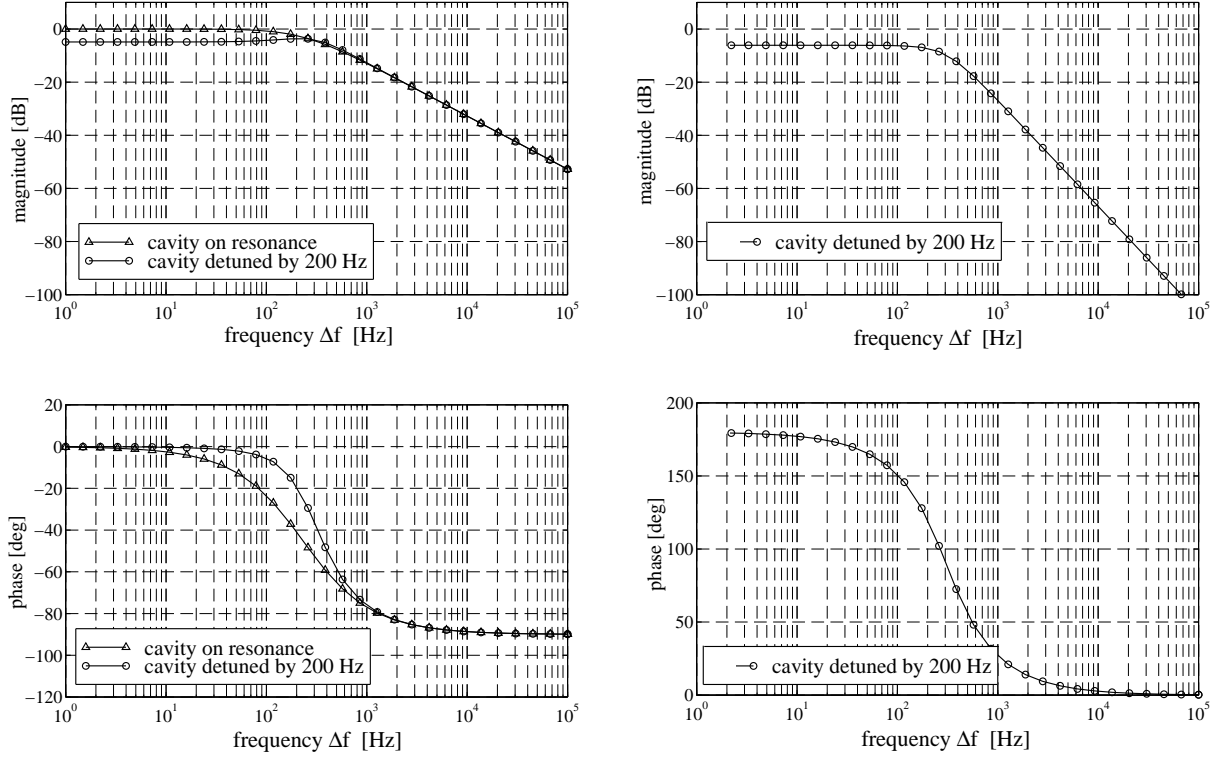


Figure 5.6: Bode plots of the transfer matrix of a detuned cavity ( $\Delta f = 100 \text{ Hz}$ ,  $\Delta f_{1/2} = 215 \text{ Hz}$ ).  
 Left diagrams: Transfer function  $H_{11}(s)$ .  
 Right diagrams: Transfer function  $H_{21}(s)$ . The transfer function of the cavity on resonance is zero.

modes can be excited, they are described by transfer matrices which are connected in parallel. It has to be taken into account that the  $\pi$ - and the  $\frac{8}{9}\pi$ -mode have a phase difference of  $\pi$  in the ninth cell in which the field is detected with a pick-up antenna. Hence, an additional phase shift of  $\pi$  has to be applied resulting in a minus sign in the transfer matrix of the  $\frac{8}{9}\pi$ -mode.

$$\begin{aligned}
 \pi\text{-mode} \quad H_{\pi}(s) &= \frac{(\omega_{1/2})_{\pi}}{\Delta\omega_{\pi}^2 + (s + (\omega_{1/2})_{\pi})^2} \begin{pmatrix} s + (\omega_{1/2})_{\pi} & -\Delta\omega_{\pi} \\ \Delta\omega_{\pi} & s + (\omega_{1/2})_{\pi} \end{pmatrix} \\
 \frac{8}{9}\pi\text{-mode} \quad H_{\frac{8}{9}\pi}(s) &= -\frac{(\omega_{1/2})_{\frac{8}{9}\pi}}{\Delta\omega_{\frac{8}{9}\pi}^2 + (s + (\omega_{1/2})_{\frac{8}{9}\pi})^2} \begin{pmatrix} s + (\omega_{1/2})_{\frac{8}{9}\pi} & -\Delta\omega_{\frac{8}{9}\pi} \\ \Delta\omega_{\frac{8}{9}\pi} & s + (\omega_{1/2})_{\frac{8}{9}\pi} \end{pmatrix} \\
 H_{cav}(s) &= H_{\pi}(s) + H_{\frac{8}{9}\pi}(s)
 \end{aligned}$$

In chapter 4.5.2, it has been shown that the dynamics of eight cavities connected in parallel is similar to the dynamics of a single cavity. Stability investigations can therefore be reduced to a single cavity.

### 5.3 Open Loop Transfer Matrix of the Digital RF Feedback System

After determining the individual subsystems, the open loop transfer matrix can be calculated. Firstly, the continuous devices are connected in series giving  $H_{cont}(s)$ .

$$H_{cont}(s) = H_{cav}(s) \cdot H_{kly}(s) \cdot H_{vec}(s)$$

The conversion from continuous to discrete representation is performed with the zero-order hold element by the transformation equation (5.1).

$$H_{dis}(z) = \left(1 - \frac{1}{z}\right) \mathcal{Z} \left\{ \frac{H_{cont}(s)}{s} \right\} = \frac{z-1}{z} \cdot \mathcal{Z} \left\{ \mathcal{L}^{-1} \left\{ \frac{H_{cont}(s)}{s} \right\} \Big|_{t=kT_s} \right\}$$

It turns out that the influence of the bandwidth of the vector modulator and the klystron can be neglected. This is shown in Figure 5.7 and 5.8. In this Bode plot, the direct transfer functions  $H_{11} = H_{22}$ ,  $H_{12} = -H_{21}$  are displayed in the continuous (thick solid line) and in the discrete representation (thin dashed line). The sampling frequency of the digital system is 1 MHz. Consequently, frequencies of up to 500 kHz can be identified. Due to aliasing, the  $\frac{8}{9}\pi$ -mode is mapped from 800 kHz to 200 kHz. On account of this, the amplitude decreases by 10 dB. The description of the continuously working module can be simplified by neglecting the vector modulator and klystron. The transfer functions of the discrete transfer matrix of the cavity with two passband modes is plotted as a dashed line. The difference to the more extended model with klystron and vector modulator is only visible close to the  $\frac{8}{9}\pi$ -mode but is negligible in the stability analysis. Therefore, we reduce our model and investigate only the discrete cavity model.

$$H_{cont}(s) \approx H_{cav}(s) \quad \Longrightarrow \quad H_{dis}(z)$$

Continuing with the series connection of the time delay  $H_{delay}(z)$  and the controller  $H_{ctrl}(z)$ , we obtain the open loop transfer matrix of the digital RF control system.

$$H_{tot}(z) = H_{dis}(z) \cdot H_{delay}(z) \cdot H_{ctrl}(z) \quad (5.5)$$

The analytical expression for the simplified transfer matrix  $H_{dis}(z)$  is given in appendix A.7.

## 5.4 Stability Analysis with Bode and Nyquist Plots

In the stability analysis for single-input single-output systems (SISO systems), stability criteria can be derived with the help of the open loop transfer function. In this, the critical point is where the phase of the open loop transfer function reaches  $-180^\circ$ . At that frequency, the negative feedback turns into positive feedback. If the loop gain is larger than one (=unity gain) at this point, the condition for oscillation is fulfilled. The control loop is unstable. This limits the bandwidth of feedback control. The model of the digital RF control system consists of input/output vectors with two components, the real and imaginary parts of the voltage. The corresponding  $2 \times 2$  transfer matrices describe multi-input multi-output systems (MIMO systems). Consequently, the general Nyquist criterion has to be applied to allow the examination of the stability of the digital RF control system [Lun 97]. If  $H_{tot}(z)$  denotes the open loop transfer matrix, the closed loop transfer matrix  $F(z)$  (feedback) of the system in Figure 5.1 is calculated to

$$F(z) = [\mathbf{1} + H_{tot}(z)]^{-1} H_{tot}(z) \quad (5.6)$$

However, a basic idea with regard to stability can be obtained by means of Bode plots of the direct transfer function  $(H_{tot})_{11} = (H_{tot})_{22}$ .

The open loop transfer function  $(H_{tot})_{11}$  of the total RF system is shown in a Bode plot in Figure 5.9. To estimate the critical gain  $K_{crit}$ , we start with a DC loop gain of one (lowest curve in the magnitude plot). The gain margin is determined by increasing the gain until unity gain is reached at the frequency at which the phase crosses the  $-180^\circ$  line. We obtain a critical gain of  $K_{crit} = 165$  ( $\approx 44$  dB). In practice, a gain below but close to  $K_{crit}$  results in overshooting and oscillations around the setpoint when step function are applied as inputs. This brings us to the subject of parameter optimization in feedback systems. We have used the method of ZIEGLER and NICHOLS [Lu/We]. It uses parameters at the stability limit to determine the operating point of the feedback loop. The optimal gain for a proportional gain controller is given by

$$K_{opt} = 0.5 \cdot K_{crit} .$$

For the digital RF control system, the optimum gain with this simplified analysis is  $K_{opt} = 80$ . The more exact stability investigation especially with regard to the  $\frac{8}{9}\pi$ -mode has to be performed with the general Nyquist criterion [Lun 97]:

*An open loop system with transfer matrix  $H_{tot}(z)$  results in a stable closed loop only if the equation*

$$\Delta \arg \det D(z) = -2n^+ \pi$$

*is fulfilled, i.e. if the Nyquist curve of  $\det D(z)$  encircles the origin  $-n^+$  times in the clockwise direction. In this,  $n^+$  is the number of poles of  $H_{tot}(z)$  with absolute values bigger than one (outside the unity circle).*

With  $\det D(z) = [\mathbf{1} + H_{tot}(z)]$  being the determinant of the feedback difference matrix (see equation (5.6)). The curve  $\det D(z)$  has to be calculated for values of  $z$  along the unity circle. It corresponds to a frequency sweep in the Laplace space  $s = j0 \dots -j\infty$ . The transformation to  $z$ -space given by  $z = e^{sT_s}$  maps the imaginary axis to the unity circle in which  $T_s$  denotes the sampling time. The precondition for the Nyquist criterion for digital systems is that the open loop systems have no poles on the unity circle. Calculating the poles of the transfer matrix  $H_{tot}(z)$  of the digital RF control system yields that all poles lie inside the unity circle, i.e. their absolute value is smaller than 1. Therefore, the Nyquist criterion can be applied and  $n^+$  is equal to zero. For stability, the Nyquist curve must not encircle the origin. In Figure 5.10, the Nyquist curve is plotted on the basis of a feedback loop gain of 100, no digital lowpass filter (filter parameter  $N = 1$ ), time delay  $T_d = 5 \mu s$  and the frequency of the  $\frac{8}{9}\pi$ -mode  $f_{\frac{8}{9}\pi} = 800 \text{ kHz}$ . With there being no digital lowpass filter, the loop gain can be increased up to  $K_{crit} = 210$ . According to the method of ZIEGLER and NICHOLS, the optimum proportional gain is

$$K_{opt} = 0.5 \cdot K_{crit} \approx 100 .$$

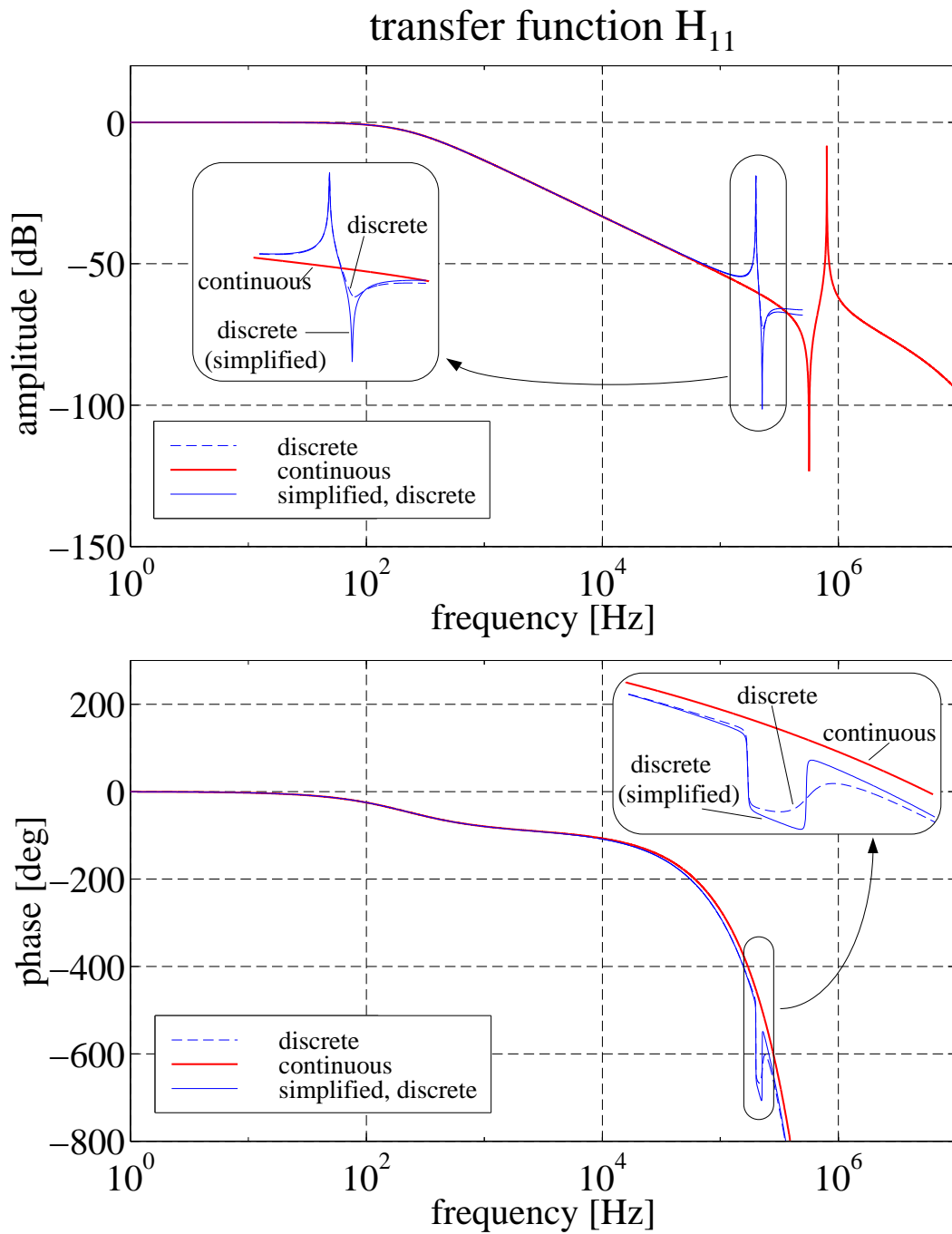


Figure 5.7: Comparison of continuous and discrete systems in Bode plots for the transfer matrix  $H_{11}$ . The simplified discrete system only consists of a cavity with  $\pi$ - and  $\frac{8}{9}\pi$ -mode.

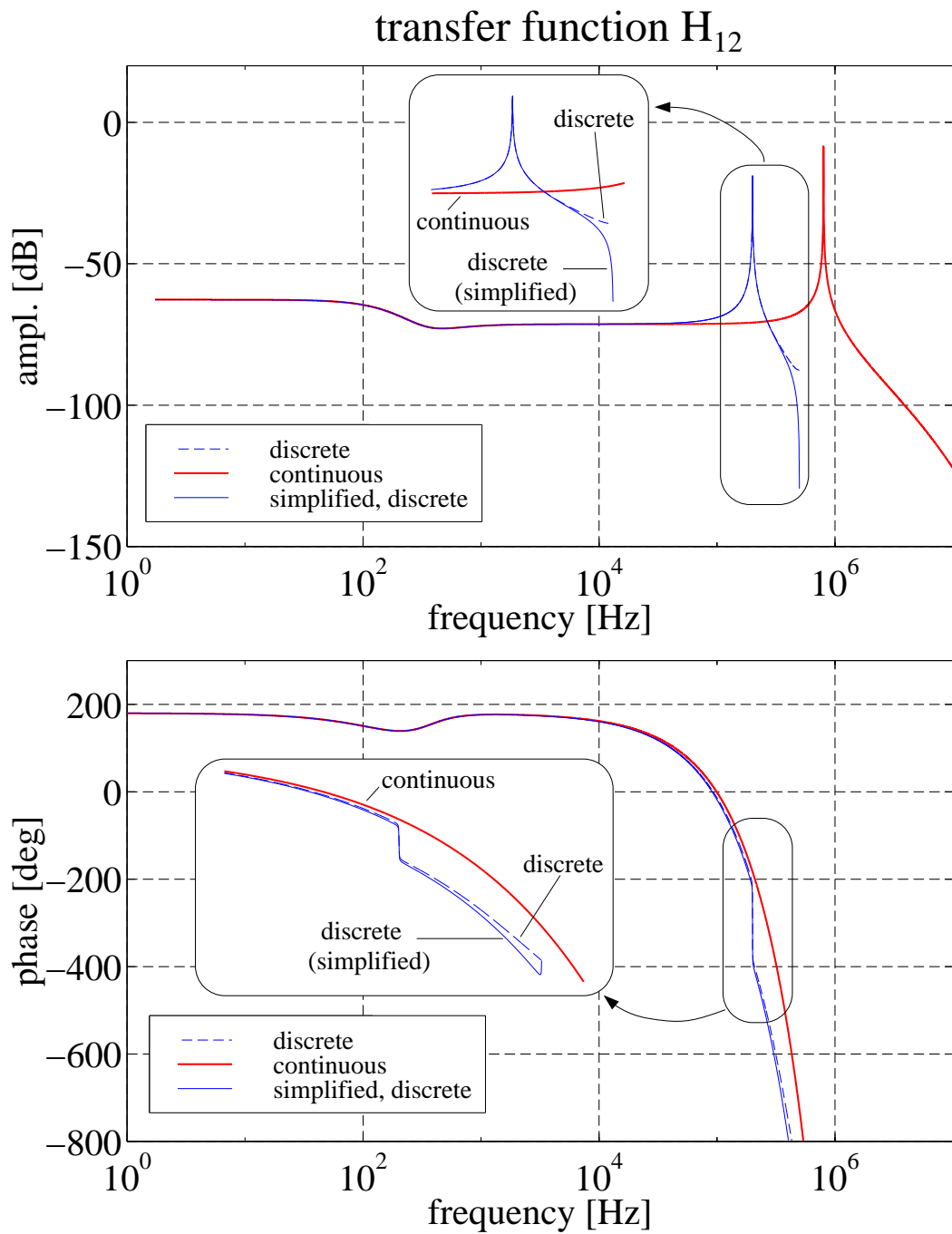


Figure 5.8: Comparison of continuous and discrete systems in Bode plots for the transfer matrix  $H_{12}$ . The simplified discrete system only consists of a cavity with  $\pi$ - and  $\frac{8}{9}\pi$ -mode.

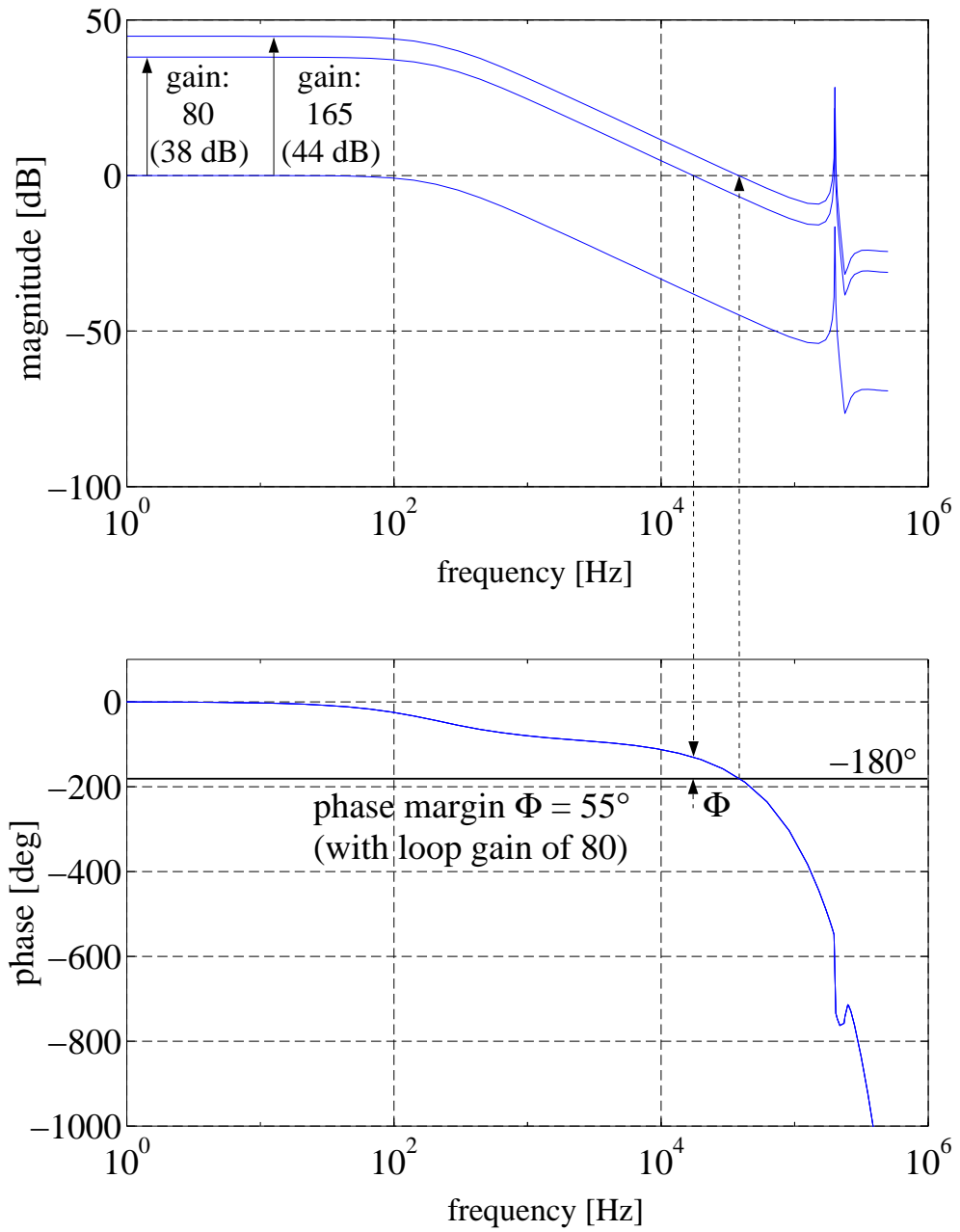


Figure 5.9: Bode plots of the open loop transfer function  $(H_{tot})_{11}$  of the TTF RF system.

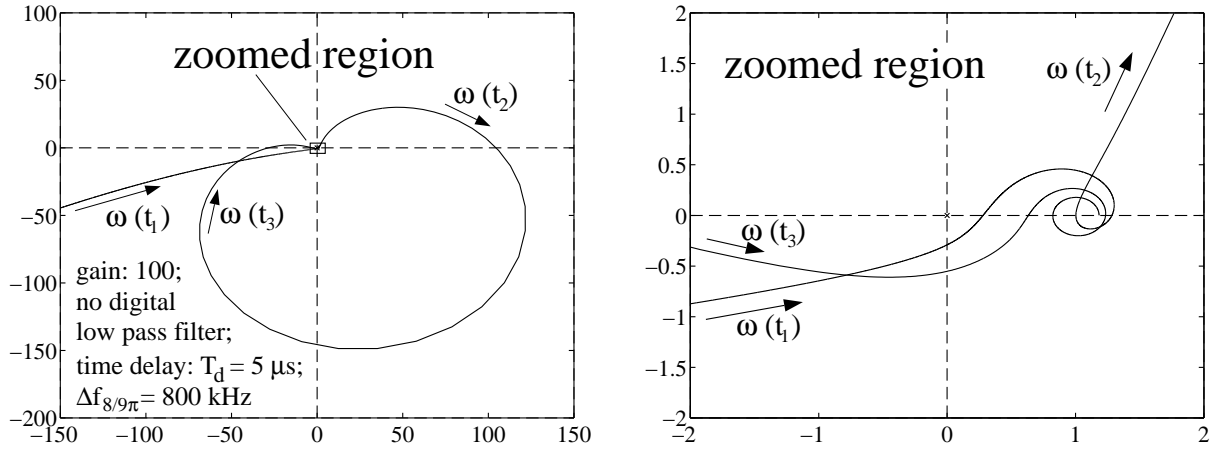


Figure 5.10: Determinant of the Nyquist curve as a function of frequency. The curve is traversed in the order  $t_1 < t_2 < t_3$ .

During the operation of the TESLA Test Facility, a digital lowpass filter with a roll-off frequency of  $f_{filt} = 110 \text{ kHz}$  has been applied to suppress sensor noise at  $250 \text{ kHz}$ . The effect of the lowpass filter for different roll-off frequencies is shown in Figure 5.11. The applied digital lowpass filter suppresses the sensor noise at  $250 \text{ kHz}$  by  $7 \text{ dB}$  approximately. The  $\frac{8}{9}\pi$ -mode is aliased to  $200 \text{ kHz}$  and consequently suppressed by approximately the same factor. The theoretical critical gain due to the digital lowpass filter with  $f_{filt} = 110 \text{ kHz}$  is reduced to  $190$  leading to a optimum gain of  $K_{opt} \approx 95$ . This is in agreement with the performance of the control system during operation. To minimize the overshoot after step responses, the loop gain was set to  $70$  (see Figure 4.16). Such step responses are for example power reductions that occur when the nominal accelerating gradient is reached after filling the cavity or injection of beam. This injection is equivalent to a step in the driving current of the cavity.

The difference frequency  $\Delta f_{8/9\pi}$  of the  $\frac{8}{9}\pi$ -mode with respect to the operating frequency is assumed to be in the range of  $800 \text{ kHz}$ . However, the TESLA cavities show a distribution of this frequency difference due to minimal variations occasioned in the manufacture of the cavities in the order of several  $10 \text{ kHz}$ . A variation of this parameter in the stability analysis has shown that the critical gain  $K_{crit}$  depends on the difference frequency  $\Delta f_{8/9\pi}$ . The stability analysis has been carried out with different settings of  $\Delta f_{8/9\pi}$  and different filter parameters  $f_{filt}$ . The  $\frac{8}{9}\pi$ -mode can reduce the maximum achievable gain. This can be understood with the help of the Bode plot of the open loop transfer function  $(H_{tot})_{11}$  (Figure 5.9). The amplitude of the transfer function shows the transmission of the  $\frac{8}{9}\pi$ -mode at the aliased frequency around  $200 \text{ kHz}$ . At this frequency, the phase varies with frequency due to the loop delay and due to the passband mode. A change in the frequency of the  $\frac{8}{9}\pi$ -mode by  $\Delta f_{8/9\pi}$  leads to a phase shift of  $\Delta\varphi = 2\pi\Delta f_{8/9\pi} \cdot T_d$  in

which  $T_d$  represents the loop delay. Depending on this delay, the feedback can be positive or negative. In the TESLA Test Facility, the accelerating fields of several cavities are controlled by one feedback system. The vector sum consists of the transmission of the  $\pi$ -mode of all cavities. They are tuned to the same frequency of the  $\pi$ -mode. However, the frequency spread of the  $\frac{8}{9}\pi$ -mode results in a transmission in the range of around 800 kHz below the fundamental mode frequency. Consequently, the sum of all  $\frac{8}{9}\pi$ -modes can have a much lower transmission than that in a single cavity. During the operation of the linac, no instabilities caused by this passband mode have been observed.

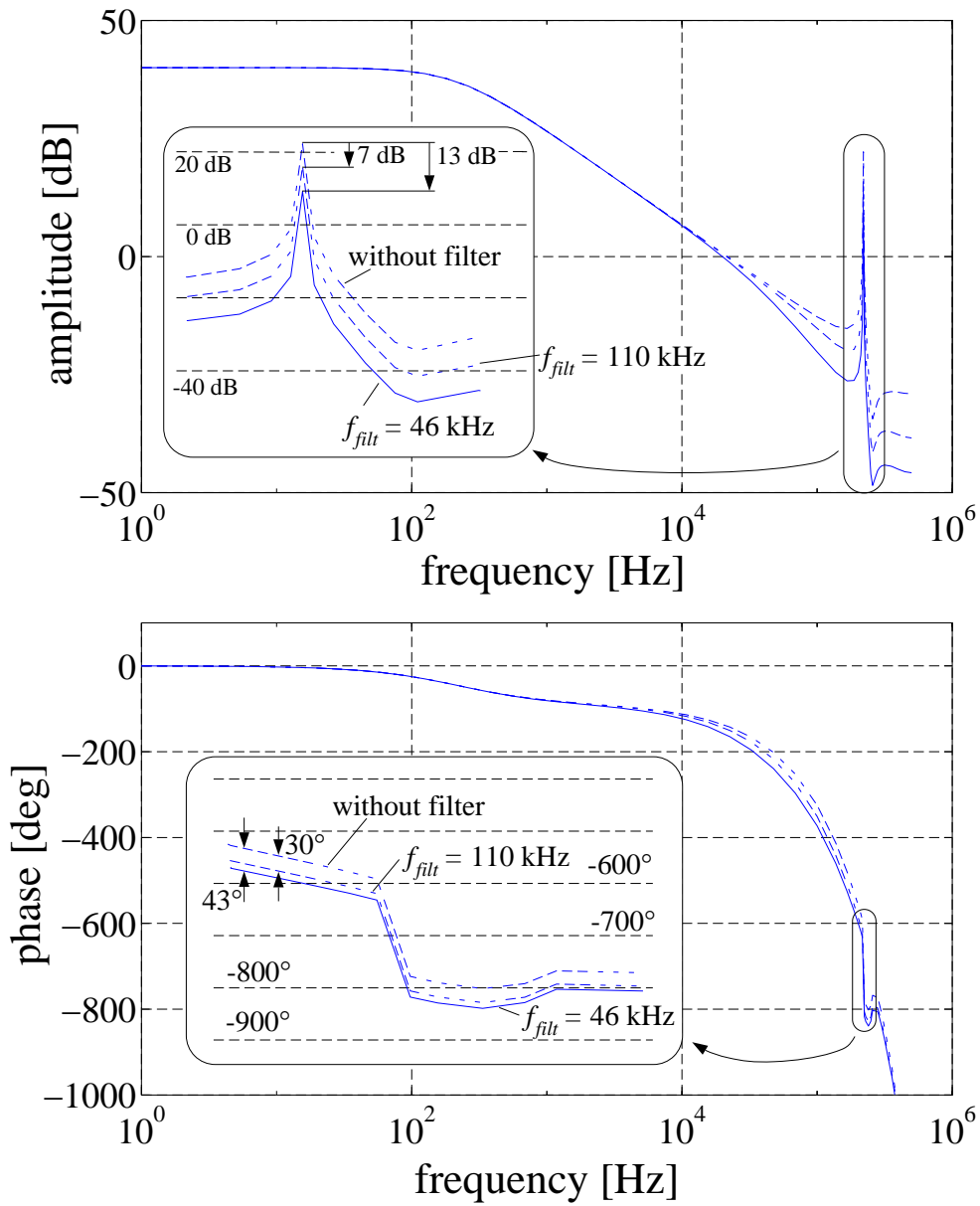


Figure 5.11: Effect of digital lowpass filter on the direct transfer function  $(H_{tot})_{11}$ . The Bode plots show the effect of the lowpass filter with three different roll-off frequencies.

With  $f_{filt} = 110$  kHz: transmission of the  $\frac{8}{9}\pi$ -mode suppressed by 7 dB.

With  $f_{filt} = 46$  kHz: transmission of the  $\frac{8}{9}\pi$ -mode suppressed by 13 dB.

## Chapter 6

# Mechanical Properties of the TESLA 9-cell Cavity

Superconducting cavities have high unloaded quality factors  $Q_0$  which are in the order of  $10^9$  to  $10^{11}$ . The optimum external  $Q_{ext}$  depends on the beam loading and is usually smaller than  $Q_0$  by a factor  $10^3$  to  $10^4$ . Therefore, the loaded  $Q_L$  is a good approximation of the external  $Q_{ext}$ . The resulting bandwidths of the resonators are in the order of a few hundred Hertz. The mechanical properties of superconducting cavities differ from those of normal conducting cavities on account of different materials and wall thicknesses being used and on their being employed under different operating conditions. Normal conducting cavities (usually copper cavities) are manufactured so as to be rigid so that they are mechanically stable and will withstand the great heat that is caused by the high dissipated power of several 10 kW per meter in a typical accelerating structure. Since the material used for the TESLA cavities is niobium of high purity, the costs increase with increasing wall thickness. In addition, the cooling capacity of superfluid Helium has to be taken into account. Consequently, the design of superconducting cavities makes them more susceptible to mechanical disturbances such as external mechanical excitations (microphonics) or Lorentz force detuning.

Microphonic noise modulates the resonance frequency of the cavities and changes the initial conditions at the beginning of an RF pulse. The knowledge about the microphonics level is of importance because several requirements for the RF control system are dependent on this level. Stochastic fluctuations of the resonance frequency that are due to microphonics demand extra RF power to maintain a constant accelerating field. Besides that, the stochastic errors in amplitude and phase have to be compensated for by a feedback system. The suppression of these errors requires a minimum gain to reduce the contribution to the energy spread. Finally, it has been discussed in chapter 2.1.3 that depending on the microphonics the calibration of the vector sum has to be within certain tolerable limits to keep the energy gain errors due to calibration errors small.

Lorentz forces detune the cavities repetitively from pulse to pulse. The dynamics has to be understood if more sophisticated feedback algorithms are to be applied to cavities operated in pulsed mode. It is planned to implement state estimators and Smith predictors

[Lev 95]. Based on the knowledge of the present driving term state estimators predict the state of the system in advance. The smith predictor compensates time delays in the feedback loop. These algorithms are based on a mathematical model which describes the control system. Since the detuning  $\Delta\omega$  of a cavity is one of the parameters in these models, the objective is to find a proper mathematical description of the dynamics of Lorentz force detuning.

Besides that, the pulsed operating mode of the cavities (with a pulse repetition rate of up to 10 Hz) represents a repetitive excitation of the niobium resonators. The structures may have mechanical resonances which could be excited by the periodical Lorentz forces. The build-up of a mechanical resonance leads to an oscillation of the electrical resonance frequency with an amplitude that depends on the quality factor of the mechanical resonance. If the amplitude of this frequency oscillation exceeds the power limit of the klystron, it is no longer possible to control the vector sum. This behavior has already become manifest in the operation of superconducting cavities in other accelerator laboratories [Doo/Sim]. In this chapter, the measured microphonics in the first accelerating module of the TESLA Test Facility is presented. Furthermore, it provides information about the studies performed on the Lorentz force detuning of the 9-cell cavities. Finally, resonance measurements of a TESLA cavity at room temperature are presented and compared to the excitation measurements of cold cavities.

## 6.1 Microphonics in the Module

Microphonics has been measured by means of the method described in section 4.4, according to which the resonance frequency is determined at the end of the RF pulse. For this purpose, the vector sum of seven cavities has been regulated at a constant gradient for several hours. The cavity filling time and the flattop period have been set to the design values of 500  $\mu\text{s}$  and 800  $\mu\text{s}$  respectively. During the first run of the linac, the mechanical tuners (stepper moter) were not used. The tuners are expected to compensate slow resonance frequency variations on a time scale of several seconds. The resulting resonance frequency measured at the end of the RF pulse versus time is shown in Figure 6.1. The variation in all cavities follow the same slow time dependency. Measurements of the helium pressure have indicated that a correlation between frequency and pressure variations with time constants in the order of several minutes. Tuner control of the individual cavities could reduce the fluctuations of the resonance frequencies  $\omega_0$ . The residual distribution of microphonics has been calculated on the assumption that the slow drift of  $\omega_0$  is compensated by the mechanical tuners. This will be demonstrated on the example of one cavity.

In Figure 6.2, the variation of the detuning of one cavity is plotted versus time (left diagram). When plotting the resonance frequency spread for the resonance frequency variation as shown in the left diagram, this results in a Gaussian distribution around the mean value -19 Hz with  $\sigma_{\Delta f} = 4$  Hz. The measured microphonic levels in the cavities are given in table 6.1. The mechanical tuners have been in a fixed postition. The he-

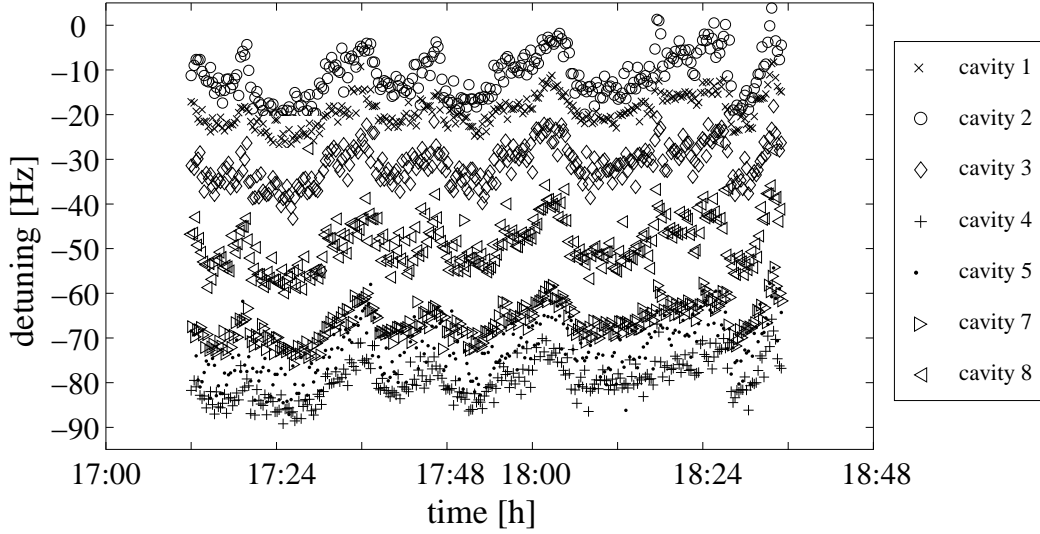


Figure 6.1: Long-term variation of the resonance frequency  $\omega_0$  of the cavities in the module. The variation of  $\omega_0$  is measured after the RF pulse has been turned off.

lium pressure has been measured only every eight minutes. The measured peak-to-peak variations have been below 0.25 mbar. The detuning of the cavity drifts on a time scale of several minutes indicated by the different intervals in Figure 6.2. Based on the assumption that tuner control compensates these slow drifts in the time intervals, only the detuning variation to a interpolated straight line is calculated. The result is plotted in Figure 6.3. The distributions have a Gaussian shape. If there was a dominant frequency in the microphonic spectrum, the most likely resonance frequency of the cavity would be at the limits of the microphonics range. The probability density has its maximum at the turning points of the oscillation. This is illustrated in Figure 6.4.

Measurements in the horizontal cavity test stand have shown similar results. Am-

cavity no.	$\sigma_{\Delta f}$ (rms)	cavity no.	$\sigma_{\Delta f}$ (rms)
1	4 Hz	5	9 Hz
2	5.5 Hz	7	4.5 Hz
3	5 Hz	8	6.5 Hz
4	7 Hz		

Table 6.1: The rms errors of the microphonic noise levels of the cavities in the TTF cryomodule.

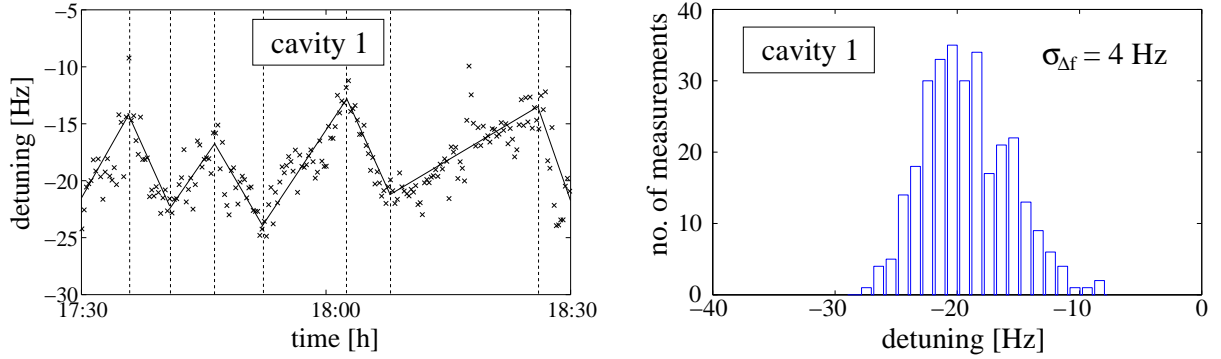


Figure 6.2: Variation of the detuning of a single cavity in the cryomodule.  
left diagram: The solid line indicates the assumed frequency correction by a mechanical tuner. The residual microphonics is calculated with respect to this line.  
right diagram: The resonance frequency spread is plotted to demonstrate the resonance frequency variation shown in the left diagram. The mechanical tuner has been in a fixed position, i.e. no tuner control has been applied.

plitude and phase of a nine-cell cavity were controlled by the digital RF system. The resonance frequency variation due to microphonics was 11 Hz (rms).

In chapter 3.3 it has been shown that in the case of TESLA and a beam current of  $I_{b0} = 8 \text{ mA}$  and accelerating gradients of 25 MV/m (loaded  $Q_L = 3 \cdot 10^6$ ), the required generator power per meter of acceleration length is given by

$$P_g = 50kW \cdot \left( 4 + \left( \frac{\Delta f}{f_{1/2}} \right)^2 \right)$$

The TTF RF system has been designed to cope with microphonics noise levels of approximately  $\pm 50 \text{ Hz}$ . Lorentz forces contribute to a detuning of  $\pm 200 \text{ Hz}$  [CDR 500] with optimum predetuning. This results in a maximum total detuning  $\Delta f$  of 250 Hz. The required extra RF power in this case is 30%. Assuming a maximum detuning of  $\pm 20 \text{ Hz}$  due to microphonics, this margin is reduced to 26%. It has been demonstrated that it is possible to keep the microphonic noise level below 10 Hz (rms) provided that the helium pressure variations are sufficiently small. Even without mechanical tuner control can the RF control system fulfill the requirements for the TESLA Test Facility with regard to amplitude and phase stability. If these conditions can be achieved for TESLA 500 operating at gradients of 25 MV/m, the question arises whether it is really necessary for mechanical tuners to compensate the resonance frequency variations on a time scale of several minutes.

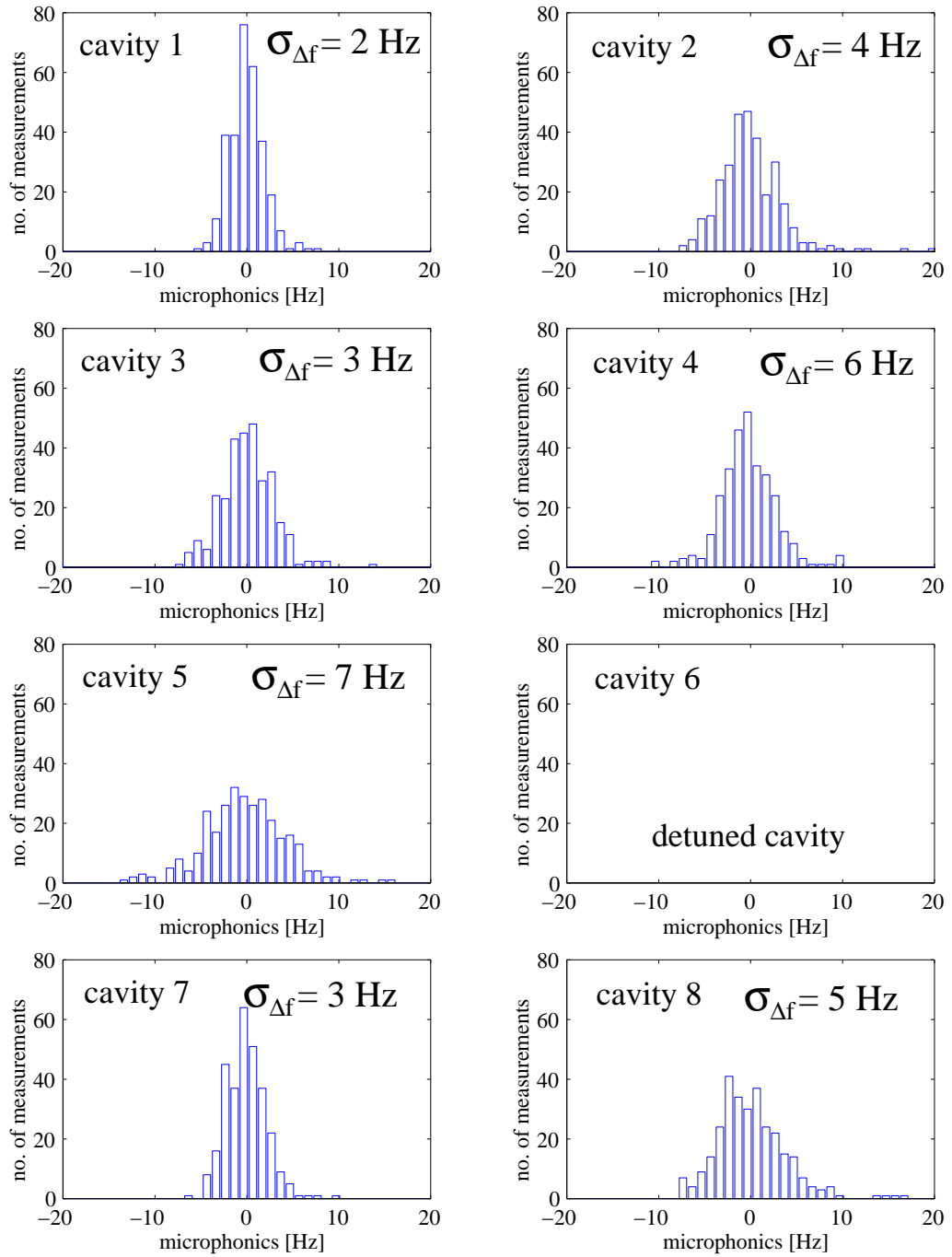


Figure 6.3: Microphonics in the TTF module. The change in resonance frequency due to slow helium pressure variations can in principle be compensated by the use of the mechanical frequency tuner with a control bandwidth of  $< 1$  Hz. In the first weeks of operation, the individual tuners of the cavities were in a fixed position. These plots demonstrate the microphonics of the cavities as it would exist if tuner control were applied.

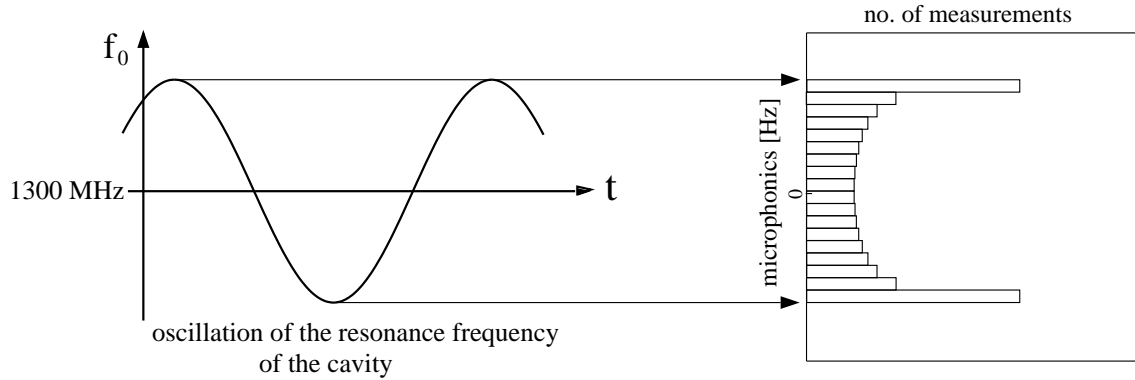


Figure 6.4: Expected microphonic spectrum if the cavity oscillates on a mechanical resonance.

## 6.2 Lorentz Force Detuning

In this section, the influence of high accelerating fields on the resonance frequency in superconducting cavities is discussed. The static detuning of a resonator due to the action of Lorentz forces is proportional to the square of the accelerating field (see chapter 3.4, equation (3.53)).

$$\Delta f_0 = (f_0)_2 - (f_0)_1 = -K \cdot E_{acc}^2 \quad (6.1)$$

This relation has been verified several times in continuous-wave operation. To determine the Lorentz force constant of TESLA cavities, two different types of measurements have been performed. The result is shown in Figure 6.5. In the left diagram, the cavity has been phase locked on resonance. The shift of the resonance frequency is plotted versus the square of the accelerating field. The result shown in the right diagram has been obtained by operating the cavity with constant RF input power and measuring the gradient at various frequencies. Due to Lorentz force detuning, the resonance curve is tilted. It is not possible to measure the unstable range below the bent curve. Starting with a frequency above resonance, the frequency has been reduced in steps. The field in the cavity reaches the maximum and then immediately returns to the lower branch of the gradient curve. Starting below the resonance frequency and increasing the RF frequency leads to a gradient following the Lorentz curve to the turning point where the resonance frequency drops again with increasing gradient. There, a jump to the upper branch occurs. Fitting a tilted Lorentz curve to the measured data results in a Lorentz force constant of  $K=0.9 \text{ Hz}/(\text{MV}/\text{m})^2$ . The two measurements have been performed with two different cavities. The results are very close to the computed value of  $K = 1 \text{ Hz}/(\text{MV}/\text{m})^2$ .

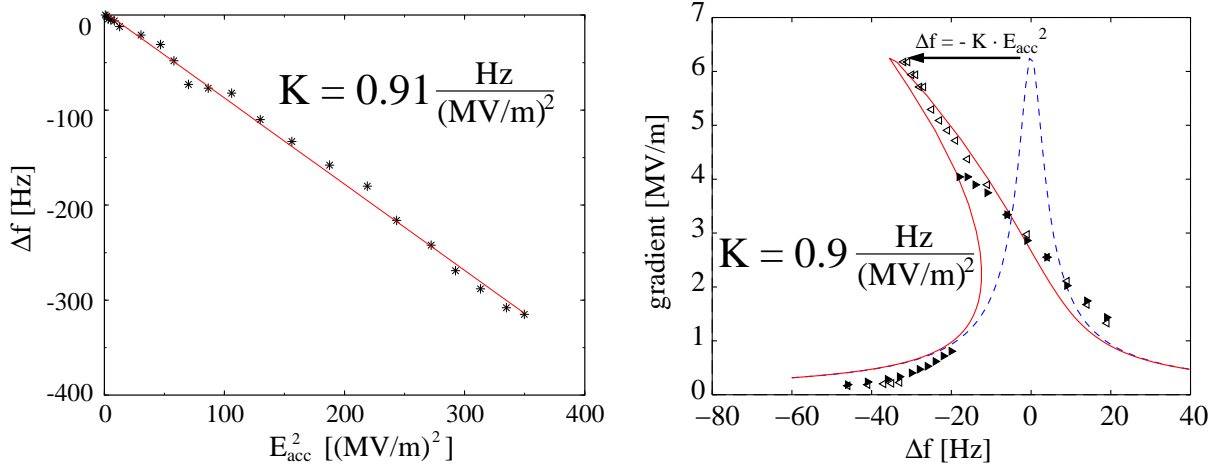


Figure 6.5: Static Lorentz force detuning.

Left diagram: Measurement of Lorentz force parameter  $K$ .

Right diagram: Resonance curve of a superconducting cavity with Lorentz force detuning. The dotted curve is an ideal Lorentz curve. Depending on the gradient, the cavity resonance frequency is shifted in proportion to the square of the accelerating field  $E_{acc}$ . The measured points are indicated with triangles.

However, in the linac of the TESLA Test Facility, the 9-cell cavities are operated in pulsed mode. The maximum pulse repetition rate is 10 Hz i.e. there is a 100 ms time difference between the pulses. The cavity time constant  $\tau$  is in the order of 300 to 700  $\mu$ s depending on the loaded  $Q_L$ . As a consequence, the cavity field at the beginning of each pulse is zero. Filling a cavity with RF power results in an increase of the electric field  $E_{acc}$  and hence to detuning due to Lorentz forces. On account of the inertia of the cavity walls, the shift of the resonance frequency does not immediately follow the quadratic dependence of the field which is only valid for steady-state conditions. The resonance frequency changes with a dynamic behavior. Measurements carried out with a different type of a superconducting cavity in pulsed mode (MACSE cavity, [Mos 93]) have shown that the dynamics can be described by a first-order differential equation (see chapter 3.4).

$$\begin{aligned} \tau_m \cdot \Delta\dot{\omega}(t) &= -(\Delta\omega(t) - \Delta\omega_T) - 2\pi K \cdot E_{acc}^2(t) \\ \Delta\omega(t) &= \omega_0(t) - \omega \end{aligned} \quad (6.2)$$

Simulations carried out for the TESLA cavity resulted in a mechanical time constant of  $\tau_m$  of 1 ms. To examine this description, the time dependence of the resonance frequency has been measured during an RF pulse. For this purpose, a single cavity was regulated with regard to amplitude and phase by the digital RF control system. As described in chapter 4.4, the resonance frequency of a cavity can be determined immediately after turning off

the RF power. The setpoint of the amplitude of the cavity has been set to the curve shown in Figure 6.6. The feedback system forced the cavity field to rise exponentially with the

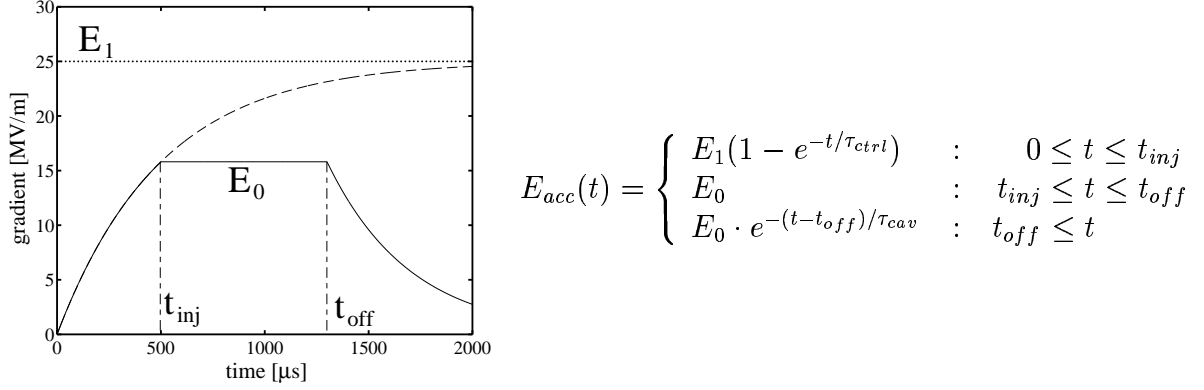


Figure 6.6: Accelerating field for Lorentz force detuning measurement. The amplitude setpoint of a single cavity is set to the time dependence shown.

time constant  $\tau_{ctrl}$  and independently of the cavity time constant  $\tau_{cav}$ . After 500  $\mu\text{s}$ , the field is kept constant at  $E_0$  (flattop) for 800  $\mu\text{s}$ . The field decay follows an exponential curve with the cavity time constant  $\tau_{cav}$ . The resonance frequency has been measured by turning off the klystron from macro pulse-to-macro pulse at different times within the pulse. Microphonics modulates the resonance frequency, which is why the klystron pulse length has been kept constant over several pulses in order to obtain sufficient statistical values for the calculation of the mean value of the resonance frequency. The mean value is plotted versus time in Figure 6.7. The accuracy of the detuning measurement is better than  $\pm 3$  Hz if the cavity field is above 1 MV/m. The analytical solution of the first-order differential equation (6.2) for the applied accelerating field  $E_{acc}(t)$  is given in appendix A.8. The result of the numerical fit of the measured data is plotted as solid lines in the Figure 6.7. The fit parameters for the individual cavities are the Lorentz force constant  $K$ , the mechanical time constant  $\tau_m$  and the initial pre-detuning  $\Delta\omega_T$ . The cavity time constants  $\tau_{cav}$  have been determined experimentally from the exponential field decay. The analytical solution shows that the Lorentz force constant  $K$  always appears as a product with the cavity field  $E_0$  or  $E_1$  (see Figure 6.6). The cavity gradients have not been calibrated precisely enough, which is why the values of the individual  $K$  cannot be determined by this fit procedure. The mechanical time constants  $\tau_m$  are between 130 and 400  $\mu\text{s}$ . The best fits of the seven cavities are those of cavity 1, 5 and 7 whose mechanical time constants are between 300  $\mu\text{s}$  and 400  $\mu\text{s}$ . The gradients in the cavities have been different during the measurements of the detuning. The range has been between 8 MV/m (cavity 8) and 15 MV/m (cavity 4). This results in different absolute detunings within the 1300  $\mu\text{s}$  RF pulse as seen in Figure 6.7.

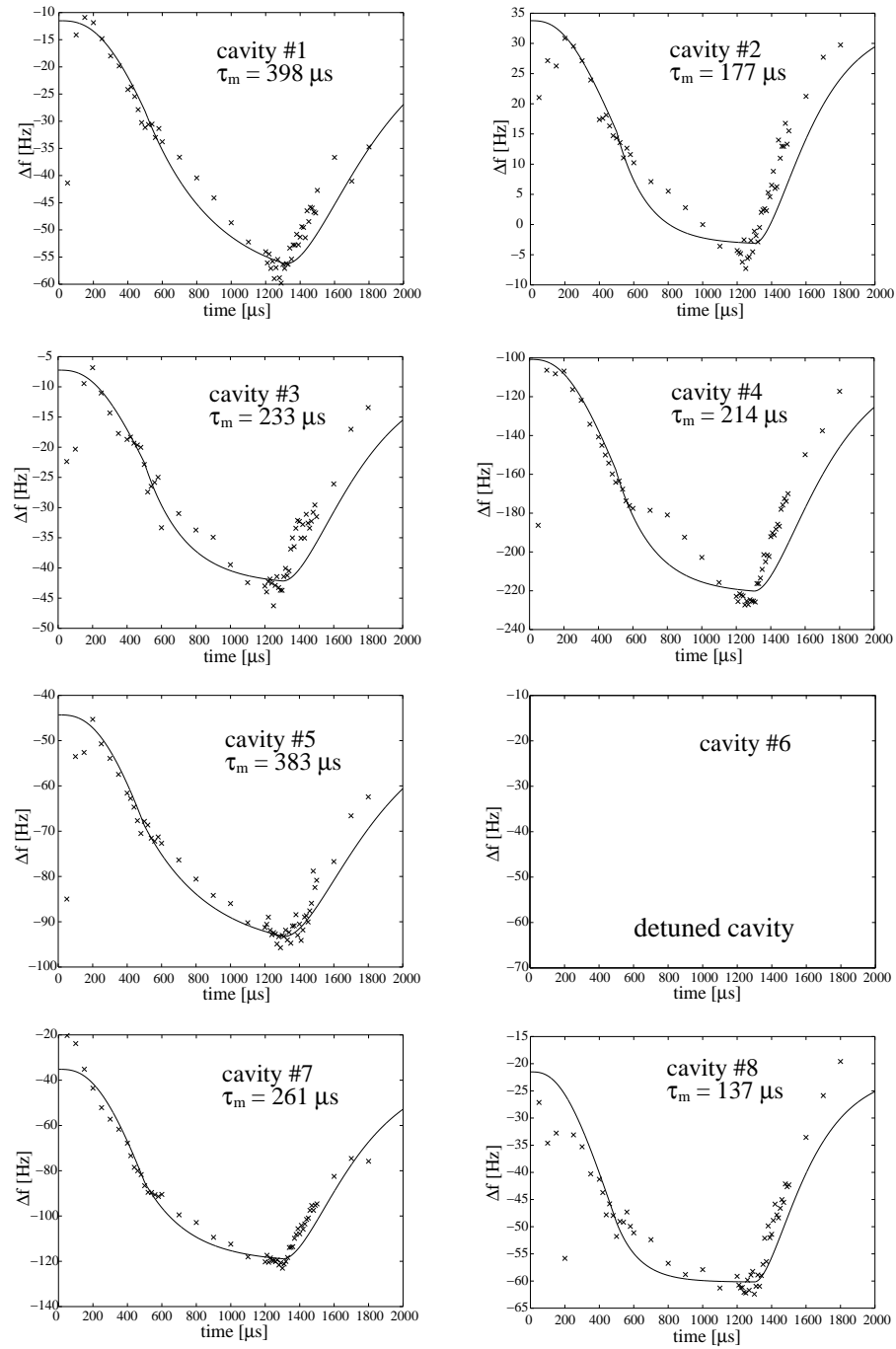


Figure 6.7: Cavity detuning during a macro pulse due to Lorentz forces. The crosses mark the mean value of the measured detunings while the solid line is the fit of the analytical solution of the first-order differential equation.

The first-order differential equation is able to describe the dynamics of the detuning  $\Delta\omega(t)$  qualitatively. However, all the cavities show a steeper return to the initial pre-detuning during the field decay (after 1300  $\mu\text{s}$ ) than the fit could explain. The resonance frequency still changes during the flattop condition between 500  $\mu\text{s}$  and 1300  $\mu\text{s}$ , which is equivalent to a continuing dynamic behavior. The steady-state condition, in which detuning is proportional to the square of the accelerating field, is not yet reached after 1300  $\mu\text{s}$ . Since the first-order model cannot describe the dynamics precisely, the question remains whether an approach with a higher-order differential equation could solve this problem. Even if the description made on the basis of the first-order differential equation is used, it still has to be clarified whether the mechanical time constant  $\tau_m$  is dependent on the gradient. This has to be investigated with the help of cavities which are able to reach higher gradients than 20 MV/m since the effect of Lorentz force detuning increases quadratically and therefore provides higher precision in determining the parameters  $\tau_m$  and  $K$ . Different approaches in the description of Lorentz force detuning are given in [Hün 98].

Assuming that the description of the detuning by a first-order differential equation with a gradient independent time constant  $\tau_m$  (which is in the order of 400  $\mu\text{s}$ ) is appropriate the consequences for the operation at 25 MV/m would be remarkable. The dynamic behavior of the resonance frequency of a cavity with the mechanical parameters  $\tau_m = 400 \mu\text{s}$  and  $K = 0.9 \text{ Hz}/(\text{MV}/\text{m})^2$  is plotted in Figure 6.8. The resonance frequency change

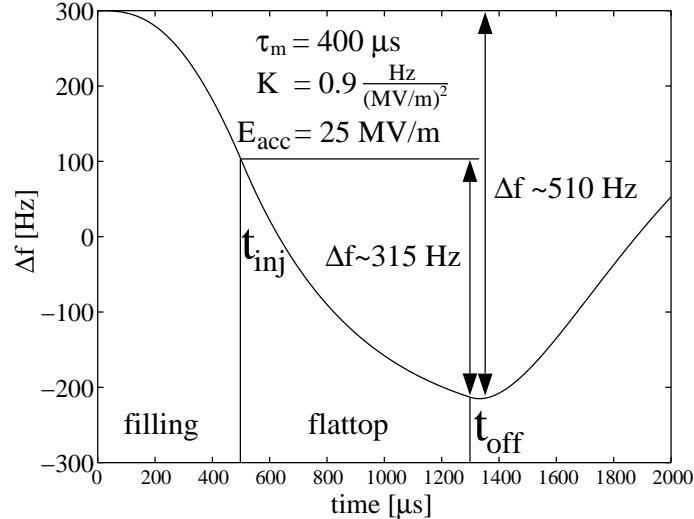


Figure 6.8: Theoretical Lorentz force detuning of a cavity operated at 25 MV/m. The cavity filling time is 500  $\mu\text{s}$  and flattop up to 1300  $\mu\text{s}$ . The mechanical parameters are  $\tau_m = 400 \mu\text{s}$  and  $K = 0.9 \text{ Hz}/(\text{MV}/\text{m})^2$ .

in this model during flattop is approximately 315 Hz, the total change is 510 Hz. This is

100 Hz more than the expected 400 Hz at this gradient and time structure. Calculating the required klystron power for the steady-state condition (equation (3.46) ) which can be assumed during flattop provides us with the power versus detuning shown in Figure 6.9. With an initial pre-detuning of +300 Hz (i.e. the resonance frequency is 300 Hz

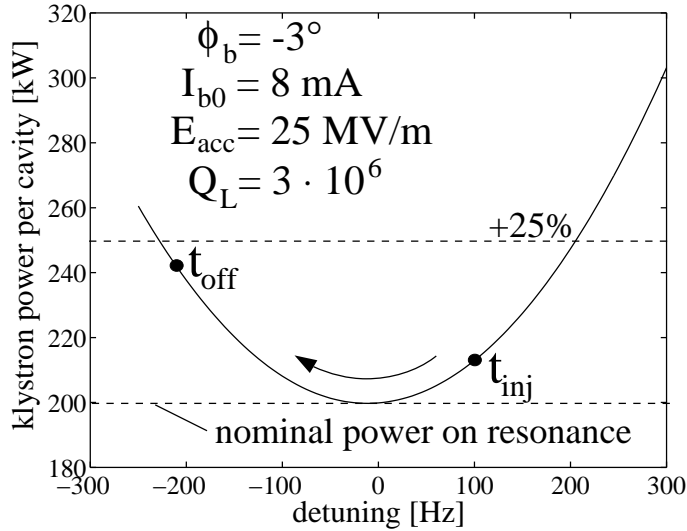


Figure 6.9: Required klystron power per cavity for a TESLA 9-cell cavity operated at design conditions (beam current: 8 mA;  $E_{acc} = 25$  MV/m;  $Q_L = 3 \cdot 10^6$ ; beam phase  $\phi_b = -3^\circ$ ) as a function of detuning. The curve is calculated for steady-state which can be assumed during flattop.

above the operating frequency of 1.3 GHz), it is possible to keep the required extra power due to Lorentz force detuning below 25% during flattop. However, further studies have to be carried out to find the optimum filling time and curve on which the cavities have to be filled in order to stay below the given power margin of 30% for amplitude and phase control.

### 6.3 Mechanical Resonances of the Cavity

Theoretical calculations of the vibrational mode spectrum have been made with finite element codes [Mar 93]. The spectrum has been calculated for three different configurations: the bare 9-cell structure (without stiffening rings), the stiffened structure and the stiffened, constrained structure. The effect of the helium vessel has not been taken into account. The result of these calculations are eight transversal and four longitudinal modes in the frequency range below 1000 Hz. These frequencies are quoted in Table 6.2 (first column). These frequencies are calculated for the cavity without HOM and input couplers.

During the operation of the linac, no strong excitation of mechanical resonances has been observed. This has been concluded from the results of the microphonic measurements shown in Figure 6.3 and 6.4. Additionally, experiments have been performed to excite mechanical resonances by the Lorentz force itself. The experimental setup is sketched in Figure 6.10. The cavity has been operated in continuous-wave mode at a gradient of

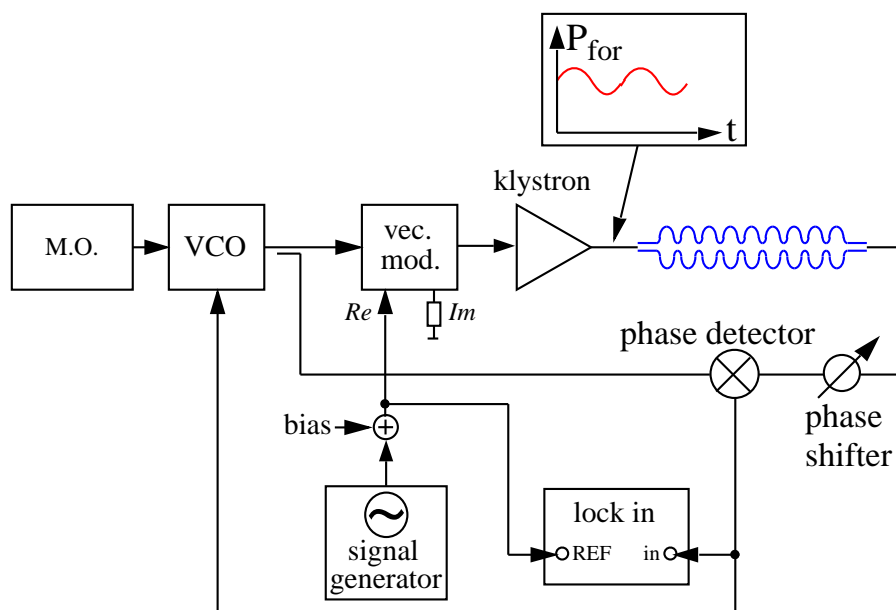


Figure 6.10: Experimental setup for mechanical excitation by Lorentz force.

7 MV/m with a loaded  $Q_L$  of  $1 \cdot 10^8$  and phase locked on resonance by controlling the detuning angle (phase between incident and field probe signal) to zero. A signal generator together with a bias voltage provided an amplitude-modulated low frequency signal ( $f < 4000$  Hz) at the input of a vector modulator. Modulation of the incident wave results in a modulation of the gradient in the cavity. This variation of the gradient corresponds to differently powerful Lorentz forces and hence to a modulation of the resonance frequency of the cavity ( $\Delta f_0 = -K \cdot E_{acc}^2$ ). The sweep of the excitation frequency has been performed with a signal generator. If the excitation frequency agrees with a mechanical resonance, the phase control signal would be enhanced by the quality factor of this resonance. The spectrum of the phase control signal has been scanned with a lock-in amplifier. The same measurement has been carried out at TJNAL with a 5-cell cavity (1497 MHz) at an operating temperature of 2.0 K. These cavities are not stiffened by stiffening rings and they have a Lorentz force detuning constant of  $K = 3 \text{ Hz}/(\text{MV}/\text{m})^2$ . They show two closely spaced mechanical resonances at about 66.3 and 64.7 Hz with mechanical quality factors of several hundreds [Doo/Sim]. The measurement performed with a TESLA 9-cell cavity has not revealed any significant enhancement of vibrational amplitudes.

Another approach adopted to determine mechanical resonance frequencies has been the measurement of mechanical vibrations of a constrained TESLA cavity at room temperature. For this purpose, a cavity was mounted onto a rigid aluminium support. The end flanges were fixed on the support to simulate the constraint by the helium vessel. Although this fixture differs from the actual one, in which the cavity is welded into the helium tank and mounted with a mechanical tuner, it gives an indication of the number and location of the resonances in the frequency spectrum. The excitation of the cavity was performed with sound waves coming from a loudspeaker. As a vibrational sensor, a piezoelectric crystal was used in combination with a lock-in amplifier which drove the loudspeaker. The aim of this measurement has been to detect the frequencies of mechanical resonances rather than to determine the resonance amplitude. Vibrations of the ground and of the aluminium support were measured first. Resonances at these frequencies were regarded as external vibrations which are not related to a cavity resonance frequency. Several resonances were found. Table 6.2 lists the detected mechanical resonance frequencies (second column). The strongest detected one is around 175 Hz. The amplitude of this resonance is shown in Figure 6.11. The corresponding phase curve in the same Figure shows the inverse tangens function as expected for a mechanical resonance. The quality factor of this resonance has been determined to be  $Q_m = 115$ . All other resonances have quality factors in the same order of about 100 or less. It has not been possible to identify the measured resonances with the theoretical calculations. However, the measurement has shown that the theoretically calculated number of resonances is in the range of the observed resonances. Until now, mechanical resonances have not been excited extensively during the operation of the linac.

calculated vibrational modes [Mar 93] (constrained)	mechanical modes of the constrained cavity (at room temperature)
70.9 (T)	96 Hz
181 (T)	175 Hz
234 (L)	239 Hz
322 (T)	281 Hz
465 (L)	325 Hz
474 (T)	353 Hz
621 (T)	381 Hz
693 (L)	486 Hz
748 (T)	507 Hz
844 (T)	565 Hz
900 (T)	696 Hz
915 (L)	764 Hz
	860 Hz
	1010 Hz
	1158 Hz
	2075 Hz
	2698 Hz
	2725 Hz
	2751 Hz

Table 6.2: Calculated and measured mechanical resonance frequencies. Left column: calculated vibrational modes of the constrained 9-cell cavity without HOM and input coupler. (T) stands for transversal vibrational modes, (L) for longitudinal modes. Right column : mechanical modes of the constrained 9-cell cavity at room temperature. The constraint imposed by the helium tank has been simulated by means of fixing the cavity to the aluminium support at the end flanges.

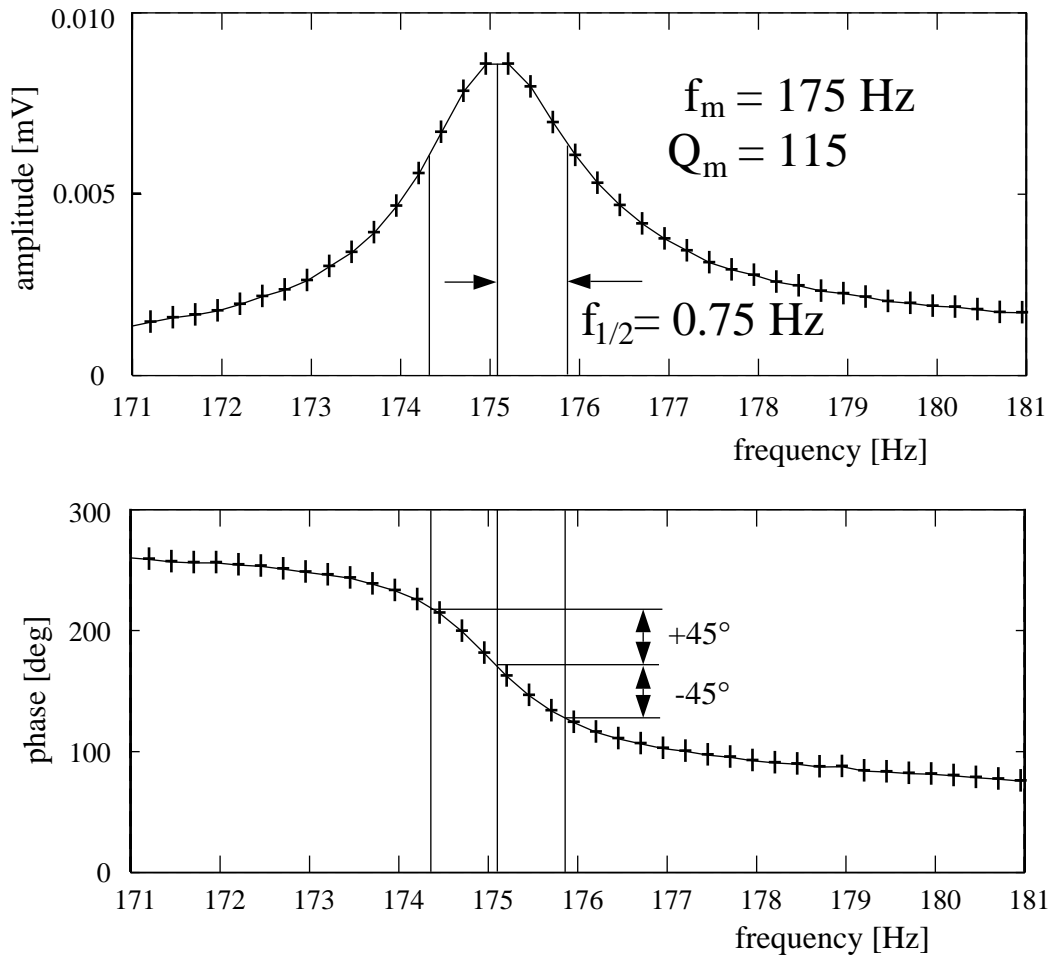


Figure 6.11: Mechanical resonance of a TESLA cavity. The measured values are indicated by crosses which are connected by a solid line.  
 Diagram above: Lorentz curve of the mechanical resonance curve. The amplitude is plotted versus the excitation frequency.  
 Diagram below: Phase curve of the mechanical resonance curve. The phase between measured control signal and excitation signal shows an inverse tangens function.

# Chapter 7

## Conclusion and Outlook

In this thesis, a digital RF control system has been developed to control the vector sum of the accelerating field of eight superconducting 9-cell cavities powered by a single klystron. It is the prototype for a possible RF feedback system for the TESLA 500 linear collider. The RF control system is implemented as a driven feedback system and has been installed at the TESLA Test Facility at DESY (Hamburg, Germany). The challenge that the design and development of an RF control system poses is to cope with disturbances which result from the pulsed operation of superconducting cavities, especially the detuning caused by the action of Lorentz forces. The objective of providing a constant accelerating field in order to minimize the energy spread was successfully reached within a few hours after turning the system on for the first time. This is mainly due to the extensive build-in diagnostics of the digital system, which provides access to the state of each cavity field during the RF macro pulse. Gradient and phase are measured as a function of time in each cavity. A sampling rate of 1 MHz has been chosen to guarantee a sufficiently fast response to disturbances. The main errors have been expected to come from microphonic noise and Lorentz force detuning. During the first run, it turned out that the microphonic noise level had been below 10 Hz (rms), which corresponds to a phase error of less than  $\pm 2^\circ$  in cavities with a loaded  $Q_L$  of  $1.8 \cdot 10^6$ . The eight superconducting cavities in the first cryomodule of the TESLA Test Facility were operated at an average gradient of up to 16.7 MV/m resulting in electron beam energies above 120 MeV. In addition to the feedback control system, an adaptive feed forward scheme has been applied to suppress repetitive errors. Since statistical perturbations (e.g. microphonics) of the accelerating field were on the  $10^{-4}$  level, adaptive feed forward stabilized the amplitude of the accelerating field to  $5 \cdot 10^{-4}$  (rms) and the phase of the RF field with respect to the beam to a value better than  $0.05^\circ$  (rms). The achieved stability is better than that required for the TESLA Test Facility by a factor of 10. This performance was reached with a beam pulse length of 30  $\mu\text{s}$  and has to be verified for the design beam pulse length of 800  $\mu\text{s}$ .

Studies of the mechanical properties of the TESLA 9-cell cavities have shown that the transfer of external vibrations to the cavities is well below the maximum tolerable value of  $\pm 50$  Hz for which the RF control system and the klystron with its power margin of 25% have been designed. Investigations of the dynamic behavior of the resonance

frequency  $\omega_0(t)$  of cavities under the influence of strong Lorentz forces have pointed out the qualitatively good agreement between the measured data and the description by a first-order differential equation. However, this model cannot explain the fast return of the resonance frequency to the initial pre-detuning after turning off the RF power. Further measurements have to be performed to provide an answer to this question in more detail.

In a next step, the digital RF control system has to prove that it is capable of fulfilling the requirements with regard to amplitude and phase stability when the control of the vector sum of the present eight cavities has to be extended to 24 cavities. In this, the field stability of the first eight cavities has to be studied within the control section of 24 cavities. This is important because a bunch compressor will be installed after the first cryomodule which requires a tight phase stability of the accelerating field of the first cryomodule. The design of the fully digital system provides high potential for more sophisticated control algorithms which can be implemented in future. This includes Smith predictors to compensate for delay times in the control loop, Kalman filtering, which provides the best reconstruction of the state of a system in the presence of statistical noise, and state estimators, which estimate the full state based on the measurements of only a part of the states. Moreover, the extensive access to information about the state of the individual cavities during an RF pulse allows system identification. Based on this design, many RF control-related procedures can be automated similar to the automated loop phase adjustment already installed. As the objective is an RF control system for TESLA 500 with nearly 20000 cavities, automatisisation has to be extended to include tuner control (mechanical stepper motor), RF exception handling, which guides the operator in recovering the system in the case of RF failures, quench detection of a cavity within a control section, etc. The operation of the TESLA Test Facility with its planned eight cryomodules will permit more experience to be gained with regard to the implementations required for the operation of a large  $e^+e^-$ -collider.

# Appendix A

## Appendix

### A.1 Effective Accelerating Voltage of an RF Cavity

In computing the energy gain of a particle passing through a cavity filled with RF, the electromagnetic fields varying in space and time have to be taken into account. The accelerating voltage  $V_{acc}$  seen by the particle after the passage is defined as the energy gain divided by the charge of the particle. In the following, only the special case of the  $\pi$ -accelerating mode in a standing wave structure and a relativistic beam ( $v \approx c$ ) are discussed. The accelerating field on axis is written as

$$E_z(z, t) = E(z) \cdot \cos(\omega t)$$

where  $\omega = 2\pi f$  is the frequency of the RF. We choose the coordinate system as shown in Fig. A.1. The time axes is choosen in such a way that the particle passes the origin

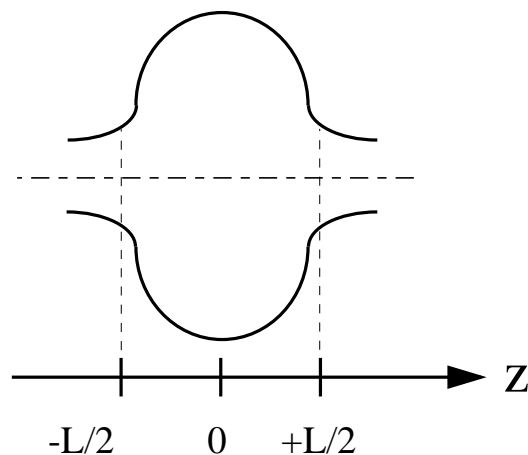


Figure A.1: Coordinate system of an RF cavity

(center of cavity) at time  $t = 0$ . Therefore,

$$z = c \cdot t$$

In this case the accelerating voltage is

$$V_c = \int_{-L/2}^{+L/2} E(z) \cdot \cos\left(\frac{\omega}{c}z\right) dz \quad (\text{A.1})$$

If the particle injection is delayed by a time  $t_b$  then

$$z = c \cdot (t - t_b) \quad \Longleftrightarrow \quad t = \frac{z}{c} + t_b$$

which means the particle reaches the center of the cavity at the delayed time  $t_b$ . If we look at the co-moving frame which moves along with the particle, the electrical field  $E_p$  seen by the particle is given by

$$\begin{aligned} E_p(z, t(z)) &= E_p(z) = E(z) \cdot \cos\left(\omega \cdot \left(\frac{z}{c} + t_b\right)\right) \\ &= E(z) \cdot \left( \cos\left(\frac{\omega}{c}z\right) \cdot \cos(\omega t_b) - \sin\left(\frac{\omega}{c}z\right) \cdot \sin(\omega t_b) \right) \end{aligned}$$

Defining  $\varphi = \omega t_b$  as the phase due to the delay, the accelerating voltage which acts on the particle is

$$\begin{aligned} V_{acc}(t_b) &= \int_{-L/2}^{+L/2} E_p(z) dz \\ &= \cos \varphi \cdot \int_{-L/2}^{+L/2} E(z) \cdot \cos\left(\frac{\omega}{c}z\right) dz - \sin \varphi \cdot \int_{-L/2}^{+L/2} E(z) \cdot \sin\left(\frac{\omega}{c}z\right) dz \quad (\text{A.2}) \end{aligned}$$

For symmetric field distribution  $E(z) = E(-z)$ , the second integral in eq. (A.2) vanishes. The first integral is defined as the maximum accelerating voltage of the cavity  $V_c$ . With equation (A.1), the dependence of the accelerating voltage of delay time  $t_b$  is

$$V_{acc}(t_b) = V_c \cdot \cos \varphi = V_c \cdot \cos(\omega t_b) \quad (\text{A.3})$$

Fig. A.2 shows the accelerating voltage versus phase  $\varphi = \omega t_b$ . Injection with no delay is called *injection on crest* (point (1) in Fig. A.2). This means that a particle reaches the center of the cavity when  $E(z, t)$  is at its maximum. A delay by a quarter of an RF period ( $\varphi = \frac{\pi}{2}$ ) is *injection at zero crossing* (point (2) in Fig. A.2) and point (3) *180° out of phase* which means deceleration of the particle.

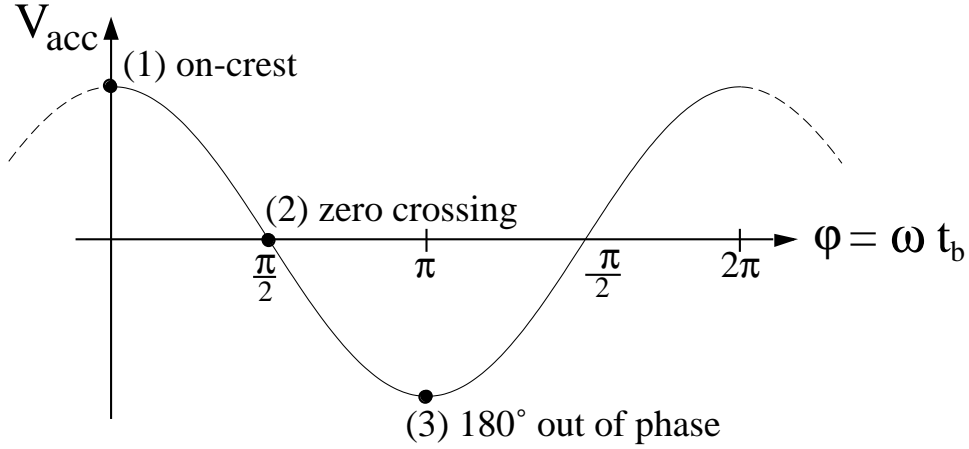


Figure A.2: Dependence of accelerating voltage versus injection phase  $\varphi$

## A.2 Amplitude and Phase of an LCR circuit

The individual impedances in an LCR circuit are

$$Z_L = i\omega L \quad ; \quad Z_R = R \quad ; \quad Z_C = \frac{1}{i\omega C}$$

The total impedance is therefore

$$Z_{tot} = \frac{1}{\frac{1}{R} + \frac{1}{i\omega L} + i\omega C} = \frac{R}{1 - iR\left(\frac{1}{\omega L} - \omega C\right)}$$

or with the quantities  $\omega_0$  and  $Q_0$

$$Z_{tot} = \frac{R}{1 - iQ_0\left(\frac{\omega_0}{\omega} - \frac{\omega}{\omega_0}\right)} \quad (\text{A.4})$$

A sinusoidal current  $I(t)$  results in a voltage  $V(t)$  according to

$$V(t) = Z_{tot} \cdot I(t) .$$

Since this is a multiplication in the complex plane, we get the same time dependence for  $V(t)$  but with a phase shift  $\psi$ .

$$V(t) = \hat{V} \cdot \sin(\omega t + \psi)$$

The absolute value of  $Z_{tot} = |Z_{tot}| \cdot e^{i\psi}$  is calculated to

$$|Z_{tot}| = \frac{R}{\sqrt{1 + Q_0^2 \left(\frac{\omega_0}{\omega} - \frac{\omega}{\omega_0}\right)^2}} \quad (\text{A.5})$$

and the phase  $\psi$  to

$$\tan \psi = Q_0 \left( \frac{\omega_0}{\omega} - \frac{\omega}{\omega_0} \right) \quad (\text{A.6})$$

The complex impedance  $Z_{tot}$  can therefore be expressed as

$$Z_{tot} = \frac{R}{1 - i \tan \psi} \quad (\text{A.7})$$

With  $\hat{V} = |Z_{tot}| \cdot \hat{I}_0$ , we end up with the same equations for phase  $\psi$  and amplitude  $\hat{V}$  as in equation (3.20) and (3.21).

### A.3 Lossless Transmission Line

The wave equations of a lossless transmission line for the voltage  $V$  and the current  $I$  is derived for a transmission line which consists of two conductors separated by a dielectric, e.g. a co-axial line. The analysis of a transmission line can be based on lumped-circuit elements where it is decomposed into elementary parts of length  $dx$ . Each elementary part consists of series inductance  $L'$  and a shunt capacitance  $C'$  per unit length (see Fig. A.3). Applying Kirchoff's rules and expanding the functions in first order we get

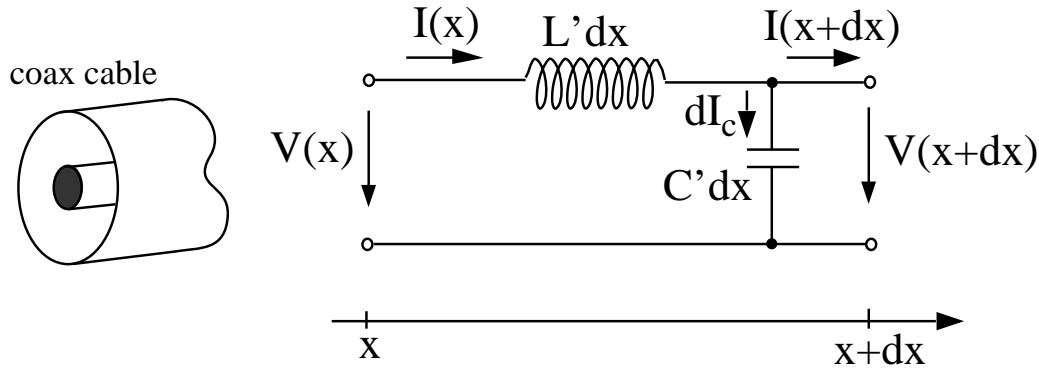


Figure A.3: Elementary equivalent circuit of a transmission line with series inductance  $L$  and shunt capacitance  $C$ .  $L'$  and  $C'$  are the inductance and capacitance per unit length respectively.

$$\begin{aligned} V(x + dx) &= V(x) + \frac{\partial V}{\partial x} dx = V(x) + dV \\ I(x + dx) &= I(x) + \frac{\partial I}{\partial x} dx = I(x) - dI_C \end{aligned}$$

The induced voltage is given by

$$\begin{aligned} dV &= \frac{\partial V}{\partial x} dx = dV_{ind} = -L' dx \cdot \frac{\partial I}{\partial t} \\ \Leftrightarrow \frac{\partial V(x, t)}{\partial x} &= -L' \cdot \frac{\partial I(x, t)}{\partial t} \end{aligned} \quad (\text{A.8})$$

The current through the capacitance can be written as

$$\begin{aligned} dI_c &= C'dx \cdot \frac{\partial V}{\partial t} = -\frac{\partial I}{\partial x}dx \\ \Leftrightarrow \frac{\partial I(x,t)}{\partial x} &= -C' \cdot \frac{\partial V(x,t)}{\partial t} \end{aligned} \quad (\text{A.9})$$

Differentiation of equation (A.8) with  $\frac{\partial}{\partial x}$ , equation (A.9) with  $\frac{\partial}{\partial t}$  and substitution of  $\frac{\partial I}{\partial x \partial t}$  yields

$$\frac{\partial^2 V}{\partial x^2} = L'C' \frac{\partial^2 V}{\partial t^2}. \quad (\text{A.10})$$

$$\frac{\partial^2 I}{\partial x^2} = L'C' \frac{\partial^2 I}{\partial t^2}. \quad (\text{A.11})$$

These two equations are wave equations of the transmission lines with phase velocity

$$v_{ph} = \frac{1}{\sqrt{L'C'}}. \quad (\text{A.12})$$

The general solution of the differential equation (A.10) and (A.11) are forward and backward travelling waves with amplitudes  $\hat{\mathbf{V}}_+$ ,  $\hat{\mathbf{V}}_-$ ,  $\hat{\mathbf{I}}_+$ ,  $\hat{\mathbf{I}}_-$ , respectively. These amplitudes are complex quantities (phasors) which contain an initial phase at  $t = 0$ . Complex voltages and currents are written in bold-face letters.

$$\mathbf{V}(x,t) = \hat{\mathbf{V}}_+ e^{i(\omega t - kx)} + \hat{\mathbf{V}}_- e^{i(\omega t + kx)} \quad (\text{A.13})$$

$$\mathbf{I}(x,t) = \hat{\mathbf{I}}_+ e^{i(\omega t - kx)} + \hat{\mathbf{I}}_- e^{i(\omega t + kx)} \quad (\text{A.14})$$

with wave number  $k = \frac{\omega}{v_{ph}} = \omega \sqrt{L'C'}$ . In order to derive the relation between  $(\hat{\mathbf{V}}_+, \hat{\mathbf{I}}_+)$  and  $(\hat{\mathbf{V}}_-, \hat{\mathbf{I}}_-)$ , the general solution (eq. (A.13) and (A.14)) has to be inserted in equations (A.8) and (A.9). Taking equation (A.8) we obtain

$$\begin{aligned} \frac{\partial \mathbf{V}}{\partial x} &= -ik \left( \hat{\mathbf{V}}_+ e^{i(\omega t - kx)} \right) + ik \left( \hat{\mathbf{V}}_- e^{i(\omega t + kx)} \right) \\ &\stackrel{!}{=} -L' \frac{\partial \mathbf{I}}{\partial t} = -L' \left( i\omega \left( \hat{\mathbf{I}}_+ e^{i(\omega t - kx)} \right) + i\omega \left( \hat{\mathbf{I}}_- e^{i(\omega t + kx)} \right) \right) \end{aligned}$$

$$\Leftrightarrow i \left( L'\omega \hat{\mathbf{I}}_+ - k \hat{\mathbf{V}}_+ \right) e^{i(\omega t - kx)} + i \left( L'\omega \hat{\mathbf{I}}_- + k \hat{\mathbf{V}}_- \right) e^{i(\omega t + kx)} = 0 \quad (\text{A.15})$$

This equation can only be fulfilled for all  $x$  and  $t$  if  $L'\omega \hat{\mathbf{I}}_+ = k \hat{\mathbf{V}}_+ = \omega \sqrt{L'C'} \hat{\mathbf{V}}_+$  and  $L'\omega \hat{\mathbf{I}}_- = -k \hat{\mathbf{V}}_- = -\omega \sqrt{L'C'} \hat{\mathbf{V}}_-$ . This yields

$$\hat{\mathbf{I}}_+ = \frac{\hat{\mathbf{V}}_+}{\sqrt{\frac{L'}{C'}}} \quad \text{and} \quad \hat{\mathbf{I}}_- = -\frac{\hat{\mathbf{V}}_-}{\sqrt{\frac{L'}{C'}}}. \quad (\text{A.16})$$

The quantity  $\sqrt{\frac{L'}{C'}}$  has the unit of an impedance and is defined as the characteristic impedance of the transmission line. It relates voltage and current of a travelling wave.

$$Z_0 := \sqrt{\frac{L'}{C'}} \quad (\text{A.17})$$

The general solution of the transmission line (eq. (A.13) and (A.14)) can therefore be written as

transmission line:

$$\mathbf{V}(x, t) = \mathbf{V}_{for}(x, t) + \mathbf{V}_{ref}(x, t) \quad (\text{A.18})$$

$$= \hat{\mathbf{V}}_+ e^{i(\omega t - kx)} + \hat{\mathbf{V}}_- e^{i(\omega t + kx)} \quad (\text{A.19})$$

$$\mathbf{I}(x, t) = \mathbf{I}_{for}(x, t) + \mathbf{I}_{ref}(x, t) \quad (\text{A.20})$$

$$= \frac{\hat{\mathbf{V}}_+}{Z_0} e^{i(\omega t - kx)} - \frac{\hat{\mathbf{V}}_-}{Z_0} e^{i(\omega t + kx)} \quad (\text{A.21})$$

with forward wave:

$$\mathbf{V}_{for}(x, t) = \hat{\mathbf{V}}_+ e^{i(\omega t - kx)} \quad (\text{A.22})$$

$$\mathbf{I}_{for}(x, t) = \frac{\hat{\mathbf{V}}_+}{Z_0} e^{i(\omega t - kx)} = \frac{\mathbf{V}_{for}(x, t)}{Z_0} \quad (\text{A.23})$$

and reflected wave:

$$\mathbf{V}_{ref}(x, t) = \hat{\mathbf{V}}_- e^{i(\omega t + kx)} \quad (\text{A.24})$$

$$\mathbf{I}_{ref}(x, t) = -\frac{\hat{\mathbf{V}}_-}{Z_0} e^{i(\omega t + kx)} = -\frac{\mathbf{V}_{ref}(x, t)}{Z_0} \quad (\text{A.25})$$

The minus sign in front of  $\mathbf{I}_{ref}$  indicates the counterflowing current while the voltages of forward and backward waves just add up.

## A.4 RF Component of a Bunched Beam Current

In the equivalent LCR circuit diagram of a cavity, the RF generator and the beam are represented as a current source. While the RF generator delivers an AC current with harmonic time dependence, the beam current has a pulsed structure. The beam current is nearly always given as an average DC current. Therefore, one has to take the Fourier component of the beam current at the same frequency as the RF generator with time dependence  $e^{i\omega t}$ . In the steady-state case we start with a beam structure shown in Figure A.4. A single bunch is described by a Gaussian curve with standard deviation  $\sigma_t$ .

$$I(t) = \frac{Q_0}{\sqrt{2\pi\sigma_t}} \cdot e^{-\frac{t^2}{2\sigma_t^2}} = I_{peak} \cdot e^{-\frac{t^2}{2\sigma_t^2}}$$

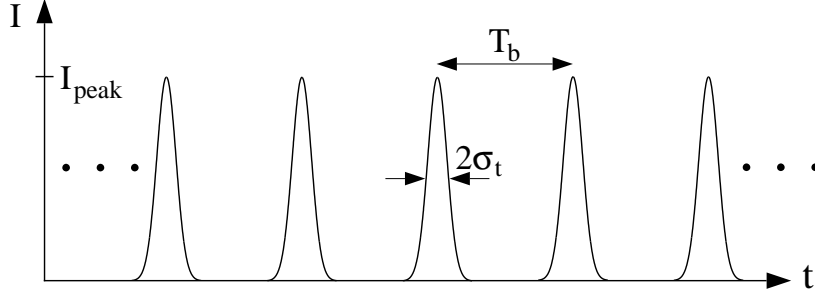


Figure A.4: Time-structure of a beam current with Gaussian-shaped bunches. The bunch spacing is  $T_b$  and the bunch width  $\sigma_t$ .

where  $Q_0$  is the total charge in a bunch. Fourier decomposition on the interval  $[-T_b/2; +T_b/2]$  gives

$$I(t) = \frac{a_0}{2} + \sum_{n=1}^{+\infty} (a_n \cos(n\omega_0 t) + b_n \sin(n\omega_0 t)) \quad (\text{A.26})$$

with

$$\begin{aligned} \omega_0 &= \frac{2\pi}{T} \\ a_n &= 2I_{peak} \sqrt{2\pi} \frac{\sigma_t}{T_b} \cdot e^{-n^2 \omega_0^2 \sigma_t^2 / 2} & n = 0, 1, 2, \dots \\ b_n &= 0 & n = 1, 2, 3, \dots \end{aligned}$$

With the definition

$$I_{b0} = I_{peak} \cdot \sqrt{2\pi} \frac{\sigma_t}{T_b} = \frac{Q_0}{T_b}$$

the Fourier spectrum of the beam current can be written as

$$a_n = 2 \cdot I_{b0} \cdot e^{-n^2 \omega_0^2 \sigma_t^2 / 2} .$$

For short bunches  $\sigma_t \ll T_b$ , the Fourier component at the operating frequency is simply

$$I_b = a_n(1300\text{MHz}) \approx 2 \cdot I_{b0} .$$

The DC component is equal to  $I_{b0}$  as seen in equation (A.26). The parameters for the TTF Injector II and TESLA 500 are shown in table A.1. The spectrum of the beam current of the TTF injector II is plotted in Figure A.5.

## A.5 Cavity Power Equation

To deduce the relation between the required generator power necessary to accelerate beam and the accelerating voltage  $V_{acc} = V_{cav} \cos \phi_b$  of the cavity, we start with the

	TTF Inj. II	TESLA 500
bunch charge $Q_0$	8.0 nC	5.8 nC
bunch length $\sigma_t$	3.3 ps	2.3 ps
peak current $I_{peak}$	958 A	993 A
average DC current $I_{b0}$	8.0 mA	8.2 mA

Table A.1: TTF/TESLA 500 beam parameter

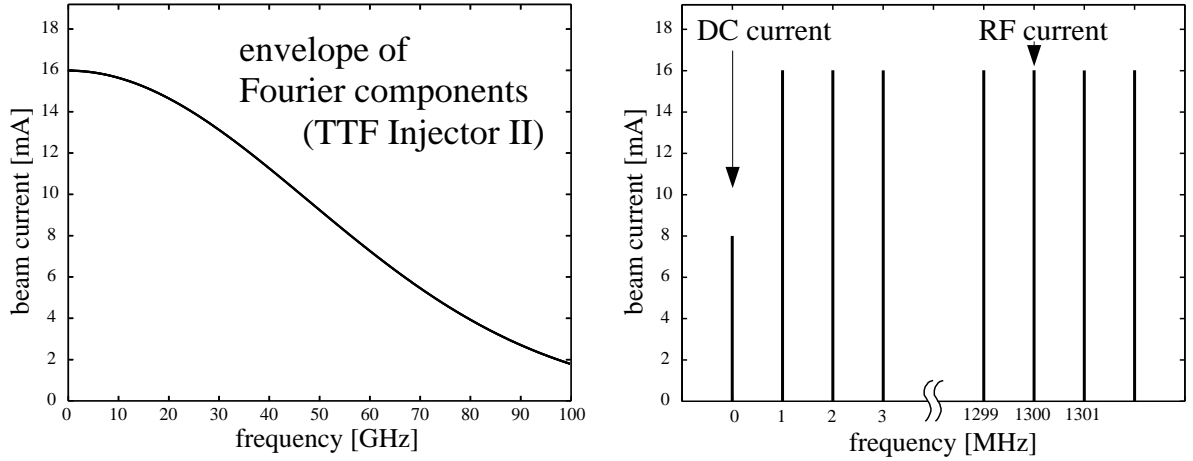


Figure A.5: Fourier spectrum of the TTF Injector II beam current with Gaussian-distributed single bunches. The left plot shows the envelope of the spectral components that are equally spaced at every 1 MHz. The right plot shows the DC component and the component at the operating frequency of 1.3 GHz.

vector diagram of Figure A.6. We only use the amplitudes of the complex quantities of the beam current  $\mathbf{I}_b$ , the cavity voltage  $\mathbf{V}_{cav}$ , the generator-induced voltage  $\mathbf{V}_g$  and the beam-induced voltage  $\mathbf{V}_b$ . From the vector diagram, we obtain the relations

$$\begin{aligned}
 V_{cav} &= V_g \cos(\psi - \Theta - \phi_b) - V_b \cos(\psi - \phi_b) \\
 0 &= V_g \sin(\psi - \Theta - \phi_b) - V_b \sin(\psi - \phi_b) .
 \end{aligned}$$

To eliminate the terms with the angle  $(\psi - \Theta - \phi_b)$ , we write

$$\begin{aligned}
 \Leftrightarrow \quad V_g \cos(\psi - \Theta - \phi_b) &= V_{cav} + V_b \cos(\psi - \phi_b) \\
 V_g \sin(\psi - \Theta - \phi_b) &= V_b \sin(\psi - \phi_b) .
 \end{aligned}$$

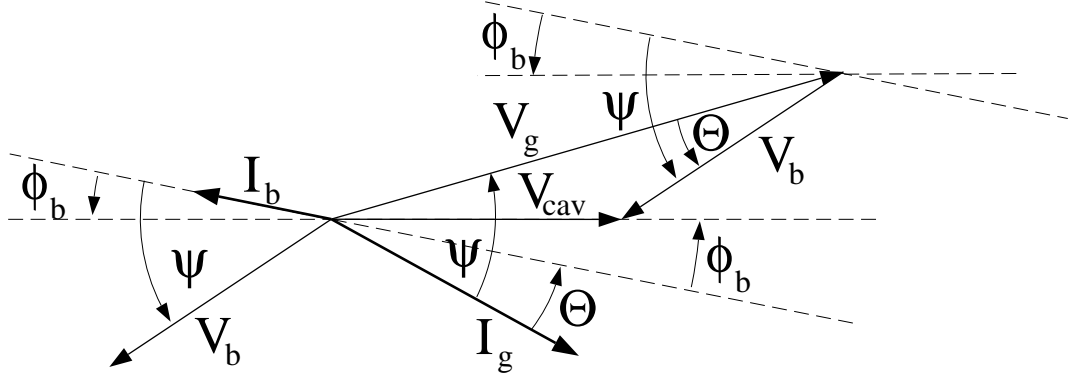


Figure A.6: Vector diagram of currents and voltages in the cavity due to beam and generator.

Taking the square of these two equations and adding them yields

$$\begin{aligned}
 V_g^2 &= (V_{cav} + V_b \cos(\psi - \phi_b))^2 + (V_b \sin(\psi - \phi_b))^2 \\
 V_g^2 &= V_{cav}^2 + 2V_{cav}V_b \cos(\psi - \phi_b) + V_b^2 \\
 V_g^2 &= (V_{cav} \cos \psi + V_b \cos \phi_b)^2 + (V_{cav} \sin \psi + V_b \sin \phi_b)^2 .
 \end{aligned}$$

Replacing the generator and beam voltage

$$\begin{aligned}
 \text{with } V_g &= V_{gr} \cos \psi & ; & \quad V_b = V_{br} \cos \psi \\
 V_{gr} &= \frac{2\beta}{\beta+1} \sqrt{\frac{2R_L P_g}{\beta}} = \sqrt{\frac{8\beta}{\beta+1} R_L P_g} & ; & \quad V_{br} = R_L I_b = 2R_L I_{b0}
 \end{aligned}$$

we obtain

$$\begin{aligned}
 \Rightarrow V_{gr}^2 \cos^2 \psi &= V_{cav}^2 \cos^2 \psi \left(1 + \frac{V_{br}}{V_{cav}} \cos \phi_b\right)^2 + V_{cav}^2 \cos^2 \psi \left(\tan \psi + \frac{V_{br}}{V_{cav}} \sin \phi_b\right)^2 \\
 \frac{8\beta}{\beta+1} R_L P_g &= V_{cav}^2 \left\{ \left(1 + \frac{2R_L I_{b0}}{V_{cav}} \cos \phi_b\right)^2 + \left(\tan \psi + \frac{2R_L I_{b0}}{V_{cav}} \sin \phi_b\right)^2 \right\} \\
 P_g &= \frac{V_{cav}^2 \beta+1}{R_L 8\beta} \left\{ \left(1 + \frac{2R_L I_{b0}}{V_{cav}} \cos \phi_b\right)^2 + \left(\tan \psi + \frac{2R_L I_{b0}}{V_{cav}} \sin \phi_b\right)^2 \right\} .
 \end{aligned}$$

In the special case of superconducting cavities, we can make the following approximation:

$$\text{for } \beta \gg 1 : \quad \tan \psi \approx 2Q_L \frac{\Delta\omega}{\omega} = 2Q_L \frac{\Delta f}{f} \quad (\text{equation (3.22)})$$

This yields:

$$\Rightarrow P_g \approx \frac{V_{cav}^2}{\left(\frac{r}{Q}\right) Q_L} \frac{1}{4} \left\{ \left(1 + \frac{\left(\frac{r}{Q}\right) Q_L I_{b0}}{V_{cav}} \cos \phi_b\right)^2 + \left(\frac{\Delta f}{f_{1/2}} + \frac{\left(\frac{r}{Q}\right) Q_L I_{b0}}{V_{cav}} \sin \phi_b\right)^2 \right\} \quad (\text{A.27})$$

with:

$$R_L = \frac{1}{2} \cdot \left(\frac{r}{Q}\right) \cdot Q_L \quad (\text{equation (3.2)})$$

## A.6 Cavity Differential Equation

A driven LCR circuit can be described in terms of the loaded  $Q_L$  by the differential equation (3.16)

$$\ddot{\mathbf{V}}(t) + \frac{\omega_0}{Q_L} \dot{\mathbf{V}}(t) + \omega_0^2 \mathbf{V}(t) = \frac{\omega_0 R_L}{Q_L} \dot{\mathbf{I}}(t).$$

If the driving current is harmonic with time dependence  $e^{i\omega t}$ , we separate the fast oscillations from the slow amplitude changes.

$$\begin{aligned} \mathbf{V}(t) &= (V_r(t) + iV_i(t)) \cdot e^{i\omega t} \\ \mathbf{I}(t) &= (I_r(t) + iI_i(t)) \cdot e^{i\omega t} \end{aligned}$$

Inserting this in the differential equation yields

$$\begin{aligned} (\ddot{V}_r + i\ddot{V}_i) + 2i\omega(\dot{V}_r + i\dot{V}_i) - \omega^2(V_r + iV_i) + \frac{\omega_0}{Q_L} ((\dot{V}_r + i\dot{V}_i) + i\omega(V_r + iV_i)) \\ + \omega_0^2(V_r + iV_i) = \frac{\omega_0 R_L}{Q_L} (\dot{I}_r + i\dot{I}_i) + i\frac{\omega_0 \omega R}{Q_L} (I_r + iI_i) \end{aligned}$$

Separating the differential equation in real and imaginary parts yields

$$\begin{aligned} \text{real:} \quad \ddot{V}_r + \frac{\omega_0}{Q_L} \dot{V}_r - 2\omega \dot{V}_i - \omega^2 V_r - \frac{\omega \omega_0}{Q_L} V_i + \omega_0^2 V_r &= \frac{\omega_0 R_L}{Q_L} \dot{I}_r - \frac{\omega_0 \omega R_L}{Q_L} I_i \\ \text{imag.:} \quad \ddot{V}_i + \frac{\omega_0}{Q_L} \dot{V}_i + 2\omega \dot{V}_r - \omega^2 V_i + \frac{\omega \omega_0}{Q_L} V_r + \omega_0^2 V_i &= \frac{\omega_0 R_L}{Q_L} \dot{I}_i + \frac{\omega_0 \omega R_L}{Q_L} I_r \end{aligned}$$

Multiplying the first equation with  $-\frac{1}{2\omega}$  and the second with  $\frac{1}{2\omega}$  gives

$$\begin{aligned} \frac{1}{2\omega} \ddot{V}_i + \frac{\omega_0}{\omega} \frac{1}{2Q_L} \dot{V}_i + \dot{V}_r + \frac{1}{2\omega} (\omega_0^2 - \omega^2) V_i + \frac{\omega_0}{2Q_L} V_r &= \frac{R_L}{2Q_L} \left( \frac{\omega_0}{\omega} \dot{I}_i + \omega_0 I_r \right) \\ -\frac{1}{2\omega} \ddot{V}_r - \frac{\omega_0}{\omega} \frac{1}{2Q_L} \dot{V}_r + \dot{V}_i - \frac{1}{2\omega} (\omega_0^2 - \omega^2) V_r + \frac{\omega_0}{2Q_L} V_i &= -\frac{R_L}{2Q_L} \left( \frac{\omega_0}{\omega} \dot{I}_r + \omega_0 I_i \right) \end{aligned}$$

The second-order terms can be neglected as they are small compared with the others. Furthermore, the resonance frequency is nearly equal to the RF frequency. Therefore, the following approximation can be made:

$$\frac{\omega_0}{\omega} \approx 1 ; \quad \frac{1}{2\omega} (\omega_0^2 - \omega^2) = \frac{\omega_0 - \omega}{2} \cdot \frac{\omega_0 + \omega}{\omega} \approx \omega_0 - \omega = \Delta\omega$$

We end up with two first-order differential equations for real and imaginary parts.

$$\begin{aligned}\dot{V}_r + \frac{1}{2Q_L}\dot{V}_i + \Delta\omega V_i + \frac{\omega_0}{2Q_L}V_r &= \frac{R_L}{2Q_L}(\dot{I}_i + \omega_0 I_r) \\ \dot{V}_i - \frac{1}{2Q_L}\dot{V}_r - \Delta\omega V_r + \frac{\omega_0}{2Q_L}V_i &= -\frac{R_L}{2Q_L}(\dot{I}_r + \omega_0 I_i)\end{aligned}$$

Multiplying the second equation by  $\frac{1}{2Q_L}$  and subtracting it from the first one:

$$\dot{V}_r\left(1 + \frac{1}{4Q_L^2}\right) + \Delta\omega V_i - \frac{\Delta\omega}{2Q_L}V_r + \frac{\omega_0}{2Q_L}V_r - \frac{\omega_0}{4Q_L^2}V_i = \frac{R_L}{2Q_L}\left(\dot{I}_i + \frac{1}{2Q_L}\dot{I}_r + \omega_0 I_r - \omega_0 \frac{1}{2Q_L}I_i\right) ;$$

and adding the second equation to the first one multiplied by  $\frac{1}{2Q_L}$ :

$$\dot{V}_i\left(1 + \frac{1}{4Q_L^2}\right) - \Delta\omega V_r + \frac{\Delta\omega}{2Q_L}V_i + \frac{\omega_0}{2Q_L}V_i + \frac{\omega_0}{4Q_L^2}V_r = \frac{R_L}{2Q_L}\left(-\dot{I}_r + \frac{1}{2Q_L}\dot{I}_i + \omega_0 I_i + \omega_0 \frac{1}{2Q_L}I_r\right) .$$

If we defined  $\alpha$  by

$$\alpha := \frac{1}{1 + \frac{1}{4Q_L^2}} = \frac{4Q_L^2}{1 + 4Q_L^2}$$

the two previous equations will be written as:

$$\begin{aligned}\dot{V}_r + \alpha\left(\Delta\omega V_i - \frac{\Delta\omega}{2Q_L}V_r + \omega_{1/2}V_r - \frac{\omega_{1/2}}{2Q_L}V_i\right) &= \alpha R_L \omega_{1/2}\left(\frac{1}{\omega_0}\dot{I}_i + \frac{1}{\omega_0 2Q_L}\dot{I}_r + I_r - \frac{1}{2Q_L}I_i\right) \\ \dot{V}_i + \alpha\left(-\Delta\omega V_r + \frac{\Delta\omega}{2Q_L}V_i + \omega_{1/2}V_i + \frac{\omega_{1/2}}{2Q_L}V_r\right) &= \alpha R_L \omega_{1/2}\left(-\frac{1}{\omega_0}\dot{I}_r + \frac{1}{\omega_0 2Q_L}\dot{I}_i + I_i + \frac{1}{2Q_L}I_r\right)\end{aligned}$$

with  $\omega_{1/2} = \frac{\omega_0}{2Q_L}$ .

These equations are represented in the state space formalism by:

$$\begin{aligned}\frac{d}{dt}\begin{pmatrix} V_r \\ V_i \end{pmatrix} &= \alpha\begin{pmatrix} -\omega_{1/2} + \frac{\Delta\omega}{2Q_L} & -\Delta\omega + \frac{\omega_{1/2}}{2Q_L} \\ \Delta\omega - \frac{\omega_{1/2}}{2Q_L} & -\omega_{1/2} - \frac{\Delta\omega}{2Q_L} \end{pmatrix} \cdot \begin{pmatrix} V_r \\ V_i \end{pmatrix} \\ &+ \alpha R_L \omega_{1/2}\begin{pmatrix} 1 & -\frac{1}{2Q_L} \\ \frac{1}{2Q_L} & 1 \end{pmatrix} \cdot \begin{pmatrix} I_r \\ I_i \end{pmatrix} \\ &+ \alpha R_L \frac{\omega_{1/2}}{\omega_0}\begin{pmatrix} \frac{1}{2Q_L} & 1 \\ -1 & \frac{1}{2Q_L} \end{pmatrix} \cdot \frac{d}{dt}\begin{pmatrix} I_r \\ I_i \end{pmatrix}\end{aligned}$$

This equation is an inhomogeneous matrix differential equation with inhomogeneity function  $f(t)$

$$f(t) = \alpha R_L \omega_{1/2}\begin{pmatrix} 1 & -\frac{1}{2Q_L} \\ \frac{1}{2Q_L} & 1 \end{pmatrix} \cdot \begin{pmatrix} I_r \\ I_i \end{pmatrix} + \alpha R_L \frac{\omega_{1/2}}{\omega_0}\begin{pmatrix} \frac{1}{2Q_L} & 1 \\ -1 & \frac{1}{2Q_L} \end{pmatrix} \cdot \frac{d}{dt}\begin{pmatrix} I_r \\ I_i \end{pmatrix} .$$

The solution for  $\mathbf{V}(t) = \begin{pmatrix} V_r \\ V_i \end{pmatrix}$  is defined on intervals with continuous function  $f(t)$ . In the case of  $Q_L \gg 1$ ,  $\omega_{1/2} \ll \omega_0$  and  $\Delta\omega \ll \omega_0$ , we obtain the approximation

$$\frac{d}{dt} \begin{pmatrix} V_r \\ V_i \end{pmatrix} = \begin{pmatrix} -\omega_{1/2} & -\Delta\omega \\ \Delta\omega & -\omega_{1/2} \end{pmatrix} \cdot \begin{pmatrix} V_r \\ V_i \end{pmatrix} + \begin{pmatrix} R_L\omega_{1/2} & 0 \\ 0 & R_L\omega_{1/2} \end{pmatrix} \cdot \begin{pmatrix} I_r \\ I_i \end{pmatrix}.$$

## A.7 Open Loop Transfer Function of the Digital RF Feedback System

After simplification of the system, the transfer matrix of the continuous system is given by:

$$H_{cont}(s) \approx H_{cav}(s) = H_\pi(s) + H_{\frac{8}{9}\pi}(s)$$

in which the transfer matrices for the two modes are:

$$\begin{aligned} \pi\text{-mode} \quad H_\pi(s) &= \frac{(\omega_{1/2})_\pi}{\Delta\omega_\pi^2 + (s + (\omega_{1/2})_\pi)^2} \begin{pmatrix} s + (\omega_{1/2})_\pi & -\Delta\omega_\pi \\ \Delta\omega_\pi & s + (\omega_{1/2})_\pi \end{pmatrix} \\ \frac{8}{9}\pi\text{-mode} \quad H_{\frac{8}{9}\pi}(s) &= -\frac{(\omega_{1/2})_{\frac{8}{9}\pi}}{\Delta\omega_{\frac{8}{9}\pi}^2 + (s + (\omega_{1/2})_{\frac{8}{9}\pi})^2} \begin{pmatrix} s + (\omega_{1/2})_{\frac{8}{9}\pi} & -\Delta\omega_{\frac{8}{9}\pi} \\ \Delta\omega_{\frac{8}{9}\pi} & s + (\omega_{1/2})_{\frac{8}{9}\pi} \end{pmatrix}. \end{aligned}$$

The discretization of the system is represented by the transfer matrices in the  $z$ -space  $H_\pi(z)$  and  $H_{\frac{8}{9}\pi}(z)$ :

$$\begin{aligned} H_\pi(z) &= \left(1 - \frac{1}{z}\right) \mathcal{Z} \left\{ \frac{H_\pi(s)}{s} \right\} = \frac{z-1}{z} \cdot \mathcal{Z} \left\{ \mathcal{L}^{-1} \left\{ \frac{H_\pi(s)}{s} \right\} \Big|_{t=kT_s} \right\} \\ H_{\frac{8}{9}\pi}(z) &= -\left(1 - \frac{1}{z}\right) \mathcal{Z} \left\{ \frac{H_{\frac{8}{9}\pi}(s)}{s} \right\} = \frac{z-1}{z} \cdot \mathcal{Z} \left\{ \mathcal{L}^{-1} \left\{ \frac{H_{\frac{8}{9}\pi}(s)}{s} \right\} \Big|_{t=kT_s} \right\}. \end{aligned}$$

The result of the transformation gives:

$$\begin{aligned} H_\pi(z) &= \frac{(\omega_{1/2})_\pi}{\Delta\omega_\pi^2 + (\omega_{1/2})_\pi^2} \begin{pmatrix} (\omega_{1/2})_\pi & -\Delta\omega_\pi \\ \Delta\omega_\pi & (\omega_{1/2})_\pi \end{pmatrix} \\ &\quad - \frac{(\omega_{1/2})_\pi}{\Delta\omega_\pi^2 + (\omega_{1/2})_\pi^2} \cdot \frac{z-1}{z^2 - 2ze^{(\omega_{1/2})_\pi T_s} \cdot \cos(\Delta\omega_\pi T_s) + e^{2(\omega_{1/2})_\pi T_s}} \\ &\quad \cdot \left\{ \left( z - e^{(\omega_{1/2})_\pi T_s} \cdot \cos(\Delta\omega_\pi T_s) \right) \cdot \begin{pmatrix} (\omega_{1/2})_\pi & -\Delta\omega_\pi \\ \Delta\omega_\pi & (\omega_{1/2})_\pi \end{pmatrix} \right. \\ &\quad \left. - e^{(\omega_{1/2})_\pi T_s} \cdot \sin(\Delta\omega_\pi T_s) \cdot \begin{pmatrix} \Delta\omega_\pi & (\omega_{1/2})_\pi \\ -(\omega_{1/2})_\pi & \Delta\omega_\pi \end{pmatrix} \right\} \end{aligned}$$

$$\begin{aligned}
H_{\frac{8}{9}\pi}(z) &= -\frac{(\omega_{1/2})_{\frac{8}{9}\pi}}{\Delta\omega_{\frac{8}{9}\pi}^2 + (\omega_{1/2})_{\frac{8}{9}\pi}^2} \begin{pmatrix} (\omega_{1/2})_{\frac{8}{9}\pi} & -\Delta\omega_{\frac{8}{9}\pi} \\ \Delta\omega_{\frac{8}{9}\pi} & (\omega_{1/2})_{\frac{8}{9}\pi} \end{pmatrix} \\
&+ \frac{(\omega_{1/2})_{\frac{8}{9}\pi}}{\Delta\omega_{\frac{8}{9}\pi}^2 + (\omega_{1/2})_{\frac{8}{9}\pi}^2} \cdot \frac{z-1}{z^2 - 2ze^{(\omega_{1/2})_{\frac{8}{9}\pi}T_s} \cdot \cos(\Delta\omega_{\frac{8}{9}\pi}T_s) + e^{2(\omega_{1/2})_{\frac{8}{9}\pi}T_s}} \\
&\cdot \left\{ \left( z - e^{(\omega_{1/2})_{\frac{8}{9}\pi}T_s} \cdot \cos(\Delta\omega_{\frac{8}{9}\pi}T_s) \right) \cdot \begin{pmatrix} (\omega_{1/2})_{\frac{8}{9}\pi} & -\Delta\omega_{\frac{8}{9}\pi} \\ \Delta\omega_{\frac{8}{9}\pi} & (\omega_{1/2})_{\frac{8}{9}\pi} \end{pmatrix} \right. \\
&\quad \left. - e^{(\omega_{1/2})_{\frac{8}{9}\pi}T_s} \cdot \sin(\Delta\omega_{\frac{8}{9}\pi}T_s) \cdot \begin{pmatrix} \Delta\omega_{\frac{8}{9}\pi} & (\omega_{1/2})_{\frac{8}{9}\pi} \\ -(\omega_{1/2})_{\frac{8}{9}\pi} & \Delta\omega_{\frac{8}{9}\pi} \end{pmatrix} \right\}
\end{aligned}$$

and  $H_{dis}(z) = H_{\pi}(z) + H_{\frac{8}{9}\pi}(z)$ .

## A.8 Solution of the First-Order Differential Equation

The solution of the first-order differential equation

$$\Delta\dot{\omega}(t) = -\frac{1}{\tau_m} (\Delta\omega(t) - \Delta\omega_T) - \frac{2\pi}{\tau_m} K \cdot E_{acc}^2(t)$$

is calculated for the time-dependent accelerating field shown in Figure 6.6. For the three different time ranges, the accelerating field is given by:

$$E_{acc}(t) = \begin{cases} E_1(1 - e^{-t/\tau_{ctrl}}) & : 0 \leq t \leq t_{inj} \\ E_0 & : t_{inj} \leq t \leq t_{off} \\ E_0 \cdot e^{-(t-t_{off})/\tau_{cav}} & : t_{off} \leq t \end{cases}$$

where  $E_0 = E_1(1 - e^{-t_{inj}/\tau_{ctrl}})$ .

The corresponding solutions are

1)  $0 \leq t \leq t_{inj}$  :

$$\begin{aligned}
\Delta\omega_{\oplus}(t) &= \Delta\omega_T - 2\pi K E_1^2 \left\{ 1 - 2\frac{\tau_{ctrl}}{\tau_{ctrl} - \tau_m} e^{-t/\tau_{ctrl}} + \frac{\tau_{ctrl}}{\tau_{ctrl} - 2\tau_m} e^{-2t/\tau_{ctrl}} \right\} \\
&+ 2\pi K E_1^2 \cdot e^{-t/\tau_m} \cdot \left\{ 1 - 2\frac{\tau_{ctrl}}{\tau_{ctrl} - \tau_m} + \frac{\tau_{ctrl}}{\tau_{ctrl} - 2\tau_m} \right\}
\end{aligned}$$

where  $\tau_{ctrl}$  has to be different from  $\tau_m$  and  $2\tau_m$

2)  $t_{inj} \leq t \leq t_{off}$  :

$$\begin{aligned}
\Delta\omega_{\oplus}(t) &= \Delta\omega_T + \left( \Delta\omega_{\oplus}(t_{inj}) - \Delta\omega_T \right) \cdot e^{-(t-t_{inj})/\tau_m} \\
&- 2\pi K E_0^2 + 2\pi K E_0^2 \cdot e^{-(t-t_{inj})/\tau_m}
\end{aligned}$$

3)  $t_{off} \leq t$ :

$$\begin{aligned} \Delta\omega_{\textcircled{3}}(t) = & \Delta\omega_T + \left( \Delta\omega_{\textcircled{2}}(t_{off}) - \Delta\omega_T \right) \cdot e^{-(t-t_{off})/\tau_m} \\ & - 2\pi K E_0^2 + 2\pi K E_0^2 \frac{\tau_{cav}}{\tau_{cav} - 2\tau_m} \cdot \left\{ e^{-2(t-t_{off})/\tau_{cav}} - e^{-(t-t_{off})/\tau_m} \right\} \end{aligned}$$

where  $\tau_{cav}$  has to be different from  $2\tau_m$

# Bibliography

- [CDR 500] 'Conceptual Design Report for a 500 GeV Linear Collider (TESLA)', DESY Print, (1997)
- [TTF CDR] 'Conceptual Design Report for the TESLA Test Facility', D. Edwards, DESY Print, (1995)
- [TESLA Prop.] TESLA-COLLABORATION, 'A Proposal to Construct and Test Prototype Superconducting RF Structures for Linear Colliders', DESY Print TESLA 93-01, DESY Print, (March 1993)
- [Grä 92] H.-D. Gräf, 'Experience with Control of Frequency, Amplitude and Phase', Proceedings of the 5th Workshop on RF Superconductivity', DESY Print M-92-01, (1992), 317
- [Sim 93] S.N. Simrock, 'Experience with Control of Frequency, Amplitude and Phase', Proceedings of the 6th Workshop on RF Superconductivity', Newport News, VA (1992), 294
- [Mos 95] A. Mosnier, O. Napoly, 'Energy Spread Sources in TESLA and TTF', DESY Print TESLA 95-05, (1995)
- [Mos 94] A. Mosnier, J.M. Tessier, 'Field Stabilization Study for TESLA', DESY Print TESLA 94-16, (1994)
- [Ju et.al.93] V. Juravlev, A. Sery, A. Sleptsov, W. Coosemans, G. Ramseier, I. Wilson, CERN SL/93-53, CLIC-Note 217, (1993)
- [Shi et.al.95] V. Shiltsev, B. Baklakov, P. Lebedev, J. Rossbach, C. Montag, 'Measurement of Ground Vibrations and Orbit Motion at HERA', DESY HERA 95-06, (June 1995)
- [Br/Ro 94] R. Brinkmann, J. Rossbach, 'Observation of Orbit Motion in HERA Covering Eight Decades in Frequency', Nucl. Instr. Meth. **A350**, 8, (1994)
- [Ga] A. Gamp, privat communication, (1998)
- [Mon 48] C.G. Montgomery, R.H. Dicke and E.M.Purcell, 'Principles of Microwave Circuits', Radiation Laboratory Series Vol. 8, McGraw-Hill, New York, (1948), Ch. 7

- [Wil 82] P.B. Wilson, 'High Energy Electron Linacs: Applications to Storage Ring RF Systems and Linear Colliders', SLAC-PUB-2884, (1987)
- [Kre] G. Kreps, private communication, (1998)
- [Beck] R. Becker, F. Sauter, 'Theorie der Elektrizität', Teubner, (1968), p.157
- [Sla] J.R. Slater, 'Microwave Electronics', van Nostrand, (1950), p.80
- [Mos 93] A. Mosnier, 'Dynamic Measurements of the Lorentz Forces on a MACSE cavity', DESY Print TESLA 93-09, (1993)
- [Hün 98] M. Hüning, 'Selbstoptimierende Parametersteuerung der Hochfrequenz des supraleitenden Linearbeschleunigers TESLA Test Facility', DESY Print TESLA, to be published
- [Lie 98] M. Liepe, 'Adaptive Feed Forward for the Digital RF Control System of the TESLA Test Facility', DESY Print TESLA, to be published
- [Lud 96] Ludyk, 'Theoretische Regelungstechnik', vol. 1,2 , (1996)
- [Lu/We] H. Lutz, W. Wendt, 'Taschenbuch der Regelungstechnik', Verlag Harri Deutsch, (1995)
- [Lun 97] J. Lunze, 'Regelungstechnik 2', Springer Verlag Berlin Heidelberg, (1997)
- [Lev 95] W.S. Levine (editor), 'The Control Handbook', CRC Press in Cooperation with IEEE Press, (1995)
- [Doo/Sim] L. Doolittle, S.N. Simrock, private communication, (1997)
- [Mar 93] A. Marziali, H.A. Schwettman, 'Vibrational Analysis of the TESLA Structure', DESY Print TESLA 93-41, (1993)



## Acknowledgements

I would first like to thank my Doktorvater, Prof. Dr. P. Schmüser, for all the advice and encouragement that he has given me along the way. He has helped me to make my years at DESY interesting and productive, and I appreciate his many efforts undertaken on my behalf.

I owe sincere thanks to S. Simrock for all the support and stimulus with which he has provided me during the past three years. He has never hesitated to share with me his rich scientific and human experience.

I also offer my thanks to Dr. A. Gamp for his interest and contributions to this work.

In recognition of all they have contributed to the success of this project, I would like to express gratitude to the members of the low level RF control group, S. Goloborodko, M. Hning, M. Liepe, A. Kholodny, J. Sonnenberg, and Y. Tchernouosko.

Thanks are due in particular to Dr. H. Weise for his continuous encouragement and moral support throughout the length of my stay in Hamburg.

I would like to thank all my colleagues from the FDET and MHF groups for providing a stimulating and friendly work environment.

K. Rehlich and O. Hensler deserve honourable mention for their continuous computer support.

I offer my thanks to Dr. P. Castro-Garcia, M.P. Zorzano-Mier and I. Reyzl for their contribution to the layout of this work and their encouragement in recent weeks.

I would like to express my gratitude to all members of my family, who have always believed in me and encouraged me to do my best.

Finally, C. Adloff deserves my heartfelt thanks for all the fantastic support she has given me during this difficult time.



**Eidesstattliche Erklärung:**

Hiermit erkläre ich an Eides statt, daß ich die vorliegende Dissertation selbständig verfaßt, keine anderen als die angegebenen Hilfsmittel verwendet und bisher noch keinen Promotionsversuch unternommen habe.

Hamburg, im März 1998